La borsa di dottorato è stata cofinanziata con risorse del
Programma Operativo Nazionale Ricerca e Innovazione 2014-202 (CCI 2014IT16M2OP005)
Fondo Sociale Europeo, Azione I.1 "Dottorati Innovativi con caratterizzazione Industriale"

UNIVERSITA' DELLA CALABRIA
Dipartimento di Fisica

Dottorato di Ricerca in
Scienze e Tecnologie Fisiche Chimiche e dei Materiali

CICLO
XXXV

Optical Metasurfaces: from reconfigurable polymer-based platforms to sensing applications.

Settore Scientifico Disciplinare FIS/03

Coordinatore: Ch.mo Prof. Gabriella Cipparrone
Firma [redacted] Firma oscurata in base alle linee guida del Garante della privacy

Supervisore/Tutor: Ch.mo Prof. Giuseppe Strangi
Firma____ Firma oscurata in base alle linee guida del Garante della privacy

Dottorando: Dott. Giuseppe Nicoletta

Firma oscurata in base alle linee guida del Garante della privacy

Abbreviations

MDM	Metal-Dielectric-Metal
FROC	Fano Resonance Optical Coating
SPP	Surface Plasmon Polaritons
LSPR	Localized Surface Plasmon Resonances
SERS	Surface Enhanced Raman Spectroscopy
LCP	Left Circular Polarized
RCP	Right Circular Polarized
CD	Circular Dichroism
UV	Ultraviolet
IR	Infrared
FOM	Figure of Merit
EWFD	Electromagnetic Waves, Frequency Domain
PDEs	Partial Differential Equations
FEM	Finite Element Method
PBCs	Periodic Boundary COnditions
PMLs	Perfect Matched Layers
TE	Transverse Electric
TM	Transverse Magnetic
FWHM	Full Width at Half Maximum
RIU	Refractive Index Unit
POM	Polarized Optical Microscopy
AuNP/GNP	Gold Nanoparticle
CMOS	Complementary Metal Oxide Semiconductor
SEM, TEM	Scanning and Transmission Electron Microscopy

List of Symbols and Constants

c_0	Speed of light
ϵ_0	Dielectric vacuum constant
ω	Angular frequency
λ	Wavelength
ϵ_r	Relative dielectric constant
μ_r	Relative permability
R	Reflectance
T	Trasmittance
A	Absorbance
$\|\|$	Parallel direction
$\perp$	Perpendicular direction
ν	Frequency
k	Wave vector
n	Refractive index
$\mathbf{E}$	Electric field
$\mathbf{E}_0$	External Electric field amplitude
γ	Damping constant
$\mathbf{D}$	Electric displacement
$\mathbf{J}$	Electric current density
h	Planck constant
I	Light or laser intensity

List of Pubblications

- Palermo, G., Sreekanth, K. V., Maccaferri, N., Lio, G. E., **Nicoletta, G.**, De Angelis, F., ... Strangi, G. (2020). Hyperbolic dispersion metasurfaces for molecular biosensing. Nanophotonics, 10(1), 295-314.
- Lininger, A., Palermo, G., Guglielmelli, A., **Nicoletta, G.,** Goel, M., Hinczewski, M., Strangi, G. (2022). Chirality in light–matter interaction. Adv. Mater, 2107325.
- Palermo, G., Lininger, A., Guglielmelli, A., Ricciardi, L., **Nicoletta, G.**, De Luca, A., ... Strangi, G. (2022). All-Optical tunability of metalenses permeated with liquid crystals. ACS nano, 16(10), 16539-16548.
- Guglielmelli, A., **Nicoletta, G.**, Valente, L., Palermo, G., Strangi, G. (2022). Numerical Modeling of 3D Chiral Metasurfaces for Sensing Applications. Crystals, 12(12), 1804.

Abstract

Research is of paramount importance for the well-being and improvement of life, and this is often supported by material research. It is enough to remember that in the past man could greatly improve his own existence by the discovery of stone, and later he could do so by the discovery of bronze and still later iron. Technology today leads us to have increasingly compact devices that are capable of transmitting data as quickly as possible. Among the greatest challenges for scientists is research into materials for microprocessors, optical fibers, and the optimal use of renewable energy sources. The study of light-matter interaction is of fundamental importance since most electromagnetic devices and phenomena originate from it. In this case, the creation of different structures and geometries makes it possible to modify electromagnetic radiation for the intended scientific purposes. Metamaterials offer the possibility to overcome the limits of the physical and chemical properties of materials. With technical processes, it is possible to create structures that show a unique response thanks to their dimensions, which are smaller than the characteristic incident wavelength. One of the most important challenges in the biomedical, environmental, and chemical fields is the biorecognition of analytes in the surrounding environment with high sensitivity and specificity. One possible solution to achieve this goal is to study the change in refractive index that correlates with the specific molecule or biomolecule that needs to be detected in a fluid. The aim of this thesis is to develop an optical approach for various metasurfaces with high sensitivity, which can be used for biosensors and thus for the detection of biological material such as cells, proteins, bacteria etc. Another important aspect is the study of metasurfaces capable of opti-

cal reconfiguration by external stimuli, useful to tune the focus of metalenses. This thesis is divided into four chapters, one appendix, and conclusion and perspective.

In the first chapter, the concept of chirality is introduced, the interaction between chiral light and chiral matter. The focus is on extrinsic chiral metasurfaces, the study of 3D out-of-plane helices. A modeling study of various helix parameters and an analysis of the modes and their sensitivity have been performed.

The second chapter presents Fano Resonance Optical Coating (FROC). After a brief introduction, relevant theoretical references are given. After accurate simulations on the FROCs, several samples were fabricated and analyzed by spectrophotometry and ellipsometry to provide a few applications for these samples.

In the third chapter, metalenses supplied by the Capasso group are presented, infiltrated with various liquid crystals according to Cassie-Baxter theory. The purpose is to tune the metasurface to allow in-depth optical investigation. The goal is to tune the metalenses using photonics to excite the gold nanoparticles inside the liquid crystal.

In the fourth chapter, a technique is presented for the low-cost reproduction of metalenses, which focus visible light and can be thermally tuned. The goal is to provide materials that do not degrade over time and that retain their properties for focusing. It has been experimentally demonstrated that due to the thermal effect, it is possible to tune the focus of the lens with a shift of 150 μm.

In the appendix, we present a metasurface consisting of a polymer matrix containing gold nanoparticles. These substrates are analyzed from a thermoplasmonic point of view, obtaining excellent results useful, for example, for the purification of materials from bacteria. In addition, these membranes are analyzed from the point of view of sensing by stretching. In the second appendix metasurfaces based on the MIMI nanocavities used as a platform for refractive index sensing are presented.

Finally, the achieved results are discussed and future perspectives based on the work of this thesis are shown.

Introduzione

La ricerca è di fondamentale importanza per il benessere e il miglioramento della vita dell'uomo, e questo è spesso supportato dalla ricerca dei materiali. Basti ricordare che in passato l'uomo poté migliorare notevolmente la propria esistenza con la scoperta della pietra, e più tardi lo poté fare con la scoperta del bronzo e più tardi ancora del ferro. La tecnologia oggi ci porta ad avere dispositivi sempre più compatti in grado di trasmettere i dati il più velocemente possibile. Tra le maggiori sfide per gli scienziati c'è la ricerca sui materiali per i microprocessori, le fibre ottiche e l'uso ottimale delle fonti energetiche rinnovabili. Lo studio dell'interazione luce-materia è di fondamentale importanza poiché la maggior parte dei dispositivi e dei fenomeni elettromagnetici hanno origine da esso. In questo caso, la realizzazione di strutture e geometrie differenti permette di modificare la radiazione elettromagnetica per gli scopi scientifici previsti. I metamateriali offrono la possibilità di superare i limiti delle proprietà fisiche e chimiche dei materiali. Con processi tecnici è possibile creare strutture che mostrano una risposta unica grazie alle loro dimensioni, che sono inferiori alla lunghezza d'onda incidente caratteristica. Una delle sfide più importanti in campo biomedico, ambientale e chimico è il bioriconoscimento di analiti nell'ambiente circostante con elevata sensibilità e specificità. Una possibile soluzione per raggiungere questo obiettivo è studiare il cambiamento nell'indice di rifrazione correlato alla specifica molecola o biomolecola che deve essere rilevata in un fluido. Lo scopo di questa tesi è sviluppare un approccio ottico per varie metasuperfici ad alta sensibilità, che possa essere utilizzato per biosensori e quindi per il rilevamento di materiale biologico come cellule, proteine, batteri ecc. Un altro aspetto importante è lo studio di metasuperfici capaci di una riconfigurazione ottica dovuta a stimoli esterni, utili ad esempio per tunare il focus di metalenti. Questa tesi è suddivisa in quattro capitoli, un'appendice, conclusioni e prospettive.

Nel primo capitolo viene introdotto il concetto di chiralità, l'interazione tra luce chirale e materia chirale. L'attenzione si concentra sulle metasuperfici chirali estrinseche, e in paricolare sullo studio delle eliche 3D fuori dal piano. È stato eseguito uno studio di modellazione di vari parametri dell'elica e un'analisi dei modi e della loro sensibilità.

Nel secondo capitolo vengono presentati i Fano Resonance Optical Coatings (FROCs). Dopo una breve introduzione, vengono forniti i cenni teorici sulla risonanza di Fano. Dopo accurate simulazioni sui FROCs, diversi campioni sono stati fabbricati e analizzati mediante spettrofotometria ed ellissometria per fornire alcune applicazioni per questi campioni.

Nel terzo capitolo vengono presentate delle metalenti fornite dal gruppo Capasso dell'università di Harvard, infiltrate con differenti cristalli liquidi secondo la teoria prevista. Lo scopo è quello di analizzare le metasuperfici per consentire un'indagine ottica approfondita nel campo di nuovi device. L'obiettivo è tunare le metalenti usando la luce visibile per eccitare le nanoparticelle d'oro all'interno della mistura con il cristallo liquido.

Nel quarto capitolo viene presentata una tecnica per la fabbricazione a basso costo di metalenti, che focalizzano la luce visibile e possono essere tunate termicamente. L'obiettivo è quello di fornire materiali e in particolare lenti che non si degradino nel tempo e che mantengano le loro proprietà di focalizzazione. Una proprietà importante rilevata è che queste lenti polimeriche sono flessibili e quindi adattabili ad ogni tipo di device. È stato dimostrato sperimentalmente che per effetto termico è possibile shiftare il fuoco della lente con uno spostamento di 150 μm.

In appendice è presentata una metasuperficie costituita da una matrice polimerica contenente nanoparticelle d'oro. Questi substrati vengono analizzati dal punto di vista termoplasmonico, ottenendo ottimi risultati utili, ad esempio, per la purificazione dei materiali dai batteri. Inoltre, queste membrane vengono analizzate mediante stretching e compressione per fornire anche in questo caso informazioni relative allo shift in lunghezza d'onda. Nella seconda appendice vengono presentate delle metasupefici basate sulle nanocavità MIMI usate come piattaforma per il sensing di indice di rifrazione. Infine, vengono discussi i risultati raggiunti e vengono mostrate le prospettive future basate sul lavoro di questa tesi.

Contents

Chapter 1

Chirality in light-matter interaction: numerical analysis of 3D helical metasurfaces

Sensitivity and specificity are critical factors in biosensing platforms, playing a vital role in facilitating the successful transfer of technology. Efforts have been extensively devoted to developing sensing platforms that can effectively control the interaction between light and matter at the nanoscale. Achieving high sensitivity is crucial for biosensing platforms as it determines their ability to detect and quantify target analytes accurately. By enhancing the sensitivity of a biosensor, even low concentrations of analytes can be detected, enabling early disease diagnosis, environmental monitoring, and other important applications. Researchers have explored various strategies to enhance sensitivity, such as employing nanomaterials with unique optical properties, developing novel transduction mechanisms, and optimizing the design of the sensing interfaces. On the other hand, specificity refers to the ability of a biosensing platform to selectively recognize and differentiate between the target analyte and other interfering substances present in complex biological samples. Specificity is crucial for minimizing false-positive or false-negative results, ensuring the reliability of the biosensor. To achieve high specificity, researchers have focused on designing recognition elements that exhibit high affinity and selectivity towards the target analyte. This often involves the use of biomolecules such as antibodies, aptamers, or enzymes that can selectively bind to the target analyte with high affinity, while minimizing cross-reactivity with non-target molecules. In recent years, nanotechnology has played a pivotal role in advancing biosensing platforms. By harnessing the unique properties of nanomaterials, such as plasmonic nanoparticles, quantum dots, or carbon nanotubes, researchers have been able to manipulate light-matter interactions at the nanoscale. These nanomaterials can be tailored to exhibit specific optical properties, such as enhanced light scattering or absorption, which can be harnessed for sensitive and selective detection of analytes. Additionally, the large surface-to-volume ratio of nanomaterials provides ample opportunities for functionalization with recognition elements, further enhancing the specificity of biosensing platforms. Furthermore, the integration of nanoscale components into biosensing platforms allows for miniaturization, portability, and multiplexing capabilities. These advancements have paved the way for the development of point-of-care diagnostic devices, wearable sensors, and lab-on-a-chip systems, enabling rapid and on-site analysis in various fields, including healthcare, food safety, and environmental monitoring. In this chapter it is investigated how a 3D out-of-plane chiral plasmonic metasurface can be used as a key element in a sensing platform, by exploiting the variation of the plasmonic and lattice modes as a function of the refractive index of the surrounding medium. The results indicate that chiral metasurfaces can be used to perform sensing, by detecting the refractive index change with a maximum sensitivity of 761 nm/RIU. The metasurface properties can be suitably designed to maximize the optical response in terms of shift modulated by the refractive index of the analyte molecules. Such studies can pave the way for engineering and fabricating highly selective and specific chiral metasurface-based refractive index sensing platforms.

1.1 Introduction

In the biomedical, environmental, and chemical fields, the biorecognition of analytes with high sensitivity and specificity is a significant challenge. However, one potential solution to address this challenge is by utilizing refractive index sensors to probe changes in the refractive index associated with specific molecules or biomolecules in the surrounding fluid environment. This approach can be particularly valuable in screening and detecting cancer progression by monitoring alterations in the refractive index of cells and tissues. Cancer progression is often accompanied by various molecular and cellular changes within the affected tissues. These changes can manifest as alterations in the refractive index, which is a result of differences in the composition, concentration, and structural properties of the cells and tissues. By employing refractive index sensors, researchers can detect and quantify these changes, providing valuable insights into the progression and characteristics of cancer. Refractive index sensors function by measuring the refractive index of the medium surrounding the sensor surface. These sensors typically consist of a transducer that interacts with the sample, allowing the detection of changes in the refractive index through the modulation of light-matter interactions. When specific molecules or biomolecules bind to the sensor surface, they induce changes in the refractive index, leading to measurable signals that can be correlated with the presence or concentration of the analyte of interest. In the context of cancer research, refractive index sensors can be used to detect biomarkers associated with cancer cells or tissues. These sensors can be functionalized with specific recognition elements, such as antibodies or aptamers, that selectively bind to the target biomarkers. Upon binding, the refractive index at the sensor surface changes, providing a means to detect and quantify the presence of cancer-related analytes. The advantages of refractive index sensors in cancer detection lie in their label-free and real-time detection capabilities. They offer the potential for non-invasive and rapid analysis, allowing for continuous monitoring of cancer progression or response to treatment. Additionally, by utilizing arrays of sensors with different recognition elements, multiplexed detection of multiple biomarkers becomes possible, enabling a more comprehensive characterization of cancer-related changes. However, it's important to note that the development and application of refractive index sensors for cancer detection is an active area of research, and further studies are needed to optimize their sensitivity, specificity, and practical implementation. Nonetheless, the potential for using refractive index sensors to screen and detect cancer progression based on changes in the refractive index of cells and tissues holds promise for advancing cancer diagnostics and personalized medicine approaches. [1–3]. It is possible to retrieve the refractive index in the analyte by converting it into a detectable optical signal. In this direction, the most widely studied are the plasmonic refractive index sensor based on metal nanostructures [4, 5]. Optical sensors overcome many limitations of conventional analytical techniques by offering some advantages: (1) high sensitivity/selectivity, (2) real-time analyses, (3) label-free detection of bio-chemical molecules, and (4) small sizes [6]. Surface Plasmon Polaritons (SPP) and Localized Surface Plasmon Resonance (LSPR) sensing are well-established methods based on the shift of the LSPR frequency caused by the change in the refractive index of the nanostructure surrounding medium [7, 8]. Through the integration of metasurface, a whole new paradigm shift in sensor technology has been opened up, reaching boosted sensitivity, enhanced detection accuracy, and size even more compacted, easily implementable with lab-on-chip devices [9, 10]. Metasurfaces are two-dimensional materials with tailoring subwavelength structures and intriguing optical properties. Each elementary unit of the metasurface is characterized by electromagnetic resonances very sensitive to changes in the surrounding medium (the analyte polarizability), and so perfect to be implemented in optical sensors. The resonant electromagnetic spectrum, dominated by the environment, can be suitably tuned by engineering the individual meta-atoms geometry or their periodic arrangements. Different geometry and structure arrangement have been tested to optimize the performance of LSPR sensors, including gold nanocheckerboard arrays [11], gold mushroom arrays [12], gold–silver alloy nanodisk arrays [13], nanopin-cavity resonators [14], gold–silver alloy nanodisk [13] and split-ring resonators [15]. The shifts occurring in the resonant modes of the output spectrum allow the probing of the refractive index of the surrounding molecular analytes. Metasurface-based refractive index sensing platforms present several advantages over conventional SPP-based sensors in terms of fabrication tolerance, reliable readout signal [16], lower radiative damping and higher quality factor. Moreover, some interesting optical phenomena can occur like plasmonically induced transparency [17], Fano resonances [18], multiple resonances, and broadband slow light effects resulting from a complex arrangement of meta-atoms in a unit- or super-cell [19]. In addition, the detection of small molecules concentration is allowed due to the confinement of optical energy into volumes substantially smaller than diffraction-limited optical spots [20]. Furthermore, sensitive detection of small volumes can be realized thanks to Surface-Enhanced Raman Spectroscopy (SERS) mediated by an inverted pyramidal metasurface [21]. A further step forward in the field of optical sensing has been marked by the advent of chiral metasurfaces, composed of meta-atoms that do not exhibit mirror symmetry. Researchers have dedicated significant attention to the study of chiral metasurfaces due to their unique chiroptical properties when interacting with Left-Circular Polarized (LCP) or Right-Circular Polarized (RCP) light. Chiral metasurfaces, consisting of subwavelength nanostructures, exhibit handedness or chirality, allowing them to selectively interact with circularly polarized light. The interaction between chiral metasurfaces and circularly polarized light leads to intriguing phenomena known as chiroptical effects. These effects manifest as differences in the transmission, reflection, absorption, or scattering of LCP and RCP light by the chiral metasurface. Chiroptical properties are sensitive to the geometry, arrangement, and material composition of the metasurface structures, providing researchers with opportunities to engineer desired optical responses. Chiral metasurfaces can exhibit various chiroptical phenomena, such as circular dichroism (CD) and optical rotation. Circular dichroism refers to the differential absorption of LCP and RCP light, resulting in different intensities or spectral shifts in the transmitted or reflected light. This property enables the discrimination of molecular structures, as certain molecules exhibit unique CD spectra. Optical rotation, on the other hand, refers to the rotation of the polarization plane of linearly polarized light upon interaction with the chiral metasurface. The magnitude and direction of the optical rotation provide information about the chiral properties of the metasurface. Different chiral structures have been investigated, such as L-shape [22], twisted Z-shaped [23], dagger-like [24], Shuriken structure [25], gammadion structure [26], diatomic metamolecules shape [27], twisted propeller blades shape [28] and 3D helicoidal structure coupled with a hyperbolic metamaterial [29]. Among the various chiral-dependent phenomena, they display the Circular Dichroism (CD) signal which is the different absorption (or transmission) between the two opposite circularly polarized states of light. This mechanism is part of what is called optical activity, the property of chiral systems of responding to LCP or RCP differently [30]. The circularly polarized light shows a peculiar behavior when interacting with chiral meta-elements with a helix-like nanostructure. The light traveling along the helix axis with the same handedness as the helices is reflected, whereas the opposite is transmitted, for frequencies that exceed one octave [31, 32]. Thanks to fine control of the local fields the metasurfaces open the possibilities to perform chiral sensing, as theoretically and experimentally demonstrated [26, 33]. The interaction of an optically active system with light can be controlled locally, and this has generated enormous interest in achieving metamaterial designs with enhanced chiroptical signals [34]. The design of these sensing platforms is also aimed to improve the chiroptical signals of different biomolecules with Ultraviolet (UV), visible, and Infrared (IR) CD bands [35–37].

In this chapter, a metasurface consisting of 3-D chiral gold helices periodically arranged in a 2-D square lattice is designed. The work consists of the investigation of the influence of the structure parameters (number of helix pitch - N, dimension on the unit cell - a, angle of incidence - θ) on the resonant peaks. Furthermore, to test the metasurface performance in terms of refractive index sensor, simulations by changing the surrounding medium refractive index were performed. The estimated sensing sensitivity and the Figure Of Merit (FOM) values are in the range of 450 - 761 nm/RIU and 9.9 - 12.3 RIU^{-1} respectively. We analyzed the CD signal of the structure by changing the polarization state of the incident light, proposing also a molecular detection exploiting the CD signal. The obtained results for the design of such compact chiral plasmonic metasurface can open different possibilities to achieve multi-functionalities such as optical absorption, circular dichroism, and highly sensitive refractive index sensing.

1.2 Theory of chirality in the light–matter interaction

The light - matter interaction at the macroscopic scale is described by classical electrodynamics based on Maxwell's equations.[38] The achiral material response to an electromagnetic wave is described by the constitutive equations:

$$\begin{aligned} \mathbf{D} &= \varepsilon_0 \,\overline{\overline{\varepsilon}}\, \mathbf{E}, \\ \mathbf{B} &= \mu_0 \,\overline{\overline{\mu}}\, \mathbf{H}, \end{aligned} \tag{1.1}$$

where $\mathbf{D}$ the electric displacement field, $\mathbf{E}$ is the electric field, $\mathbf{H}$ is the magnetic field, and $\mathbf{B}$ is the inductive magnetic field, ε_0 and μ_0 are the vacuum permittivity and permeability, respectively, $\overline{\overline{\varepsilon}}$ and $\overline{\overline{\mu}}$ are the relative permittivity and permeability of the material, respectively. For isotropic materials, which have the same electromagnetic properties in every orientation, these two quantities reduce to scalars, resulting in the $\mathbf{E}$ and $\mathbf{D}$ fields (and the $\mathbf{B}$ and $\mathbf{H}$ fields) becoming parallel to one another. However, for anisotropic materials, or materials with different electromagnetic properties at different orientations, $\overline{\overline{\varepsilon}}$ and $\overline{\overline{\mu}}$ take the form of second rank tensors. This means that the fields are no longer necessarily parallel. Anisotropic materials include some crystals and optical metamaterials, materials with engineered structural features much smaller than the wavelength of light.

By combining Maxwell's equations with the constitutive equations above, the wave equation can be obtained.[38] An important solution of this wave equation is represented by monochromatic plane waves, which are described by:

$$\mathbf{E} = E_0\,\mathbf{J}\,e^{i\,(k\,z\,-\,\omega\,t)}, \tag{1.2}$$

where E_0 is the wave amplitude, z is the propagation direction, ω is the angular frequency, k is the wavenumber, and $\mathbf{J}$ is the Jones vector. [39, 40] The Jones vector is used to describe the state of polarization for a propagating light wave. Linearly polarized light (LPL) is described by a Jones vector with all real components:

$$\mathbf{J}^{\phi}_{LPL} = \begin{pmatrix} \cos\,\phi \\ \sin\,\phi \\ 0 \end{pmatrix}, \tag{1.3}$$

where ϕ is the polarization angle, defined as the angle between the electric field vector and the propagation axis. LPL is confined to oscillate within a single plane, defined by the polarization angle and the axis of propagation. The Jones vector for circularly polarized light (CPL) contains an imaginary element and is given as:[41]

$$\mathbf{J}^{\pm}_{CPL} = \frac{1}{\sqrt{2}} \begin{pmatrix} 1 \\ \pm\,i \\ 0 \end{pmatrix}. \tag{1.4}$$

In the case of CPL, a single component of the electric field (the x-component) is either delayed (-) or advanced (+) by a phase factor $\pi/2$ as compared to the y-component, as the wave propagates along the z-axis. Since only a single electric field component is manipulated, the electric field vector will rotate about the optical axis as the wave propagates. This can be contrasted with LPL, where the oscillation plane is fixed. [42] The rotation of propagating CPL has a definite handedness, making CPL waves geometrically chiral objects. The definition of the handedness in a chiral object is always arbitrary since the definition depends on the observer's perspective. We will adopt a common convention in classical optics, known as the detector's view: an observer in the detector plane views an oncoming CPL wave as rotating in the frontal plane. The handedness of the oncoming wave is defined by the direction of rotation for the electric field vector: right circularly polarized (RCP) light rotates clockwise, while left circularly polarized (LCP) light rotates counterclockwise. In this work, we use the notation "+" (RCP) and "-" (LCP) to label the handedness of a CPL wave.

An important class of materials is represented by bi-isotropic media, materials with the special optical property that the polarization state of incident light twists as it passes through the material. The constitutive relations are slightly modified for these materials:[43, 44]

$$\mathbf{D} = \varepsilon\,\mathbf{E} + \xi\,\mathbf{H}, \tag{1.5}$$

$$\mathbf{B} = \mu\,\mathbf{H} + \zeta\,\mathbf{E}, \tag{1.6}$$

where ξ and ζ are the magnetoelectric parameters (dimensionless), representing the coupling strength between the electric and magnetic fields.[45, 46] These quantities are defined as:

$$\xi = (\chi - i\,\kappa)\sqrt{\mu_0\,\varepsilon_0}, \tag{1.7}$$

$$\zeta = (\chi + i\,\kappa)\sqrt{\mu_0\,\varepsilon_0}, \tag{1.8}$$

where χ is the Tellegen parameter and κ is the chirality parameter. The Tellegen parameter is used to describe the magnetoelectric effect, and materials with $\chi \neq 0$ are termed non-reciprocal.[47, 48] The chirality parameter is a quantifiable measurement of the degree of chiral handedness in the material, and changing the sign of κ is equivalent to taking a mirror image of the material. Chiral materials are characterized by $\kappa \neq 0$ and $\chi = 0$, known as a Pasteur medium, or by $\kappa \neq 0$ and $\chi \neq 0$, known as a bi-isotropic medium.[43]

The wave equation in the frequency domain takes on the following form when describing an electric field in a chiral material:[49]

$$\nabla^2 \mathbf{E} + 2\,\omega\mu\xi\,(\nabla \times \mathbf{E}) + \omega^2\mu\varepsilon\,\mathbf{E} = 0, \tag{1.9}$$

where the mode propagation constant satisfies the following equation:

$$k^2 = \left(\frac{\omega^2\mu\varepsilon - k^2}{2\,\omega\mu\xi}\right)^2 . \tag{1.10}$$

This wave equation has two eigen solutions in the form of CPL waves:

$$k_L = -\omega\mu\xi + \omega\,\sqrt{\mu\varepsilon + \mu^2\,\xi^2}, \tag{1.11}$$

$$k_R = \quad \omega\mu\xi + \omega\,\sqrt{\mu\varepsilon + \mu^2\,\xi^2}. \tag{1.12}$$

This result demonstrates the double mode propagation in the medium, termed *polarization birefringence* by Engheta and Jaggard. [50] As a result of these mode propagation constants, an RCP wave propagates through a chiral medium with phase velocity $v_+ = \omega/k_R$, while an LCP wave propagates with $v_- = \omega/k_L$. The different phase velocities between the two circular polarization states implies that a linearly polarized light wave cannot transverse the chiral media without its polarization state being altered in the process. This results in a chiroptically responsive material, whereby for linearly polarized light the polarization plane is rotated about the propagation axis as the light wave propagates. This is referred to as the *optical rotation* or *optical rotatory dispersion* (ORD).[51–57] The optical rotation is quantified by a rotation in the polarization angle, which depends on the thickness of chiral material through which the wave propagates and the wavelength of incident light:

$$\gamma = \frac{\pi\, d\,(n_+ - n_-)}{\lambda_0}, \tag{1.13}$$

where $n_\pm$ is the refractive index of the chiral material (defined as $n_\pm = \sqrt{\mu\varepsilon} \pm \xi$), λ_0 is the vacuum wavelength, and d is the material thickness.[51] Similarly, γ can be quantified by comparing the difference between transmitted complex phases of incident light from each of the two circular polarization states: $\gamma = [\arg(T_+) - \arg(T_-)]/2$, where T_+ and T_- are the complex transmission coefficients for RCP and LCP waves, respectively. It is interesting to note that chiral materials can exhibit a negative refractive index—occurring when $\xi > \sqrt{\mu\varepsilon}$—even while ε and μ are both positive. This property makes chiral materials extremely promising for cutting edge optical applications involving negative index materials, such as lensing at resolutions below the diffraction limit.[58–60]

When k_L and k_R are complex, incident RCP and LCP waves experience differential attenuation when passing through the material, in addition to the differential phase velocity. This effect, whereby RCP and LCP waves are attenuated at different rates, is referred to as the *circular dichroism* (CD).[51, 61–64] The ellipticity can be used to represent the strength of the CD from the relative magnitude of the two transmitted polarization states. Ellipticity is calculated as:

$$\eta = \frac{1}{2}\sin^{-1}\left(\frac{|T_+|^2 - |T_-|^2}{|T_+|^2 + |T_-|^2}\right). \tag{1.14}$$

The strength of the CD can also be related to the optical chirality C, defined in a general way by Tang and Cohen in 2010,[33] as representing the degree of helicity in a general (not only CPL) electromagnetic field. [65–70] C is given by:

$$C = -\frac{\varepsilon_0\,\omega}{2}\,\mathrm{Im}(\mathbf{E}^\star \cdot \mathbf{B}). \tag{1.15}$$

It should be noted that for achiral structures a large CD response can be generated by anisotropy as well as the optical chirality. In practice, the two effects can be difficult to differentiate and are easy to mistakenly identify. Therefore in these systems, the chiral effect cannot be determined solely on the basis of the CD. The variation in the optical chirality, ΔC, for RCP (C^+) and LCP (C^-) electromagnetic fields ($\Delta C \equiv C^+ - C^-$) is directly proportional to the differential absorption rate for CPL interacting with a chiral material:

$$\begin{aligned} \Delta a &\equiv a^+ - a^- \\ &= -\frac{2}{\varepsilon_0}\,\mathrm{Im}(\xi)\,\Delta C, \end{aligned} \tag{1.16}$$

where Im(ξ) is the imaginary part of the electric-magnetic mixed dipole polarizability. [71] Tang and Cohen demonstrated theoretically [33] and experimentally [72] that a particular configuration of the incident CPL field can lead to enhancement in the optical chirality C, and similarly to an increase of the CD signal. In this scheme, two incident CPL fields with the same frequency and opposite handedness are superimposed with opposite propagation directions. These two fields will interfere with each other, generating a standing wave pattern. The resultant spatial field pattern is termed *superchiral* light. The electric energy density of the superchiral field is given by:

$$U_e(z) = \frac{\varepsilon_0}{2}\,[E_1^2 + E_2^2 - 2\,E_1 E_2\,\cos(2\,kz)], \tag{1.17}$$

where k is the wave vector, and E_1 and E_2 are the electric field amplitudes for the LCP (propagating right to left) and RCP waves (propagating left to right), respectively. At the nodes of the superchiral field, the electric dipole-allowed transitions are effectively suppressed, and the local chirality is enhanced with respect to the optical chirality in the incident field. This local enhancement of the chiral fields results in a local enhancement of the chiroptical activity of the material near the field nodes.[26, 72] However, it should be noted that by scaling inversely with the electric field energy density, as opposed to the total electromagnetic field energy density, Tang and Cohen's formalism can lead to limitations at the nanoscale.[73]

An important quantity in nanoscale chiroptics is the *dissymmetry factor*, first introduced by Kunh in 1930.[74] Considering the interaction between a chiral molecule and CPL, he showed theoretically that the chirality of a molecule is revealed in the difference between the extinction powers (P_{ext}) for two CPL waves with opposite handedness, normalized to their arithmetic average:

$$g_{CPL} = 2\,\frac{P_{ext}^{+} - P_{ext}^{-}}{P_{ext}^{+} + P_{ext}^{-}}. \tag{1.18}$$

Starting from this expression, Tang and Cohen[33] derived the dissymmetry factor for two mirror-image fields as a special case of **Equation 1.18**:

$$g = g_{CPL} \, \frac{c\, C}{2\, U_e\, \omega} \tag{1.19}$$

where c is the speed of light, C is the optical chirality, ω is the angular frequency, and U_e is the energy density of the electric field, as defined in **Equation 1.17**. This is the quantity which, in Tang and Cohen's approach, is maximized near the electric field nodes. Based on this expression there are two ways of effectively maximizing the chiral dissymmetry: maximizing the optical chirality, or minimizing the electric field energy density. However, the second approach has limitations in practical application. By only considering the electric and not the total electromagnetic energy density, it is possible for the g factor to be only artificially increased. This analysis ignores the contribution due to the magnetic energy density, which is not always valid, especially at or near the node of the electric field energy due to the conservation of energy.[73, 75] This may not correspond to a real advantage in terms of detection. In these situations, U_e should be replaced by the total electromagnetic field energy.

This optical chirality definition was recently further elaborated by Hanifeh *et al.*, translating the concept of CD at the nanoscale into the dissymmetry factor, and making the concept suitable for any type of electromagnetic field including structured light.[76] This formalism allowed the authors to discriminate and investigate the chirality of dielectric nanoparticles. Interestingly, this analysis introduces an upper bound for the helicity density2[76] Electromagnetic fields at this upper bound are called *optimally chiral*, which indicates that the optical chirality is maximized for a given time average of the energy density.

The electric and magnetic field components of optimally chiral fields satisfy the condition: [77]

$$\mathbf{E} = \pm\, i\, \eta_0\, \mathbf{H} \tag{1.20}$$

where η_0 represents the intrinsic wave impedance of the vacuum, and the sign determines the handedness. Additionally, the calculation of the dissymmetry factor for optimally chiral fields can be performed without explicitly knowing the helicity and energy densities of the field, as seen in the following expression:

$$g = -4\,\eta_0^{-1}\,\frac{\Re(\alpha_{em})}{\Im(\alpha_{ee})} \tag{1.21}$$

where $\Re(\alpha_{em})$ and $\Im(\alpha_{ee})$ are the real part of the EM polarizability and the imaginary part of the electric polarizability of the NP, respectively. [76] These recent innovations, including superchiral and optimally chiral light, have the potential to present a wide array of new applications for chiroptical systems.

1.3 Finite Element Method method for simulating metasurface

COMSOL Multiphysics provides a robust computational platform for numerically solving PDEs related to electromagnetic wave propagation and light-matter interactions. Its capabilities enable researchers to simulate various metasurface geometries and investigate their optical responses. By utilizing the software, researchers can gain valuable insights into light-metasurface interactions, optimize designs, and obtain predictions that can be compared with experimental results, facilitating the advancement of metasurface research and development. It is also possible to build with this software different metasurface geometries and make the light interact with them, in such a way to calculate, for example, the optical response, how the light interacts and other physical parameters. [78–81].

In this chapter, the simulations were carried out by using the COMSOL Multiphysics module for the Electromagnetic Waves, Frequency Domain (EWFD). To solve electromagnetic equations, COMSOL uses the Finite Element Method (FEM). Maxwell's equations in three dimensions are simplified by considering that fields vary sinusoidally in time at a known angular frequency and that all material properties are linear concerning field strength

[82]:

$$\nabla \times \left(\mu_r^{-1} \nabla \times \mathbf{E}\right) - \left(\frac{\omega^2}{c_0^2}\right) \epsilon_r - \left(\frac{i\sigma}{\omega\epsilon_0}\right) \mathbf{E} = 0, \tag{1.22}$$

where μ_r, ϵ, and σ are the relative permeability, the relative permittivity, and the electrical conductivity related to materials, respectively. The equation is solved for $\mathbf{E} = E(x, y, z)$ from which the other physical quantities can be obtained. The COMSOL module used gives the possibility to choose the electric displacement field model: refractive index is the default option used. It is possible to set the real and imaginary parts of the refractive index, called n and k, and the relative permittivity:

$$\epsilon_r = (n - ik)^2 \tag{1.23}$$

To simulate the metasurface, it was chosen a 3D geometry consisting of a parallelepiped with a height six times the unit cell dimension a, where a must be comparable with the incident wavelength. Every single block consists of three main parts, starting from the bottom: (a) the glass with a refractive index $n_{glass} = 1.5$; (b) the single right-handed gold helix (Johnson and Christy refractive index) and (c) the surrounding medium with a variable refractive index n_{medium}. To create a wave diffusion environment an input ($Port1$) and an output port ($Port2$) are used, respectively one on the top for the emitted radiation and the other on the bottom for the detection. To ensure the infinity conditions in the (x, y) plane, the Periodic Boundary Conditions (PBCs) are applied to the surfaces along the x-y directions of the blocks. To simulate the repeated single unit cell the Floaquet periodicity is used which is useful in frequency domain problems. In addition to PBCs, Perfect Matched Layers (PMLs) are introduced into the simulated system, to reproduce an absorbing boundary condition at the block extremes. The equations are solved by discretizing the problem, creating a dense mesh with control over the single components of the constructed geometry (Figure 1.1). In particular, for this work an "extra–fine" mesh has been chosen, that consists of free triangular and tetrahedral geometry with 82717 domain, 8024 boundary, and 710 edge elements. The ideal mesh should preferably have the smallest component dimension of approximately one-half wavelength of the wave.

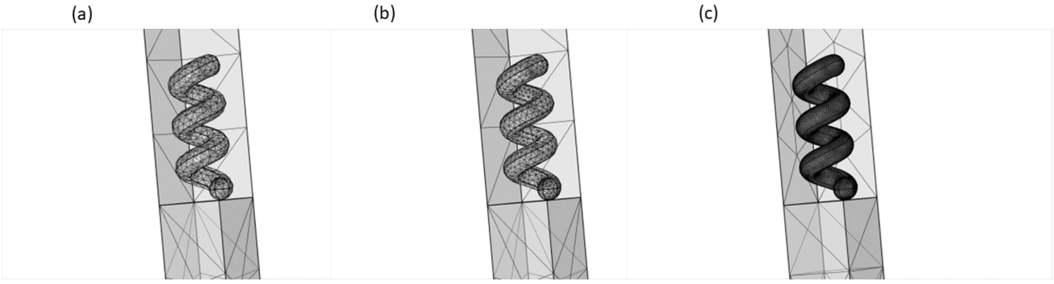

Figure 1.1: A sketch of the mesh directly controlled from the physics of COMSOL Multiphysics in the two extreme states and in the middle one **(a)** extremely coarse **(b)** normal, and **(c)** extremely fine.

The polarization (linear, circular, and elliptical) and the incident angle of the impinging radiation can be suitably selected [83], depending on the particular optical property to be investigated. In the first part of the numerical analysis, Transverse Electric (TE) and Transverse Magnetic (TM) polarization out of the plane, were used, with the field amplitude:

$$\mathbf{E}_0 = \begin{pmatrix} 0 \\ 0 \\ 1 \end{pmatrix}, \mathbf{H}_0 = \begin{pmatrix} 0 \\ 1 \\ 0 \end{pmatrix} \tag{1.24}$$

In the second part of the numerical investigation, Left and Right Circularly Polarized (LCP and RCP) light have been propagated by setting the following amplitude:

$$\mathbf{E}_0 = \begin{pmatrix} 1 \\ -1i \\ 0 \end{pmatrix}, \mathbf{E}_0 = \begin{pmatrix} 1 \\ 1i \\ 0 \end{pmatrix} \tag{1.25}$$

The top port boundary condition propagates a plane wave at the specified incident angle θ and computes the reflected light, while the bottom one calculates the transmitted light. Through the coefficient of the Scattering Matrix S

it is possible to evaluate different optical parameters, such as the Reflectance (R), Transmittance (T), and Absorption (A) of the modeled structure. In particular: (i) the S_{11} parameter provides information regarding the amount of light reflected compared to that sent from the input $Port1$; while (ii) the S_{21} parameter quantifies how much of the transmitted light reaches the output $Port2$ [29]. The equations for the two parameters are shown below:

$$S_{11} = \frac{\int_{port1}((\mathbf{E_C} - \mathbf{E_1}) \cdot \mathbf{E_1^*})dA_1}{\int_{port1}(\mathbf{E_1} \cdot \mathbf{E_1^*})dA_1}, \tag{1.26}$$

$$S_{21} = \frac{\int_{port2}((\mathbf{E_C} - \mathbf{E_2}) \cdot \mathbf{E_2^*})dA_2}{\int_{port2}(\mathbf{E_2} \cdot \mathbf{E_2^*})dA_2} \tag{1.27}$$

where E_C is the computed electric field equal to $E_C = \sum_{i=1} S_{i1}\mathbf{E_i}$. The fields are normalized concerning the integration of the power flow across each port cross section A_1 and A_2, respectively. The absorbance can be easily derived by knowing the other two optical quantities as $A = 1 - (T + R)$.

1.4 High sensitivity of chiral metasurfaces

In the study presented, Figure 1.2 (a) showcases a single structure under investigation, with its physical dimensions clearly marked. The unit cell dimension, denoted as a, establishes the fundamental size of the structure. The wire radius, labeled as r, measures 16 nm, while the helix radius, indicated as R, is 25 nm. The axial pitch, denoted as p, represents the spatial separation between two turns of the helix and is measured at 60 nm. Additionally, the number of pitches, represented by N, and the incidence angle of the helix axis, denoted as θ, contribute to the comprehensive characterization of the structure. These dimensions serve as critical parameters for investigating the behavior and properties of the analyzed structure within the scope of the study. Some of these parameters were varied to investigate the influence on the number and sharpness of resonances and to find the optimal conditions for highly effective refractive index sensing; in particular, the in-plane (a) and out-of-plane (N) periodicity were varied. Figures 1.2(b) and 1.2(c) show the resulting right-handed helical array for two values a= 100 nm and a= 250 nm, respectively.

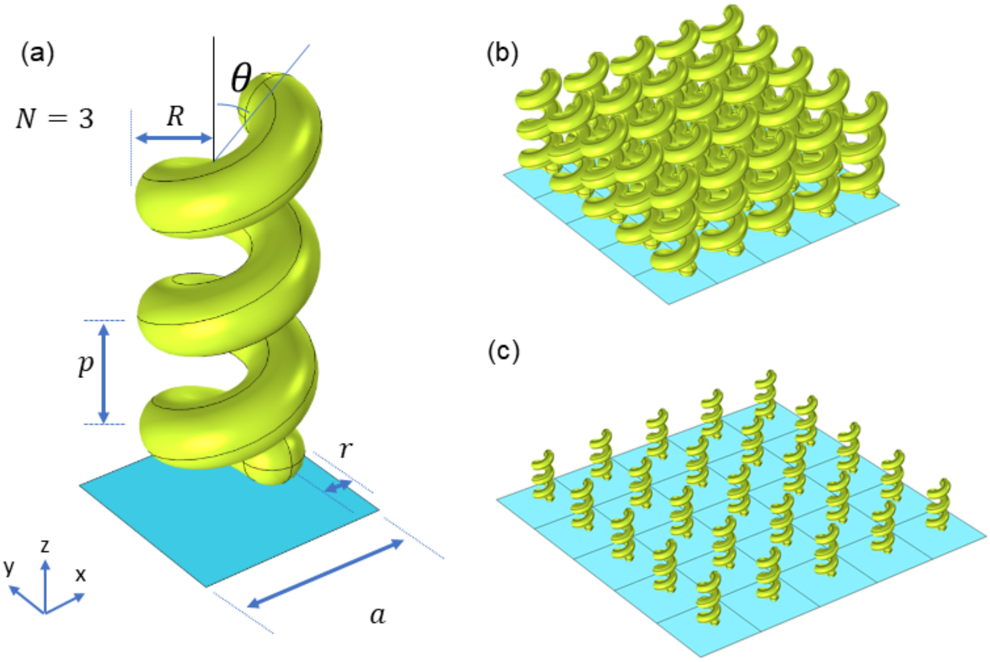

Figure 1.2: **(a)** Geometry of one lateral unit cell of the out-of-plane chiral structure composed of a right-handed Au helix on a glass substrate, the relevant structure parameters are illustrated: wire radius (r), helix radius (R), axial pitch (p), and the lattice constant (a). The out-of-plane periodicity is indicated with N. Geometry of the chiral metasurface for **(b)** a = 100 nm and **(c)** a= 250 nm.

Figure 1.3 (a-c) shows the normalized absorption maps as a function of three different parameters a, N, and θ in the wavelength range from 400 nm to 1300 nm. The tested values for a are 100, 150, 200, and 250 nm; for N they are 1, 2, 3, and 4 and for θ they are 40, 50, and 60°. Following the results obtained by varying the first parameter a (see Figure 1.3 (a)), it was decided to choose 250 nm as the in-plane periodicity of the helical array to ensure three distinct, intense, and narrow resonances in the wavelength range between 750 and 1300 nm. Although the most intense absorption band was found in the region between 400 - 600 nm, this region was excluded from the other analyzes because it was not of interest for two reasons: (i) the spectral band is broad and therefore not ideal for sensing, (ii) the visible region is the region where most bio-molecules absorb, so it may also affect analyte properties and cause signal overlap. Once the in-plane periodicity a was determined, the influence of the out-of-plane periodicity N was evaluated. From this analysis (see Figure 1.3(b)), it was found that the most intense modes were found in the same wavelength range as before for N equals 3. This value is also perfect for the purpose of detecting the refractive index of a surrounding medium, as it allows for a sufficiently large and extended out-of-plane sensing [29]. Finally, the effect of the angle of incidence θ was investigated (see Figure 1.3(c)) and it was found that the value that ensures the best performance in terms of absorption in the range 750-1300 nm was 50°. It can be noted that even an incident angle of 60° could be considered as it provides intense resonances, but the best compromise between the intensity and the width of the resonances in the range of 750 - 1300 nm is ensured by $\theta = 50°$.

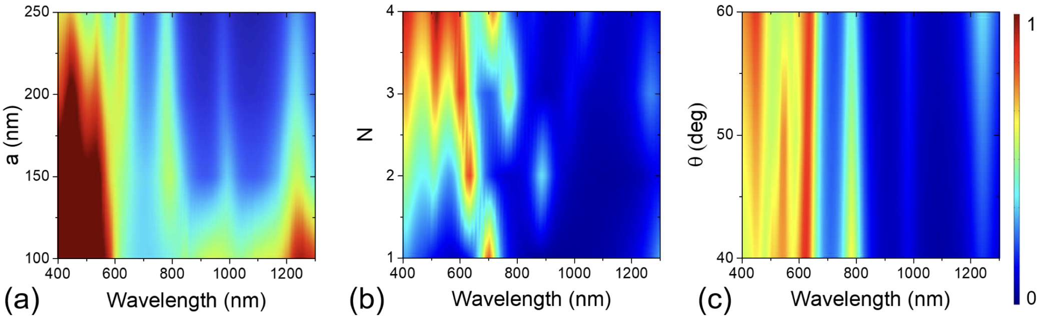

Figure 1.3: Normalized absorbance map of the plasmonic metasurface as a function of **(a)** the in-plane periodicity a in the range 100 nm – 250 nm and **(b)** the out-of-plane periodicity N in the range 1 – 4. **(c)** and the angle of incidence in the range 40° – 60°.

To test the ability of this plasmonic metasurface as a highly sensitive refractive index sensor, the molecule 1,2,3-Propantriol (glycerol) was selected as the model analyte to be detected. Various percent concentrations of glycerol dissolved in a water solution were tested (2.1, 8.5, 17.5, 38.2, 59.0, 69.2, 82.4%), corresponding to as many different refractive indices (1.345, 1.375, 1.401, 1.437, 1.455, 1.461, 1.467) [84]. Spectral shift in terms of wavelength change represents the easiest and most reliable way to perform refractive index sensing compared with intensity shift. This is related to the influence of surrounding media on the resonance condition that reflects it in the spectral shifts, more specifically on the dielectric permittivity [22]. The parameters carefully chosen by conducting the first parametric analysis (a=250 nm, N=3, $\theta = 50°$), made it possible to obtain a spectrum with three narrow and intense absorption lines in the infrared spectral range. Indeed, the tailored configuration of the periodic structure offers better spectral response with multiple resonant peaks in particular at $792, 957$, and 1173 nm, as it can be seen in Figure 1.4(a); allowing to cross-check and compare the wavelength interrogation with multiple peaks with more reliable results.

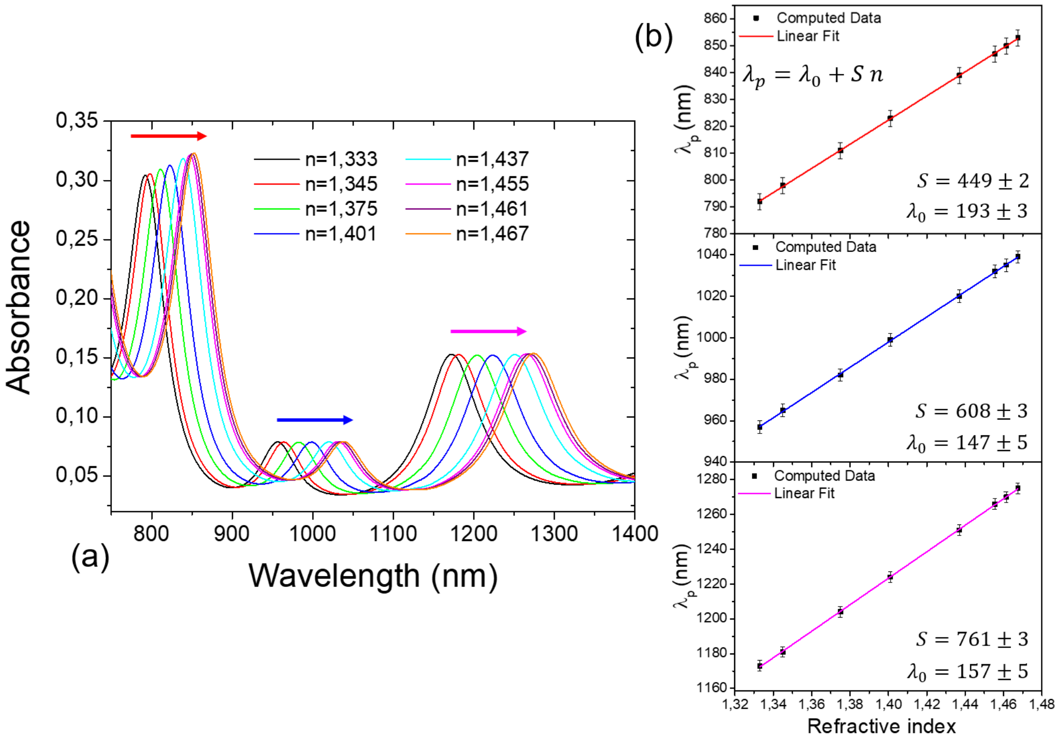

Figure 1.4: **(a)** Spectral characterization of the plasmonic metasurface: absorbance spectra calculated for different concentrations of 1,2,3-Propantriol for a=250 nm; **(b)** linear fit of the peak wavelength plotted versus the refractive index of the medium for the three resonant modes. The fitting equation is $\lambda_p = \lambda_0 + Sn$; the correlation coefficient is $R = 0.99$ for the three fits.

In Figure 1.4 (a) the three arrows indicate the gradual red shift of the resonance peaks registered at a constant increase of the refractive index from 1.333 (water) to 1.467 (82.4% of glycerol), while in figure1.4 (b) the corresponding peak positions are given as a function of the refractive index. The three plots (see figure 4.4b, top, middle, and bottom panels) show linear behavior between λ_p and n (black squares are the calculated data points and straight lines are the linear fits). For sensing applications, a linear change of the λ_p is usually preferable for refractive index of a given unknown medium [22]. From the slope of the fitting equation $\lambda_p = \lambda_0 + Sn$, the sensitivity S value for each peak can be derived. The spectral sensitivity (nm/RIU) is given by $S = \Delta n/\Delta\lambda$, where Δn is the change in the refractive index and $\Delta\lambda$ is the resonance peak shift. The calculated S values are found to be in the 449 - 761 nm/RIU range. In figure 1.4(b), the peak at 1173 nm is the one that mainly undergoes the redshift as the refractive index increases, resulting in a sensitivity value of 761 nm/RIU. It is worth noting that this mode, which is most affected by in-plane periodicity, is therefore dependent on the inter-structure interaction, as can be seen from the absorption map in figure 1.3(a). By calculating the Full Width at Half Maximum ($FWHM$) another sensing-related parameter can be deduced, the figure of merit ($FOM = S/FWHM$). The resulting FOM, for the three resonant peaks are in the range 9.9 - 12.3 RIU^{-1}, by taking into account the average $FWHM$ values.

The calculated values obtained in this study exhibit similarities within the range of values reported in other studies [24, 85, 86], which employed metasurfaces of distinct geometries such as L-shaped, U-shaped, and spiral G-shaped structures. In Figure 1.5 the distribution of the electric field enhancement ($\mathbf{E}/\mathbf{E}_0$) on the helix surface at the three resonance peaks were simulated. A significant enhancement of the electric field can be appreciated for the absorbance peak at 792 nm (max 8.57), at 957 nm (max 5.98), and 1173 nm (max 5.68).

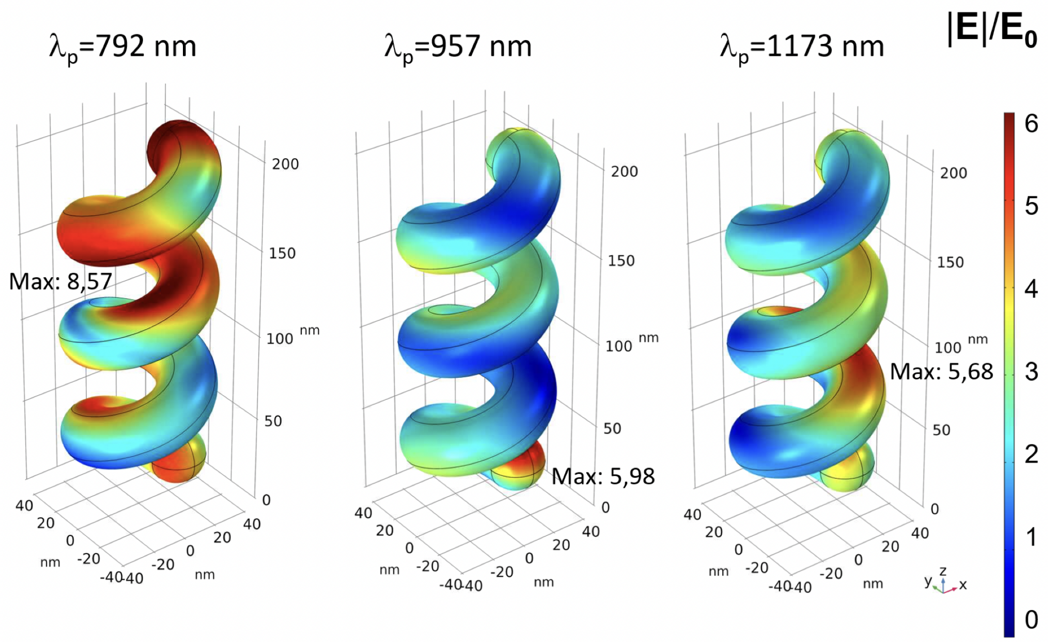

Figure 1.5: Electric field enhancement ($\mathbf{E}/\mathbf{E}_0$) on the helix surface at the three λ_p: 792 nm, 957 nm, and 1173 nm.

The intrinsic chiral nature of the plasmonic metasurface allow to consider dichroic signals for sensing applications. It is possible to exploit the absence of intrinsic mirror symmetry of the structure and the corresponding difference in its interaction with circularly polarized light. In these numerical studies both Left-handed Circularly Polarized (LCP) and Right-handed Circularly Polarized (RCP) are used to interact with the structure, with an incident angle of 50°. Figure 4.8 (a) and 1.6 (b) show the Absorbance and Transmittance curves for the plasmonic metasurface characterized by an in-plane periodicity a=250 nm, considering only water as the surrounding medium. The right-handed structure demonstrates a stronger coupling with Right-Circular Polarized (RCP) light compared to the Left-Circular Polarized (LCP) wave. This enhanced coupling results in absorbance modes that are more pronounced and peaked compared to the LCP case, indicating a more efficient interaction between the light and the metasurface. In Figure 1.6 (c) the Circular Dichroism (CD) is reported, it is calculated using the relations, CD_{Abs}=A_{LCP} - A_{RCP}, in the absorption mode, by varying the refractive index of the medium surrounding the helices, for values corresponding to 38% and 82% of glycerol in water.

Figure 1.6 (c) show CD spectra that can be identified corresponding to maxima (λ_{M1}= 590 nm, λ_{M2}= 955 nm), minima (λ_{min1}= 665 nm, λ_{min2}= 794 nm), and zero dichroism points (λ_{01}= 626 nm, λ_{02}= 899 nm). There is a shift of the modes, changing the refractive index and it is possible to calculate the bulk refractive index sensitivity S of the structure. In particular, we found S in the range 252 – 614 nm/RIU with a FOM in the range 6 – 11 RIU^{-1}. The proposed chiral plasmonic metasurface based on 3D gold helices may find specific applications as refractive index sensors for detecting different molecules, thanks to the high-sensitivity achieved in the sensing performance.

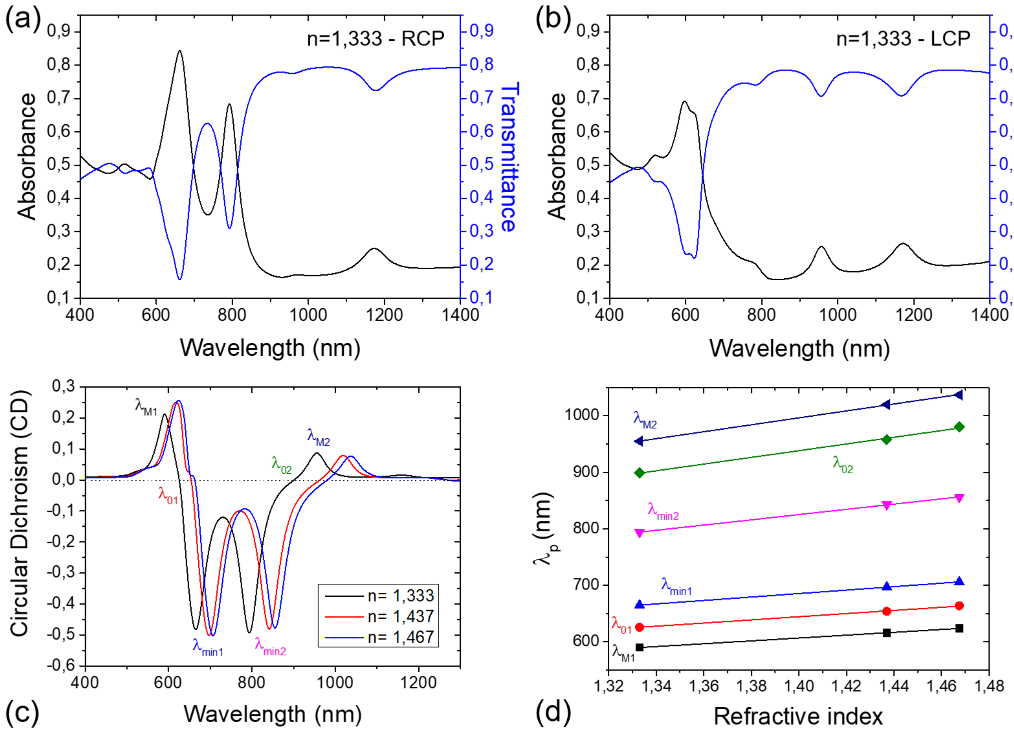

Figure 1.6: Absorbance and Transmittance spectra of the plasmonic metasurface for **(a)** Right Circular Polarized (RCP) and **(b)** Left Circular Polarized (LCP) light. **(c)** CD spectra calculated in a 1,2,3-Propantriol - water solution at different molar concentrations ranging from 0% (corresponding to water - n=1.333) to 82% of 1,2,3-Propantriol in water (n=1,467). **(d)** Linear fit of the peak wavelength plotted versus the refractive index of the medium.

1.5 Conclusion

We proposed and conducted a numerical exploration of a chiral plasmonic metasurface composed of an array of 3D right-handed gold helices. The objective is to understand the impact of various geometric parameters on the occurrence of multiple resonant modes. Through a systematic parametric analysis, we identified the optimal combination of parameters (a=250 nm, N=3, θ=50°) that enables the design of a metasurface capable of exhibiting distinct resonance modes within the infrared (IR) region of the electromagnetic spectrum. This specific configuration proves advantageous for developing minimally invasive refractive index biosensing techniques, as it avoids overlap with the absorption bands of most biomolecules found in the ultraviolet-visible (UV-VIS) range. Furthermore, the sensing performances were tested by simulating different concentrations of glycerol in the surrounding medium. The calculated sensing sensitivity and the FOM values in the range of 450 - 761 nm/RIU and 9.9 - 12.3 RIU^{-1} respectively, suggest that the tailored metasurface can be employed for surface sensing. In addition, the designed metasurface exhibits highly chiral behavior with tunable multibands CD, covering a broad spectral range from 400 to 1300 nm. The remarkable optical properties exhibited by this 3D chiral plasmonic metasurface present exciting opportunities for developing a highly sensitive surface. Integration of this metasurface into a compact chip can enable multifunctional capabilities such as optical absorption, circular dichroism, and refractive index sensing. This advancement holds the potential to revolutionize the field of optical sensing, providing a platform for robust and versatile sensing devices that can be integrated into various applications.

Chapter 2

Fano Resonance Optical Coatings

Today, optical coatings are of great importance in our daily life for the production of optical components. In this chapter, the main aspects of ellipsometric spectroscopy and the main numerical methods used to design, predict, and study the optical and photonic behavior of multilayer thin films are presented. In particular, a type of optical coating that exhibits photonic Fano resonance, called Fano-resonant optical coating (FROC), is presented. After a brief history of the discovery of Fano resonance, the theory on which this important resonance is based and how it can be applied to optical coatings will be presented. Various prototypes of optical coatings consisting of multiple layers of thin films simulated by the finite element method using COMSOL software are described. After determination, the samples are prepared by physical vapor deposition technique and analyzed by ellipsometric spectroscopy and spectrophotometry. The experimental results are in agreement with the expected simulated results. Applications can range from use as a beam splitter (they transmit a part of radiation at the same wavelength), to use in photovoltaic cells in such a way that they reflect sunlight and at the same time store radiation that can be used in the dark. Another application is to be used as biosensors to detect cells, such as cancer, or bacteria.

2.1 Introduction

In the early 1930s, amidst the bustling scientific community in Rome, an Italian physicist named Ugo Fano found himself captivated by the mysterious asymmetrical lineshapes he observed in the spectra of gases. Fano was an esteemed member of Enrico Fermi's group, a prestigious gathering of brilliant minds pursuing groundbreaking research. Intrigued by Fano's observations, Fermi recognized the importance of understanding and theoretically describing these peculiar lineshapes. He encouraged Fano to embark on a journey of exploration, urging him to uncover the underlying principles governing the behavior of these spectral features. Fuelled by Fermi's guidance and his own unwavering curiosity, Fano delved into the depths of this captivating phenomenon. After years of meticulous research, Fano finally presented his findings to the scientific community in 1935, publishing a seminal paper in the esteemed journal Nuovo Cimento. This groundbreaking work, titled *Sullo spettro di assorbimento dei gas nobili presso il limite dello spettro d'arco*, unveiled Fano's comprehensive theoretical framework for describing the absorption spectra of noble gases near the arc spectrum limit. Within its pages lay the key to unraveling the enigmatic lineshapes that had puzzled scientists for so long. As a tribute to his extraordinary contributions, this distinctive spectral feature became known as the "Fano resonance." Fano's name would forever be intertwined with this phenomenon that he had unraveled, illuminating a path toward a deeper understanding of light-matter interactions. Over the decades, the Fano resonance has become a cornerstone in the realm of optics and spectroscopy, finding applications across a multitude of fields. It's unique lineshape and intriguing interference effects have empowered scientists to explore and exploit its potential in various domains, from nanophotonics to quantum technologies. Fano's work serves as a testament to the power of curiosity, the pursuit of knowledge, and the guidance of mentorship. His unwavering dedication and meticulous research laid the foundation for future generations to build upon, fueling a continuous quest for unraveling the mysteries of light and matter. Today, scientists around the world continue to delve into the intricacies of the Fano resonance, unlocking its secrets and harnessing its power for transformative advancements in technology, medicine, and fundamental scientific understanding. From the humble origins of a scientist's observation to a renowned phenomenon bearing his name, the Fano resonance stands as a testament to the profound impact that a single individual's dedication and scientific acumen can have on the course of human knowledge. [87]

To explain the unusual shape of these peaks in the absorption spectrum of the noble gases, Fano considered two effects of the photoionization of atoms: the excitation of the atom both in a state of ionization above the threshold and in a discrete level such for which can be spontaneously ionized. The absorption is obtained by considering the interaction between the term itself and the continuum.

The Fano resonance emerges as a result of the intricate interference between a discrete quantum state and a continuum band of states. This interference gives rise to an asymmetrical spectral lineshape, offering a unique window into the behavior of quantum systems. The absorption spectrum $\sigma(E)$, is manifested with the classical shape described by the Fano's formula:

$$\sigma(E) = D^2 \frac{(q+\Omega)^2}{1+\Omega^2} \tag{2.1}$$

where E is the energy, $q = cot\delta$ is the Fano parameter, δ is the phase shift of the continuum, $\Omega = 2(E - E_0)/\Gamma$, where Γ and E_0 are the resonance width and energy respectively, and $D^2 = 4sin^2\delta$.

The q parameter is responsible for the symmetrical or asymmetrical shape of the Fano profile, but there are two important specific cases in this theory. If $q \mapsto \infty$, i.e. if the external perturbation does not couple with the continuum, the Fano form is reduced to a symmetric Lorentzian one, $\sigma_L(\Omega) \sim \frac{1}{1+\Omega^2}$. The other limit occurs when $q = 0$ then the Fano profile becomes a quasi-Lorentzian antiresonance in the continuum $\sigma_L(\Omega) \sim \frac{\Omega^2}{1+\Omega^2}$.

The advantages of using a Fano resonance, compared to others, such as the Lorentzian one, are: 1) the flexibility in which the shape of the resonance can be varied and designed for a Fano device; 2) it has a dip in the continuous spectrum that goes to zero at a particular frequency ($q+\Omega=0$), this perspective opens up numerous scenarios such as cloaking; 3) a small perturbation can cause a pronounced amplitude and phase shift in the transmittance, reflectance, and extinction spectra; 4) it is characterized by a nontrivial sharp spectral dependence of the phase that can be used in various devices.

These features make an effectively tuned and well-designed Fano resonance as powerful tool for many applications including, but not limited to high-sensitivity sensing, all-optical switching, low-loss slow-light devices, low-threshold lasing, high-performance modulators and absorbers, narrowband filters, SERS applications, and invisibility cloaking and nonlinearity enhancement.

2.2 Two coupling oscillators theory

To elucidate the essence of the Fano resonance, it is crucial to delve into the theory of two coupled oscillators. This theory can be succinctly represented by a matrix equation that encapsulates the dynamics of the system. Consider a scenario where two oscillators are coupled together, interacting through their motion or vibrations. This coupling gives rise to a coupled oscillator system, which can be mathematically described using a matrix equation. Let's represent the state of the coupled oscillators at a given time using a column vector, and the coupling between them with a coupling matrix: [88]

$$\begin{pmatrix} \omega_1-\omega-i\gamma_1 & g \\ g & \omega_2-\omega-i\gamma_2 \end{pmatrix} \begin{pmatrix} x_1 \\ x_2 \end{pmatrix} = i \begin{pmatrix} f_1 \\ f_2 \end{pmatrix} \tag{2.2}$$

where x_1 and x_2 are the oscillator amplitudes, and ω_1 and ω_2 are the resonant frequencies, γ_1 and γ_2 are the damping coefficients and f_1 and f_2 are the external forces with the driving frequency ω. g is the coupling constant that describes the interaction between the oscillator. With this system of equations, it is possible to have different resonance effects, in addition to the Fano one. Some examples of weak-coupling regimes are: **Electromagnetically induced transparency (EIT)**, which is a special case of Fano resonance. It occurs when the frequencies of strongly and weakly damped oscillators match, $\omega_1 = \omega_2$ and consequently $q = 0$, the transmission can be resonantly restored by the coupling to the undamped mode with the opposite phase, canceling the losses out. [89] **Borrmann effect** which is be described in the spatial domain, so the frequencies are to be replaced by the wave number. In this case, $\omega_1 = \omega_2$ and $\gamma_1 = -\gamma_2$ describe the wave attenuation due to absorption, and their opposite signs take into account the left and right propagating waves decay in opposite directions. [90] **Kerker effect** which doesn't require direct coupling between the oscillating modes. The coupling constant is g is zero due to the equality excitation amplitudes $f_1 = f_2$ that are different from 0. It is possible to remove light scattering either in backward (Kerker 1st condition) or forward (Kerker 2nd condition) direction. [91]

Fano resonance occurs in the weak coupling regime and when only one of the two oscillators (with large damping) is driven ($f_1 \neq 0, f_2 = 0$). An analogy of this resonance, in classical mechanics, is represented by two coupled damped oscillators (pendulums) with an external force f_1 applied to only one of them. The amplitude of the driven oscillator 1 in the spectral vicinity of the resonance of oscillator 2 can be written in the form:

$$\left|x_1(\Omega)\right|^2 \approx \left|f_1^2\right| \frac{\gamma_1^2}{(\omega_1 - \omega_2)^2 + \gamma_1^2} \frac{(\Omega + q)^2}{\Omega^2 + 1} \tag{2.3}$$

where:

$$\Omega = \left[\omega - \omega_2 + \left(\frac{g^2}{\gamma_1}\right)\frac{(\omega_1 - \omega_2)}{1+q^2}\right] \frac{\gamma_1(1+q^2)}{g^2} \tag{2.4}$$

is the dimensionless frequency. The Fano parameter q determines the spectral shape and depends on the spectra detuning of the oscillator $\omega_2 - \omega_1$. The resulting spectra show typical asymmetry with a sharp change between a dip and a peak. The spectral shape depends on the phase shift γ between the oscillators encoded in the Fano parameter q.

2.2.1 Coupled oscillator theory for thin film optical coatings

The theory of the two coupled oscillators can also be extended to thin optical coating films. An example of the so-called Fano Resonance Optical Coating (FROC) is schematized in Figure 2.1(a). Resonator 1 is a lossy material with a refractive index $n_a = n_a^{Re} + in_a^{Im}$ and a thickness L_a, and the resonator 2 consists of a Metal-Dielectric-Metal (MDM) nanocavity, i.e. a thin metallic layer $n_m = n_m^{Re} + in_m^{Im}$ with a thickness L_m, a lossless dielectric film with refractive index n_d and thickness L_d, and for last a metallic layer. Defining the intensity ratio for a generic resonator $k-th$ as $A_k = (\frac{E_k}{E_k^i})$, where E_k and E_k^i are the inside and injected fields respectively. The intensity ratio values for the two resonators are:

$$A_1(\omega) \approx \frac{1}{1 - \left|r_{a0}r_{am}\right| e^{-2Im[\phi_a(\omega)]} e^{i\{2Re[\phi_a(\omega)]+\phi_{a0}+\phi_{am}\}}} \tag{2.5}$$

and

$$A_2(\omega) \approx \frac{1}{1 - \left|r_{dm}\right|^2 e^{2i[\phi_d(\omega)+\phi_{dm}]}} \tag{2.6}$$

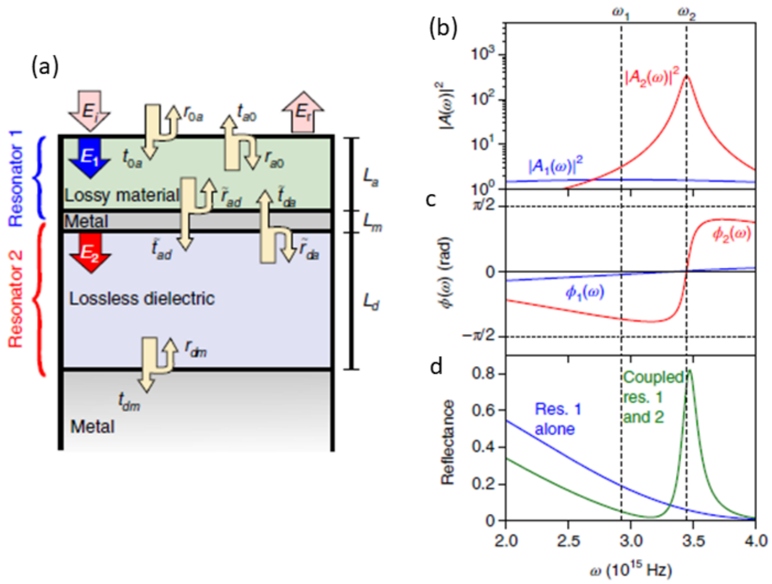

Figure 2.1: **(a)** Representation of the FROC structure consisting of two weakly coupled resonators, where resonator 1 (the top two layers consisting of a lossy material and a metal) represents a broadband absorber and resonator 2 (layers from 2 to 4 consisting of a metal, a dielectric and a metal) represents a narrowband absorber. The two resonators share a metal layer that determines their coupling strength. **(b)** The calculated oscillator intensities and **(c)** the corresponding oscillator phase. **(d)** The reflectance from the whole system of two coupled resonators (green). The reflectance of just resonator 1 (lossy material on a metal substrate) is shown in blue. **Readapted with permission from** [92]

In Figure 2.1 (b) the intensities for the two oscillators are shown with the blue and red lines, the dashed lines instead represent the resonant frequencies. The oscillator phase $\phi_i(\omega)$ is reported in Figure 2.1 (c), it is evident that the phase in resonator 1 varies slowly, on the contrary in resonator 2.

The coupling between E_1 and E_2 occurs through the off-diagonal terms in the matrix. From equation 2.7, the reflectance of the coupled oscillators appears with a peak at ω_2, Figure 2.1 (d).

$$\begin{pmatrix} \frac{1}{A_1(\omega)} & -r_{dm}\check{t}_{da}r_{a0}e^{i[2\phi_d(\omega)+\phi_a(\omega)]} \\ -\check{t}_{ad}e^{i\phi_a(\omega)} & \frac{1}{A_2(\omega)} \end{pmatrix} \begin{pmatrix} E_1 \\ E_2 \end{pmatrix} = \begin{pmatrix} t_{0a}E_i \\ 0 \end{pmatrix} \tag{2.7}$$

2.3 Ellipsometry

Ellipsometry is a highly valuable non-destructive optical technique employed for characterizing a wide range of materials. By illuminating the sample under investigation with a beam of polarized light at various angles, ellipsometry enables the determination of essential parameters such as the refractive index (n), extinction coefficient (k), and thickness (t) of the material. The key principle behind ellipsometry lies in the measurement of changes in the polarization state of light as it interacts with the sample. The incident light is typically polarized, meaning it oscillates in a specific plane. As this polarized light interacts with the material, its polarization state is modified due to the sample's optical properties. By analyzing the changes in the polarization state of the reflected or transmitted light, ellipsometry provides valuable information about the material's optical properties. These changes can be quantified using ellipsometric parameters, such as the amplitude ratio (Ψ) and phase difference (Δ) between the reflected or transmitted light's electric field components. It is notable that numerous optical parameters can be achieved by performing spectroscopic ellipsometry [93–96] and can be analyzed both thin films and bulk materials [97–99], growing film [100], surface roughness [101], and micro- and nano-structures on a surface [102–104]. Ellipsometry measures a change in polarization as light reflects or transmits from a material, no special reference samples are required.

The measureables value Ψ and Δ are related to the ratio of Fresnel reflection coefficients $\check{r_p}$ and $\check{r_s}$ for p and s state of polarized light respectively, according to the following formula:

$$\rho = \frac{\check{r_p}}{\check{r_s}} = tan(\Psi)e^{i\Delta} \tag{2.8}$$

$tan\Psi$ is the ratio of the intensity of the incident field to the reflected one, for both states s and p polarization and Δ is the difference between the two phase shifts of the reflected and incident waves. The angle Ψ can assume a value between 0 and 90 degrees (because the amplitudes of the fields are positive), in particular, it is 0 when $\left|r_p\right| = 0$ and it is 90° when $\left|r_s\right| = 0$. The angle Δ can be any value between 0 and 360 degrees. The two parameters are independent and have no immediate physical meaning (pseudo angles), allowing to determine the optical properties of the substrate (index of refraction or complex dielectric function) or geometric properties such as the thickness of a film deposited on a known substrate. Ellipsometry is an indirect method, i.e. in general the measured Ψ and Δ cannot be converted directly into the optical constants of the sample. Models can be physically based on energy transitions or simply free parameters used to fit the data. By varying the unknown parameters (e.g., thickness and optical constants), a good model can be generated, that describes the actual physical structure of the sample. The goodness of the used model is related to the Mean Squared Error (MSE), which indicates how large is the difference between the experimental data and the theoretical data:

$$MSE = \sqrt{\frac{1}{2N-M}\sum_{i=1}^{N}\left[\left(\tfrac{\psi_i^{mod}-\psi_i^{exp}}{\sigma_{\psi,i}^{exp}}\right)^2 + \left(\tfrac{\Delta_i^{mod}-\Delta_i^{exp}}{\sigma_{\Delta,i}^{exp}}\right)\right]} = \sqrt{\frac{1}{2N-M}\chi^2} \quad (2.9)$$

where N is the number of (ψ, Δ) pairs, M is the number of variable parameters in the model, and σ are the standard deviations on the experimental data points.

Figure 2.2 shows an ellipsometer consisting of a source consisting of two lamps covering a range of 200-1000 nm, a polarizer, an analyzer, a detector, and a compensator placed before the sample.

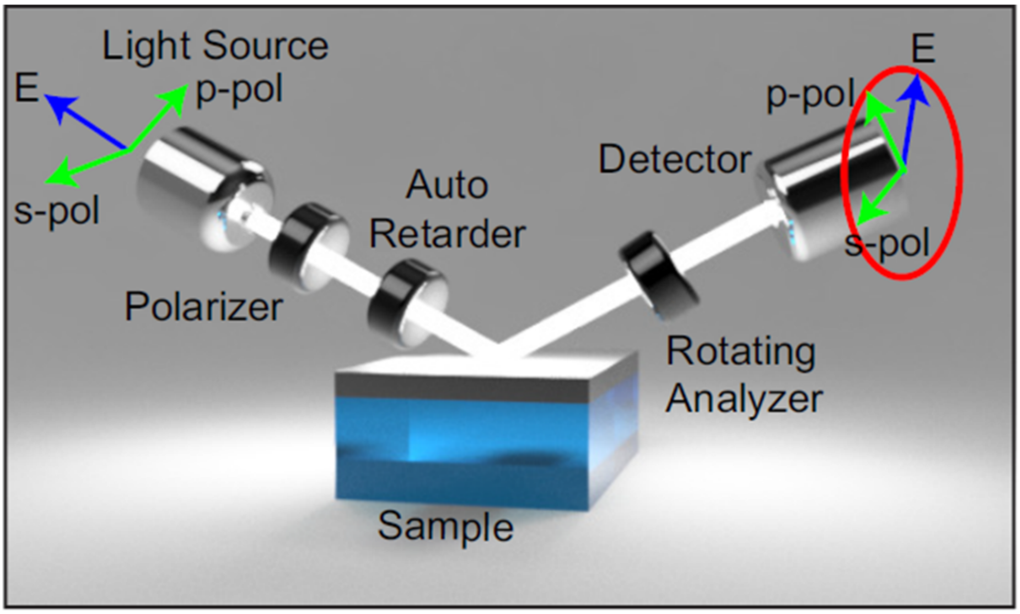

Figure 2.2: The sketch illustrates the essential components of an ellipsometer and depicts the electromagnetic wave comprising both polarizations. **Readapted with permission from** [80]

2.4 FROC simulations by using COMSOL Muliphysics

A Finite Element Method (FEM) analysis gives the possibility to solve, starting from the partial differential equations (PDEs) governing the given system, various physical conditions. For example, it is possible to simulate problems of elasticity and applied strains, thermal heating and transport, fluid mechanics and chemical transport, and last but not least, problems related to the electromagnetic wave propagation and light-matter interactions. [105, 106] Indeed, the proposed simulation for ellipsometric analysis has been performed by using the COMSOL Multiphysics platform, which gives the possibility to use a 2D or 3D environment.

Several multilayered systems were designed, fabricated, and then characterized by experimental ellipsometric analyzes. Figure 2.3 (a) shows a proposed FROC structure consisting of 1 mm glass, 100 nm Ag, a TiO_2 layer of variable thickness (t_2), representing the dielectric cavity and fixed at 50 nm for initial testing, 30 nm Ag, 15 nm Ti, and the surrounding medium is air ($n_{air} = 1$).Extensive simulations were conducted with the aim of optimizing the parameters and achieving narrow peaks in reflectance. By leveraging advanced computational techniques, researchers sought to fine-tune the system and maximize its performance. Figure 2.3 (b) and (c) show p-pol reflectance maps as a function of two different parameters of the incidence angle α and thickness (t) of the last Ti layer in the wavelength range 300-900 nm. The tested values for α are from 40° to 70° and for t are from 5 nm to 45 nm.

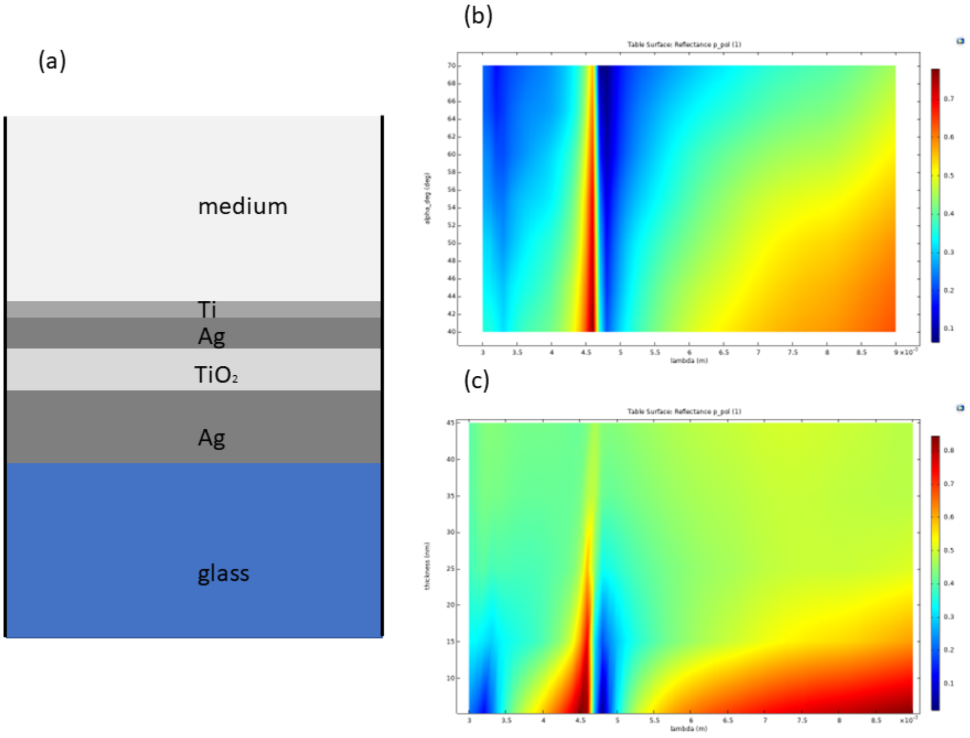

Figure 2.3: **(a)** Structure of proposed FROC **(b)** Reflectance p-pol map calculated by varying the incident angle α and the wavelength λ **(c)** Reflectance p-pol map calculated by varying the thickness t and the wavelength λ.

Following the results obtained by varying the first parameter, it was decided to choose 45° as the incident angle to guarantee distinct, intense, and narrow resonances at 460 nm.

Once the parameter α was determined and set, the next step involved evaluating the influence of the thickness (t) on the system's reflectance. By systematically varying the thickness and observing the resulting reflectance spectra, researchers sought to understand the impact of this parameter on the system's performance. Figure 2.3 (c) displays a color map that represents the intensity of reflectance as a function of the thickness values tested. The color map provides a visual representation of how the reflectance changes with different thickness values, allowing for a quick assessment of the system's behavior. Analyzing the color map, it becomes evident that at low thickness values, the reflectance intensity is higher. This indicates that the system exhibits stronger resonant behavior and enhanced light-matter interactions when the thickness is reduced.

Although another intense reflection band was found in the range between 750 - 900 nm, this region was excluded from the other analyses because it is broad for sensing and other applications.

In both maps (Figure 2.3), it is noted that a few nm away from the intensity peak, there is a minimum in reflectance which represents the typical shape of Fano resonance.

It is possible to shift the chosen Fano resonance to the desired wavelength, to enhance the signal or detect some molecules, [107–109] by varying the thickness t_2 of the dielectric material TiO_2. For this reason, some FROCs were simulated by varying t_2.

Figure 2.4 (a) shows the color map of the reflectance p-pol intensity as the thickness t_2 varies in the wavelength range between 300 nm and 800 nm.

It is evident that the reflectance maxima vary in wavelength as the thickness t_2 changes. This opens up an evident advantage in research in the optical fields such as in the manufacture of beam splitters, having a transmittance at the same wavelength, but also in biosensing and photovoltaic applications.

Figure 2.4(b) shows the reflectance spectra p-pol as the thickness t_2

varies. In each spectrum, it is evident the Fano resonance with the shape of a maximum followed by a minimum. As the thickness t_2 of the layer increases, there is a red-shift in wavelength.

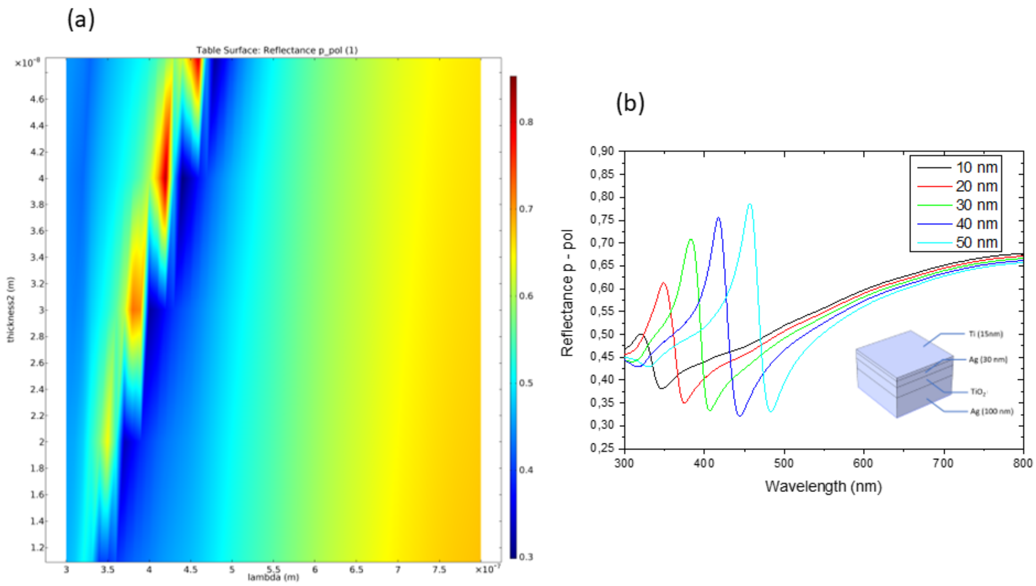

Figure 2.4: **(a)** Reflectance p-pol map calculated by varying the thickness t_2 and the wavelength λ **(b)** Reflectance p-pol spectra obtained calculated by varying the thickness t and the wavelength λ.

The numerical study revealed another fundamental feature: an increase in the intensity of the peaks as the thickness of the dielectric layer increases. This finding indicates that the interaction between light and the metasurface becomes stronger with greater thicknesses of the dielectric layer. The obtained reflectance peaks were found to occur at specific wavelengths, namely 320 nm, 350 nm, 380 nm, 417 nm, and 455 nm, respectively. These wavelengths correspond to the resonant modes supported by the metasurface structure. In this way, a linear trend for the calibration of the metasurfaces can be established, resulting in a coefficient of determination R-squared of 0.995.

The same study was performed considering the s-pole component of the polarization of the incident light and gave very similar results to the previous ones. Figure 2.5 (a) and (b) show the results obtained by varying the thickness t_2 in the wavelength range 300-800 nm.

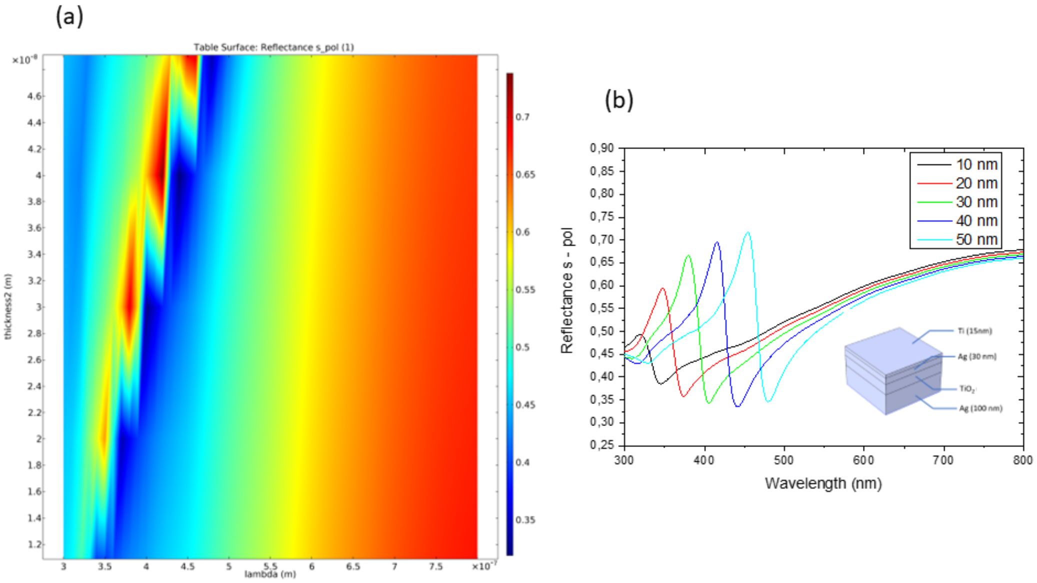

Figure 2.5: **(a)** Reflectance s-pol map calculated by varying the thickness t_2 and the wavelength λ **(b)** Reflectance s-pol spectra obtained calculated by varying the thickness t and the wavelength λ.

One possible application of these substrates is detection by changing the refractive index of the surrounding medium. This is very useful for dictating molecules and biomolecules. Figure 2.6 shows simulations of the FROC $Ag100nm, TiO_2 40nm, Ag30nm, Ti15nm$ for p-polarization at an angle of 45° by varying the refractive index from 1.33 to 1.47. As can be seen from the map (Figure 2.6 (a)), there is no shift in wavelength, but a linear trend of increasing intensity of the reflection peak can be followed.

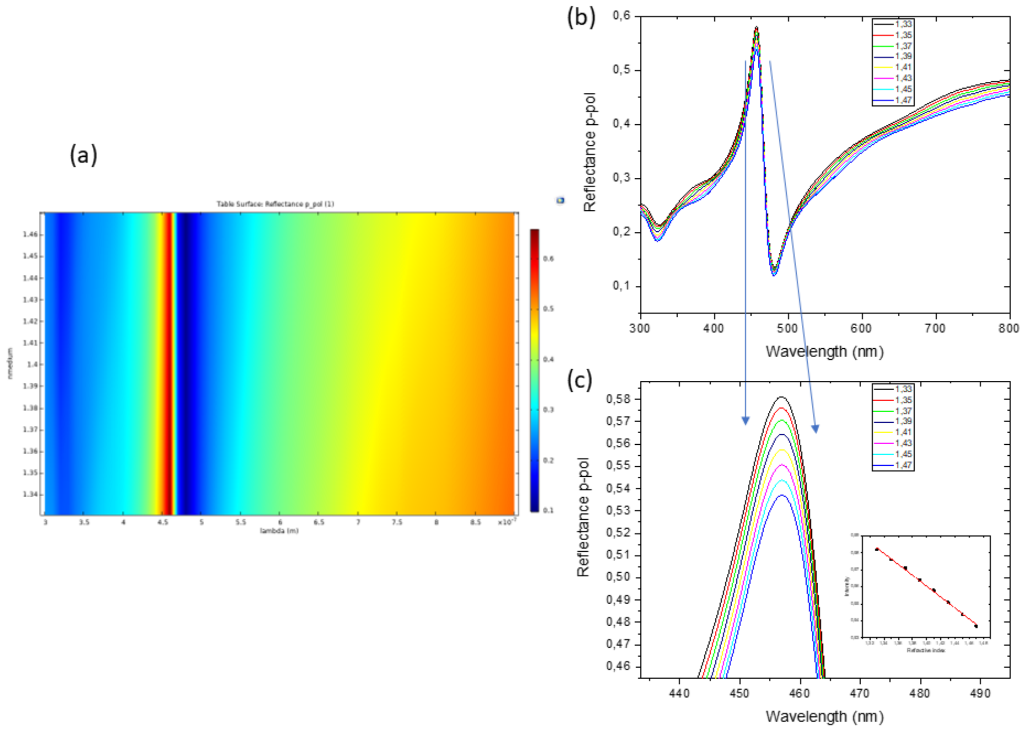

Figure 2.6: **(a)** Reflectance s-pol map calculated by varying the thickness t_2 and the wavelength λ **(b)** Reflectance s-pol spectra obtained calculated by varying the thickness t and the wavelength λ.

2.5 Fabrication and experimental analysis of FROCs metasurfaces

All samples were prepared experimentally using a sputtering (Kenosistec KS300C) with DC and RF cathodes. Sputter deposition is a physical vapor deposition (PVD) method for depositing thin films through the phenomenon of sputtering. [110–112] In this process, the material is sputtered from a target onto a substrate, e.g. a silicon wafer. One of the first widespread commercial applications of sputter coating, and still one of the most important today, was in the manufacture of computer hard disks. In the semiconductor industry, sputtering is widely used to deposit thin films of various materials in integrated circuit processing. Thin anti-reflective layers on glass for optical applications are also deposited by sputtering. Due to low substrate temperatures, sputtering is an ideal method for depositing contact metals for thin film transistors. Another well-known application of sputtering is low-emissivity coatings on glass used in double-glazed windows. The coating consists of a multilayer containing silver and metal oxides such as zinc oxide, tin oxide, or titanium dioxide. [113] A large industry has developed around the coating of tool-cutting edges with sputtered nitrides such as titanium nitride, creating the familiar gold-colored hard coating. Sputtering is also used as a process for depositing the metal layer (e.g., aluminum) in the manufacture of CDs and DVDs. The samples made are then analyzed using ellipsometry and spectrophotometry. Figure 2.7 shows the reflectance p-pol of FROC substrate formed by multilayer $Ag100nm, TiO_2$ variable $20, 30$, and $40nm$, $Ag30nm$, and $Ti15nm$ changing the angle of the incident from 45° to 65° step every 5°.

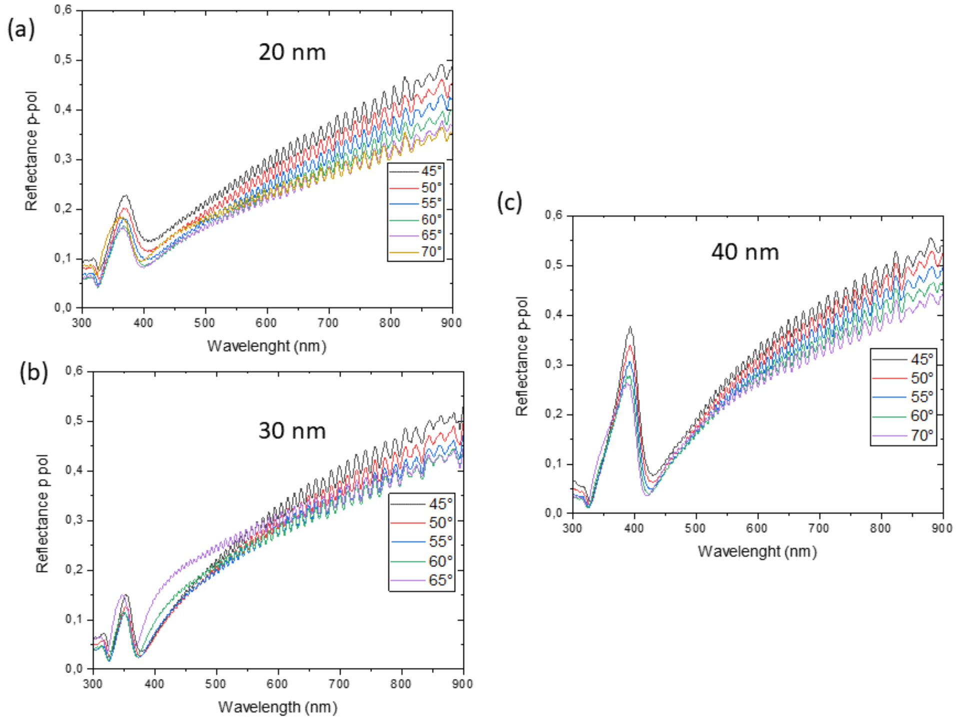

Figure 2.7: **(a)** Reflectance p-pol map calculated by varying the thickness t_2 and the wavelength λ **(b)** Reflectance p-pol spectra obtained calculated by varying the thickness t and the wavelength λ.

Experimental data are in accordance with the simulation foreseen in Figure 2.3(b), in fact, there is no shift in the reflectance peaks and the intensity is maximum for low value of incident angle. The found values of reflectance peaks in the wavelength range in the titania layer configurations of 20, 30, and 40 nm are 350, 370, and 395 nm respectively, which are values very close to those predicted by the simulations (350,380, and 417 nm). The trend is the same as that of the simulations. Some results may differ from COMSOL simulations compared to experimental data because the materials used may not be identical, especially the n and k values of each layer

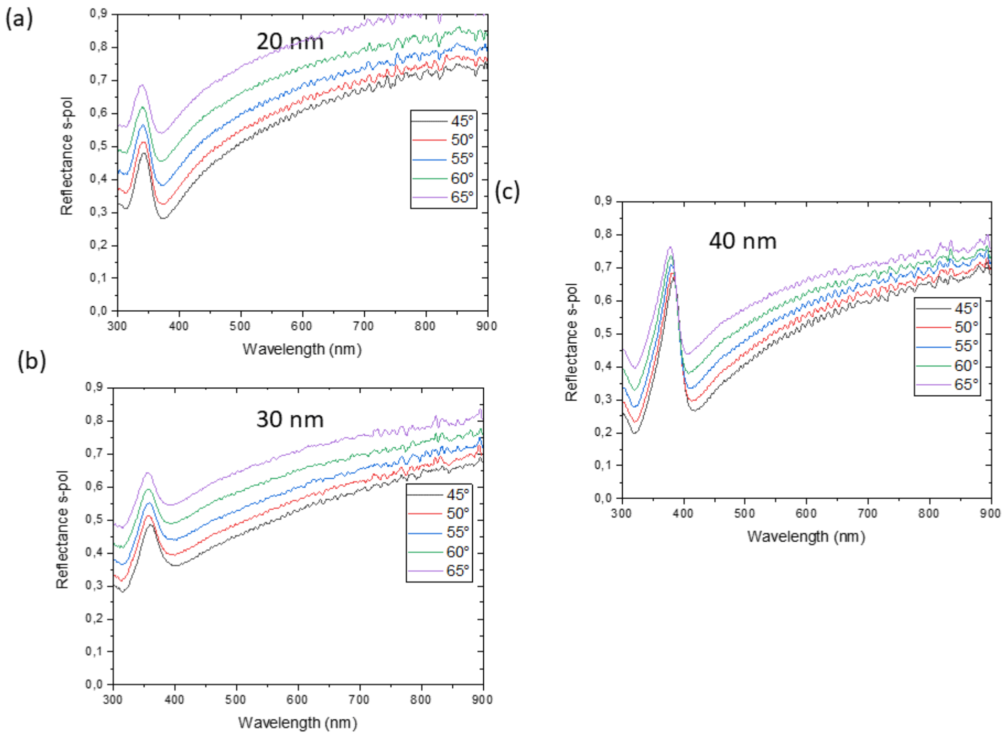

Figure 2.8: **(a)** Reflectance s-pol map calculated by varying the thickness t_2 and the wavelength λ **(b)** Reflectance s-pol spectra obtained calculated by varying the thickness t and the wavelength λ.

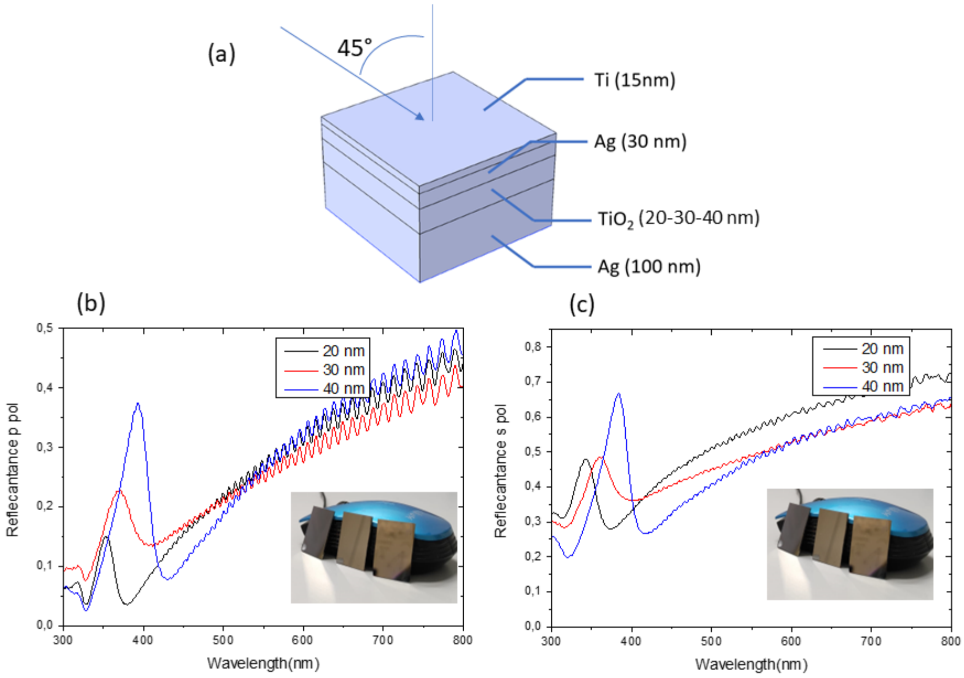

Figure 2.9: **(a)** Reflectance s-pol map calculated by varying the thickness t_2 and the wavelength λ **(b)** Reflectance s-pol spectra obtained calculated by varying the thickness t and the wavelength λ.

The same samples were analyzed by spectrophotometer with an angle of incidence equal to 0°, to evaluate the transmittance. It is also seen from the Figure in the inset that only visible radiation close to blue is transmitted. The transmittance spectrum shows how a small portion of the spectrum is transmitted and is found at 350, 380, and 420 nm respectively. These results can be optimized to obtain beam splitters, in fact, the reflected radiation peaks fall exactly into the transmitted ones.

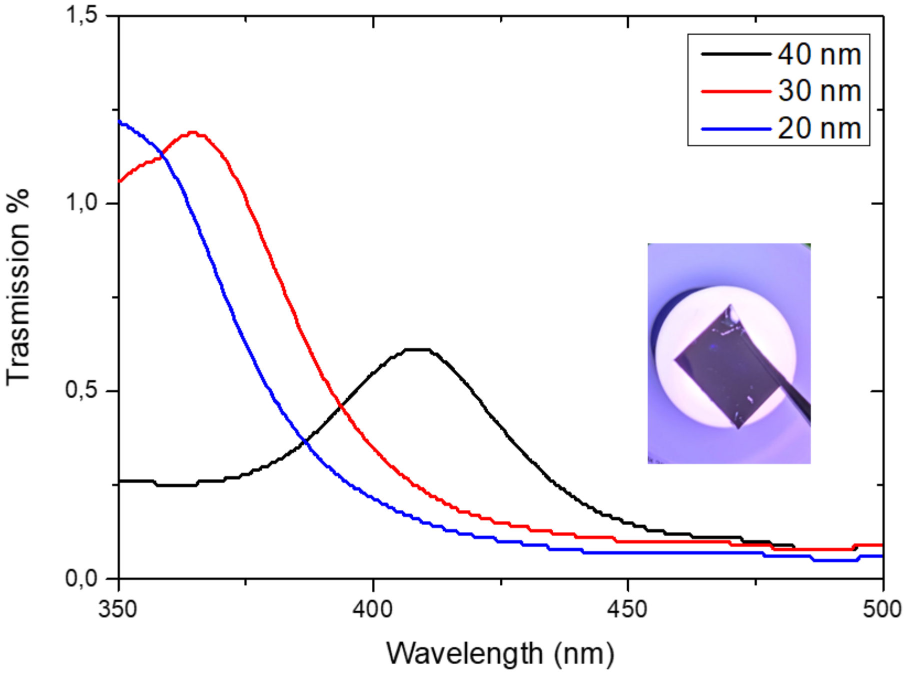

Figure 2.10: Transmittance spectra of FROCs thin films of samples Ag 100 nm, TiO_2 20, 30, 40 nm, Ag 30 nm, Ti 15 nm

2.6 Conclusion

The Fano formula, first discovered in the study of the Rydberg series for auto-ionization has been applied to various spectroscopic problems and for different objects. Because of the deep insight, it provides for spectroscopic data and its appearance in a wide range of nanophotonics studies, the Fano formula will continue to be an indispensable tool for optical design and analysis.

This chapter presents an optical coating that exhibits photonic Fano resonance (FROC). Currently, active research is being conducted on various manifestations of Fano resonance, and initial steps have been taken to apply this effect in physics, chemistry, biology, medicine, etc. Two main applications of FROCs have already been demonstrated: a beam splitter filter that reflects and transmits the same wavelength, and a platform for use as a refractive index sensor. Another potential application is as a spectral mirror for hybrid thermoelectric solar cells. Further studies will lead to new samples and uses. It has been shown that the use of Fano resonance is certainly better than the others used in the past, with improvements in performance and usage efficiencies.

The goal is to use the last titanium layer, which prevents oxidation of both air and especially aqueous solutions.

FROCs could be used for active photonic applications and reconfigurable nonreciprocity, studying the non-linear effects, and for steganography applications involving a phase change material.

Chapter 3

Tunability of metalenses permeated with Liquid Crystal

Metasurfaces have revolutionized the field of optics by providing remarkable control over the behavior of light. These engineered surfaces enable precise manipulation of optical phenomena, granting scientists and engineers unprecedented control over light propagation. Despite these advancements, one limitation of traditional metasurfaces is their fixed optical response, as they are typically designed for specific applications without the ability to modify their properties post-fabrication. This lack of adaptability poses a challenge when it comes to real-world applications that require versatility and dynamic optical control. In many practical scenarios, it is essential to have metasurfaces that can exhibit a modifiable optical response. This adaptability would allow for on-the-fly adjustments and versatile functionalities, greatly expanding the range of applications and enabling real-world implementation. Imagine metasurfaces that can be dynamically tuned to adapt to changing environmental conditions or user requirements. Such capabilities would unlock new opportunities in areas such as telecommunications, imaging, sensing, and data processing.

This chapter focuses on the analysis of a nanostructured planar fused silica metalens that incorporates a nematic liquid crystal (NLC) and gold nanoparticles. The addition of the NLC and gold nanoparticles introduces unique physical properties that can be manipulated through the application of external stimuli. This characteristic enables the development of reconfigurable optical metasurfaces, offering new possibilities for controlling light at the nanoscale. By permeating the fused silica metalens with the NLC, the refractive index of the material can be actively controlled. Nematic liquid crystals are known for their anisotropic properties, meaning their optical properties depend on the direction of light propagation. When subjected to external stimuli, such as electric fields or temperature changes, the orientation of the liquid crystal molecules can be manipulated, thereby altering the refractive index of the material. This allows for dynamic control over the optical response of the metasurface. Furthermore, the incorporation of gold nanoparticles into the NLC-infused metalens adds an additional dimension to its functionality. Gold nanoparticles exhibit plasmonic properties, meaning they can interact strongly with light at specific wavelengths. By carefully engineering the size, shape, and arrangement of the nanoparticles, researchers can tailor the metasurface's optical response and achieve functionalities such as enhanced light absorption, scattering, or polarization control. The combination of the NLC and gold nanoparticles in the fused silica metalens offers a versatile platform for reconfigurable optical metasurfaces. By applying external stimuli, such as electric fields, temperature variations, or even light itself, the properties of the embedded NLCs can be dynamically adjusted. This allows for real-time tuning of the metasurface's optical behavior, enabling functionalities such as beam steering, focusing, and wavelength selectivity. The analysis of this nanostructured planar fused silica metalens permeated with NLC and gold nanoparticles provides insights into the design principles and performance characteristics of reconfigurable optical metasurfaces. By understanding the interplay between the embedded NLC, gold nanoparticles, and external stimuli, researchers can unlock new possibilities for advanced optical devices with adaptable functionalities. These reconfigurable metasurfaces hold promise for applications in areas such as imaging, sensing, telecommunications, and optical signal processing, where dynamic control over light manipulation is essential. In summary, this chapter explores the integration of a nanostructured planar fused silica metalens with a nematic liquid crystal and gold nanoparticles. By leveraging the unique physical properties of the embedded NLCs and plasmonic nanoparticles, the metasurface becomes reconfigurable, allowing for active control over its optical response. This research opens up exciting opportunities for the development of dynamic and adaptable optical devices that can revolutionize various fields of science and technology.

In this chapter is reported all-optical, dynamic control of the metalens optical response resulting from thermo-plasmonic induced changes of the NLC associated with its nematic-isotropic phase transition. A continuous and reversible tuning of the metalens focal length was experimentally demonstrated, with a variation of 80 μm (0.16% of the 5 cm nominal focal length) along the optical axis. This is achieved without direct mechanical or electrical manipulation of the device. The reconfigurable properties were compared with numerical simulations of the focal length shift and exhibited close correspondence.

3.1 Introduction

In the past, the control of light propagation relied on refractive optical elements. However, a significant shift in this paradigm has emerged with the introduction of optical metasurfaces. These metasurfaces have revolutionized the field of optics by offering a new approach to develop flat optical components that can manipulate light at the nanoscale. [114–121]

These advances have led to the fabrication of ultra-thin metalenses with focusing properties matching or exceeding those of typical refractive lenses. [122–124] Metasurfaces have been implemented in a range of passive (non-tunable/ non-dynamic) applications, such as focusing and imaging, [125] beam conversion, [126] and holography [127]. However, these devices are typically created to support a fixed electromagnetic response which is determined at the time of fabrication. This limitation can be overcome by designing reconfigurable systems, or metasurface devices supporting a dynamically modifiable optical response. Post-fabrication tunability can unlock a range of potential applications, including varifocal imaging, beam steering, dynamic aberration correction and dynamic holography. [128] The dynamic response is typically controlled by an external stimulus; common control methods for creating reconfigurable systems involve thermal, electrical, chemical, or mechanical action. [129–132]

Nematic liquid crystals (NLCs) are well known materials in which the refractive index can be modified through the application of an external stimulus, such as an electric or magnetic field. [133] In a typical NLC cell, the liquid crystal is infiltrated between two glass slides that have been properly functionalized in order to obtain the desired molecular alignment. [134] NLCs are known to exhibit a tunable refractive index due to reorientation of the molecular alignment. This tunable refractive index can be utilized to achieve active reconfigurable control over optical metasurface devices. One recent technique to integrate NLCs and metasurfaces is to replace one of the two glass plates in a conventional liquid crystal cell with a metasurface device. The far-field optical properties of the metasurface, including diffractive lensing, can then be modified by electrically driving the liquid crystal orientation state, similar to the operation principle of a liquid crystal display. Additionally, NLC-encapsulated metasurface devices have been programmed as individually addressable pixels. With this technology, electrical modification of adjacent cells, resulting in a manipulation of the local phase, has been used to dynamically create arbitrary holographic patterns. [135] Beyond these approaches using a thick liquid crystal bulk, this chapter presents a metalens device that achieves dynamic and reversible reconfiguration by infiltrating NLC molecules into the space between the nanopillars composing the metasurface. In this scheme, the metasurface creates an initial phase profile for light focusing and the infiltrated NLC provides tunability. In previously published devices, the use of a thick liquid crystal superstrate poses certain challenges. One such challenge is the potential for a significant accumulation of transmitted phase within the bulk liquid crystal material, spanning multiple wavelengths. This accumulation of phase can make the device highly sensitive to non-uniformities present in the thick layer, which can adversely affect its performance. Moreover, the presence of thick liquid crystal layers introduces significant scattering effects. This scattering can undermine some of the advantages offered by metasurface devices, such as aberration-free focusing. The scattering phenomenon limits the device's ability to achieve precise and clear focusing of light. To address these challenges, a different approach is proposed. By removing the bulk liquid crystal cell, the metalens retains its two-dimensional configuration. This means that the phase and amplitude control necessary for manipulating light occur solely within the metasurface itself, rather than relying on the properties of the superstrate. This modification offers several benefits. Firstly, it reduces the sensitivity of the device to non-uniformities, as the thick liquid crystal layer is no longer present to introduce phase variations. Secondly, it mitigates the scattering effects associated with thick liquid crystal layers, preserving the metasurface's ability to achieve aberration-free focusing and maintain optical clarity. By confining the phase and amplitude control within the metasurface, this revised approach allows for greater precision and control over the optical properties of the device. It enables the development of more compact, efficient, and high-performance metasurface-based devices that can be tailored to specific applications. [136, 137] NLC molecules undergo evident variations in terms of optical properties by applying an external perturbation, like an electric/optical field or temperature gradients.

Spherical gold nanoparticles (AuNPs) are an ideal candidate for approaches requiring spatially-confined heating and thermally-triggered processes. [138–141] The AuNP diameter can be selected to tune the plasmonic band into the visible region, maximizing the absorption cross-section and resultant photothermal heating. [142] Plasmonic photothermal (PPT) heating is a direct consequence of localized surface plasmon resonances (LSPR), a distinct property of metallic nanoparticles. LSPR, or Localized Surface Plasmon Resonance, is a phenomenon that occurs when conductive nanoparticles interact with light at sizes smaller than the incident wavelength. This interaction gives rise to an electromagnetic resonance. [143, 144] When these nanoparticles are embedded in thermoresponsive materials, they can be used to trigger thermally induced phenomena. [145]

In particular, AuNPs can be used to induce thermoplasmonic effects in NLCs since the behavior of thermotropic NLCs is dependent on temperature: a phase transition can be induced by heating (from nematic to isotropic phase) or by cooling (from isotropic to nematic phase). During the nematic-isotropic (N-I) phase transition, the liquid crystal is converted from an ordered spatial distribution where the molecules align their long axis parallel to the substrate (planar or homogeneous alignment) to a disordered (isotropic) configuration without an alignment. [133] It should be noted that the pillar structure of the metalens can disrupt the planar alignment since the NLC molecules will interact with the interface at the pillar surface, leading to local deviations from the global alignment. This first-order phase transition modifies the physical properties of the liquid crystal, including the refractive index, density, and wetting properties. [146] For metasurface devices embedded with NLC, the phase transition can be harnessed to enable dynamic reconfigurability, greatly expanding the application space for these devices.

In this chapter, photothermally controlled varifocal metalens infiltrated with a mixture of 4-hexyl-4'-biphenylcarbonitrile (6CB) NLC and AuNPs is presented. Dynamic tunability of the focal distance is achieved through photothermal control of the NLC phase using free-space illumination, exploiting the photo-induced phase transition due to the excitation of an LSPR mode on the AuNPs. This all-optical method offers a suitable alternative for various applications requiring compact and tunable focusing devices, avoiding mechanical actuators or dedicated electrical connections. The system performance has been characterized in terms of the quality of the focus and focal length tunability range, and the reversibility and repeatability of the effect are demonstrated. The experimental results are further compared with corroborating numerical simulations of the focusing properties of the infiltrated metalens system.

3.2 An Overview of Liquid Crystals: Properties and Behavior

The classical aggregation states of matter are:

- The solid crystalline phase, is characterized by a three-dimensional positional order of the molecules and an orientational order of the molecules. The centers of gravity of the molecules are arranged on a crystalline lattice and their orientations are well-defined and fixed.
- The isotropic liquid phase characterized by a total positional and orientational disorder of the molecules. The centers of gravity of the molecules and their orientations are randomly arranged in the space.
- The isotropic gas phase is characterized by a total disorder of position and orientation and by intermolecular distances much larger than their molecular dimensions.

Toward the end of the 19th century, however, it became increasingly clear that there are many types of intermediate phases, called mesophases, whose properties lie between those of crystals and those of isotropic liquids. Normally, these phases are formed as the temperature rises. These mesophases are different depending on the geometrical characteristics of the molecules, and they can have either molecular crystals or liquid crystals.

In LCs, the molecules are strongly asymmetric (rod, disk, or banana - shaped molecules). In this case, the anisotropic interactions are very intense and favor an alignment of the molecules along a common direction called director. [147] In this case, if a sample, initially in the crystalline phase, is heated above a certain critical temperature, the transition to a new phase (liquid crystalline mesophase) is observed in which the three-dimensional positional order is completely or partially lost, while the molecules remain aligned along a common direction.

The first experimental evidence of liquid crystalline mesophases was obtained in 1880 by polarizing microscopic observations of the Austrian botanist

F. Reinitzer on a substance related to cholesterol, but not until the first half of the 20th century. [148] Liquid crystallinity is exhibited by several naturally occurring materials, including DNA, proteins, and cell membranes. [149, 150]

Depending on the nature of the phases they form, LCs can be divided into two general classes: thermotropic and lyotropic LCs. The behavior of thermotropic LCs is dependent on temperature: they usually exhibit mesophases either on heating materials from the crystalline solid state or on cooling from their isotropic liquid state. [151, 152] Lyotropic LCs, are formed by changing the concentration of amphiphilic molecules dispersed in an isotropic medium – for example, surfactant molecules dispersed in water. [153, 154] These systems are of interest primarily because of their association with some characteristic biological systems such as membranes but have not yet found important photonic applications were not yet found. On the contrary, as is well known, thermotropic liquid crystals, and especially nematic liquid crystals have found important applications both in the display industry and in the construction of photonic devices and detectors.

3.2.1 Thermotropic LCs

There are three basic types of LCs phases formed by thermotropic mesogens: smectic, nematic, and cholesteric. In all three types of phases, the LC molecules are aligned along a preferred direction called director n, which is the average orientation of the molecules within the phase. The extent to which the molecules are ordered within a phase is quantified by the order parameter S:

$$S = \frac{1}{2} < 3cos^2\theta > \tag{3.1}$$

where θ represents the angle between the director and the long axis of an individual molecule. The order parameter is temperature dependent and is in the range $-\frac{1}{2} < S < 1$.

The crystalline phase is characterized by a three-dimensional order of position and orientation. In other words, the molecules are arranged in a periodic three-dimensional lattice along three distinct directions marked by three characteristic vectors, a, b, and c. If the liquid crystalline material is initially in the solid crystalline phase and is heated above a critical temperature, it transitions to a new phase in which the orientation order is preserved while the position order is partially or completely lost.

The nematic phase has no residual positional order. The centers of gravity of the molecules are randomly arranged in space, while the molecular axes are aligned on average along a common direction characterized by a unit vector **n**, called the director. Due to the thermal agitation, the molecules are not exactly aligned along the director (Figure 3.1). The molecules distribution has a complete rotational symmetry around the director. The presence of a preferred direction makes the system macroscopically anisotropic and uniaxial, consequently, all macroscopic quantities (magnetic permeability, dielectric permeability, electrical conductivity, etc.) are anisotropic and described by uniaxial tensors. For example, the refractive index experienced by a wave polarized parallel to the director axis (extraordinary index) differs from the refractive index experienced by a wave polarized perpendicular to the director axis (ordinary index). An important property of nematic liquid crystals is that they are not ferroelectric. This means that although individual molecules may have a strong long dipole moment about the molecular axis, the dipole moment per unit volume is zero. In fact, in any macroscopic volume, for every molecule whose dipole is oriented in a particular direction, there is another with the opposite orientation.

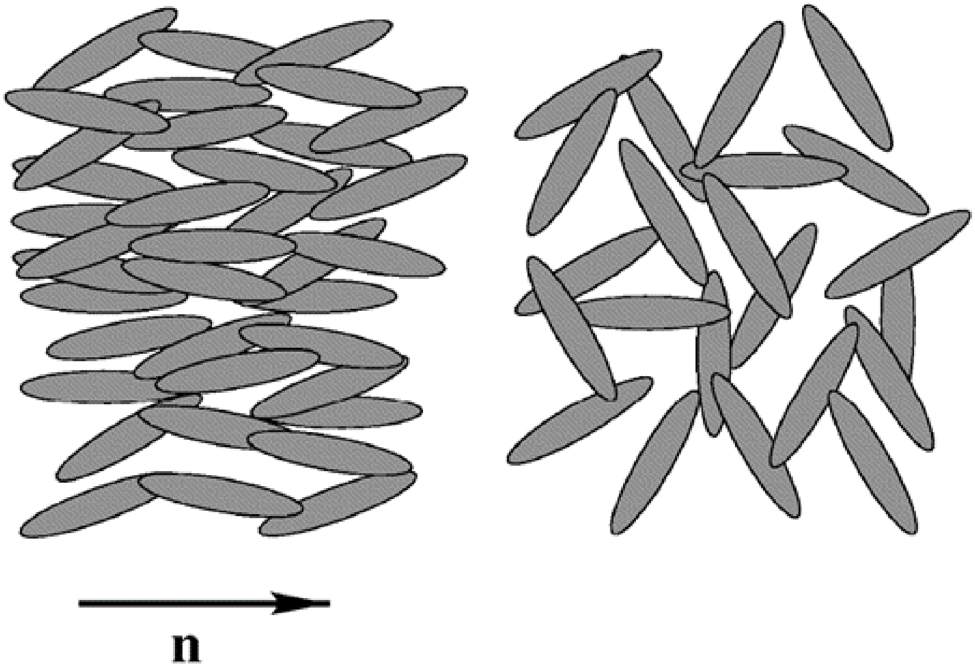

Figure 3.1: The nematic phase with a preferential orientational molecular order and the isotropic phase.

In the isotropic phase, the centers of gravity of the molecules are randomly distributed, and the orientations of the molecules are also completely random (Figure 3.1). It follows that all macroscopic properties, such as magnetic permeability, dielectric permeability, electrical conductivity, etc., are isotropic. Thus, such as system behaves like an ordinary isotropic fluid. A typical example of a calamitic molecule is the 4-hexyl-4'-biphenylcarbonitrile (6CB) molecule shown in Figure. The 6CB molecule was synthesized around the 1970s and is particularly important because it is chemically very stable and has a crystalline liquid (nematic phase) at room temperature. Due to the CN group, this molecule also has a large electric dipole moment aligned along its molecular axis. This property makes it particularly sensitive to electric fields as required for optoelectronic applications.

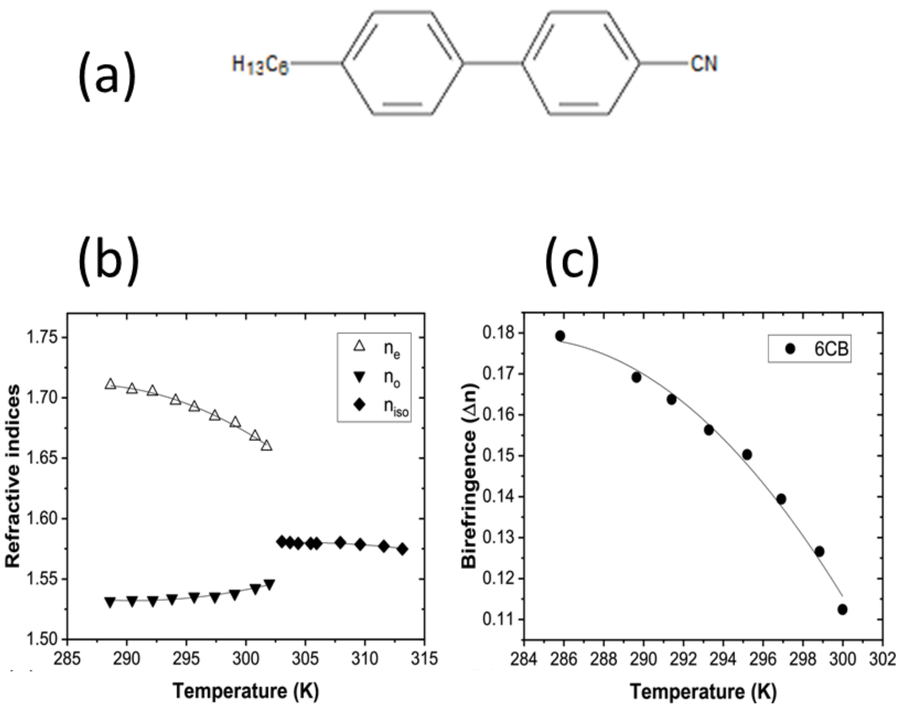

Figure 3.2: **(a)** Molecular structure of 4-hexyl-4'-biphenylcarbonitrile (6CB). **(b)** Temperature-dependent refractive indices of 6CB at λ=589 nm. **(c)** Temperature-dependent birefringence of 6CB at λ=589 nm.

[155]

The essential characteristics of the molecules leading to liquid crystalline mesophases are: 1) the presence of a rigid and anisotropic central core, generally consisting of benzene nuclei (e.g., the two benzene groups of the 6CB molecule in Figure 3.1. This rigid core minimizing the Gibb's free energy of the system. 2) The presence of partially flexible aliphatic tails (C_6H_{13} group in 6CB). These groups favor the fluidity of the system and unfavorably tend to affect the positional order and crystalline phase.

3.3 Thermoplasmonic effect with Nanoparticles

NLCs have attracted much attention both in scientific studies and in application among all soft and smart materials, due to their special properties: the possibility of changing their physical and optical properties by external stimuli, and here we focus on the effect of photothermal heating by nanoparticles (NPs). The synergism between LCs and gold nanoparticles (AuNPs) proves to be a new and interesting way to study and control temperature at the nanoscale. In fact, LCs have been used as active media to control the LSPR frequency of AuNPs and to detect photoinduced temperature variation at the nanoscale.

After the interaction with incident light in the visible spectral domain, the AuNPs gain energy by absorbing photons through electron transitions. If the frequency of the incident radiation matches the LSPR band, a resonant coupling with the EM wave occurs, with consequent excitation of the plasmon resonance, this triggering of phenomena manifests itself in a collective, coherent, and dipolar electronic oscillation in the conduction band.

The result is a global non-equilibrium condition of the electronic distribution, with some electrons absorbing photonic energy and others remaining unexcited. In order to restore the internal thermal equilibrium of the electron conduction band, the energy is redistributed, through electron-electron collisions (e-e), inside the quasi-free electronic gas. This process, which does not involve loss of energy acquired by photons, occurs on a time scale of approximately $10fs < \tau < 100fs$, based on the total energy introduced into the system. Subsequently, the energy of the hot carriers is redistributed with a relaxation process, through electron-phonon scattering (e-ph), on a time scale of $100fs < \tau < 100ps$. The last step takes into account the medium surrounding the nanoparticle, and the transfer of thermal energy to the interface, via phonon-phonon collisions (ph-ph), on the $10ps < \tau < 10ns$ time scale. The thermal dissipation leads to the cooling of the AuNP which releases heat to the surrounding medium, causing its temperature to rise. The dynamic of this process strongly depends on the heat transfer properties of the surrounding medium. The heat source term is calculated by evaluating the power density of the electromagnetic field absorbed in the NP and can be expressed:

$$Q = \sigma_{abs} I \tag{3.2}$$

where $I = nc\epsilon_0 E_0^2/2$, is the irradiance of the incident plane wave, c is the speed of light, and E_0 is the amplitude of the external electric field.

3.3.1 Photothermal characterization of the AuNPs.

To characterize the photothermal effects of the metallic colloidal solution, the solution is loaded into a 10 mm quartz cuvette and exposed to a resonant CW green laser (λ = 532 nm), impinging perpendicularly to it. In this way the heating phenomena related to the excitation of the LSPR has been stimulated. The thermal effect strongly depends on the resonant pump beam intensity I (power/surface); in fact, the energy absorbed (and delivered) by a single AuNP, which transforms in a dissipated heat Q from the nanoparticle, can be simply expressed as a function of the absorption cross section σ_{abs} and the impinging intensity. The thermographic analysis reveals the presence of hot spots, related to the photoinduced heat generated by the AuNPs. By monitoring the temperature values of the central pixel area of each hot spot, corresponding to the warmest point, it is possible to plot the temperature increase ΔT = T - T$_0$ versus the impinging intensity (T$_0$ is the temperature when the pump beam is off, which corresponds to room temperature). Experimental data of ΔT as a function of the impinging light intensity ranging from 1.0 to 10.0 W/cm^2 are reported in Figure 3.3. The maximum temperature increase obtained for the $I_{max} \sim 10$ W/cm^2 is $\sim$ 18°C.

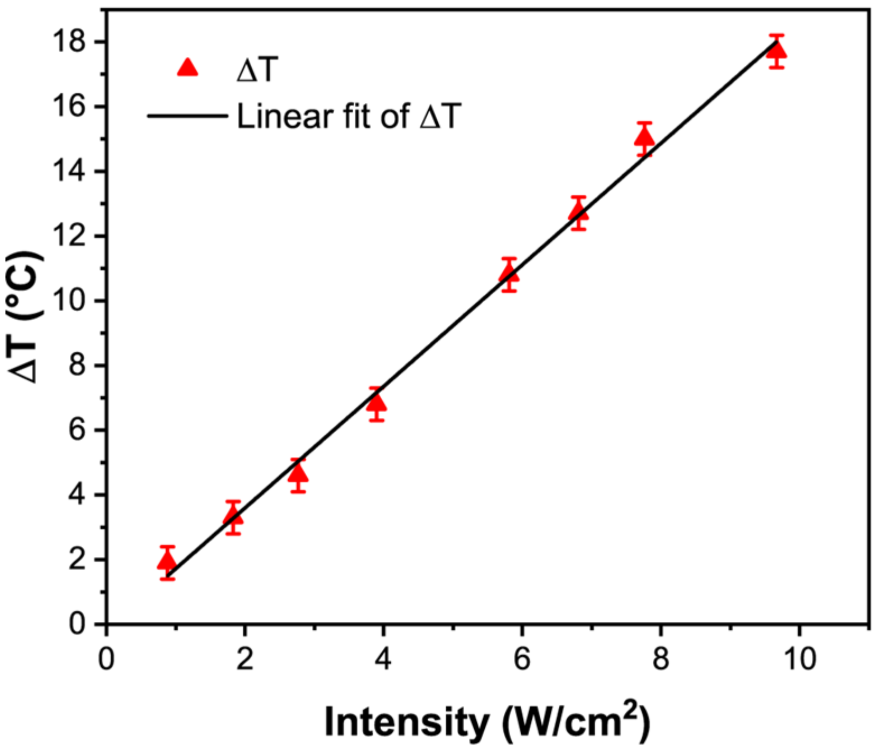

Figure 3.3: Temperature increase of AuNPs solution as a function of different intensity values of the resonant pump beam.

3.4 Liquid crystal infiltration into metasurface

The metalens considered is composed of an array of fused-silica nanopillars with diameters ranging from 250 nm to 600 nm and a height of 2 μm, arranged in concentric rings, with a fixed pillar edge-to-edge distance of 250 nm. A morphological characterization of the ”empty” metasurface (air among the nanopillars) is reported in Figure 3.4.

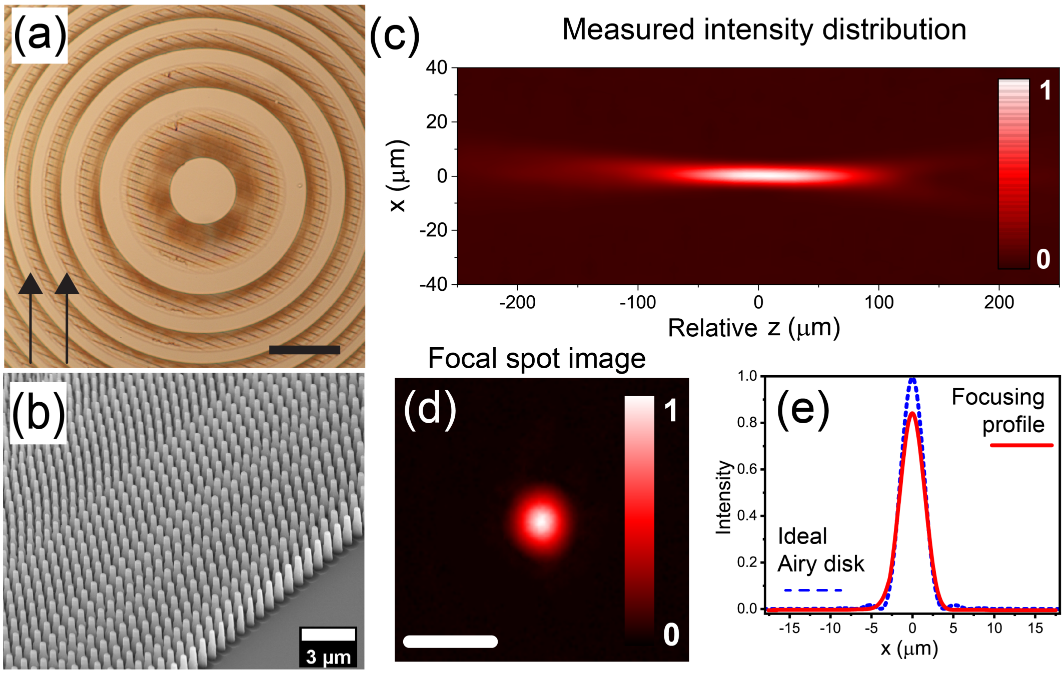

Figure 3.4: (**a**) POM (Polarized optical microscopy) image of the empty metasurface, scale bar: 200 μm; (**b**) SEM (Scanning Electron Microscopy) image of the pillar structure along the outside metalens; (**c**) normalized intensity distribution in the x-z plane about the focal point; (**d**) experimentally measured focal spot produced by the empty metalens in the focal plane, (scale bar: 10 μm) and (**e**) measured PSF (point spread function) of the empty metalens, dashed lines represent the focal spot profile for ideal Airy disk. The Strehl ratio value is 0.835. **Reproduced with permission [156].**

The wetting of the metasurface is generally non-trivial and depends strongly on the geometric properties of the patterned array and the hydrophilic attraction between the liquid and the substrate material, as well as on the viscous properties of the wetting liquid. [157] A droplet of a wetting liquid applied to a nanostructured array will generally remain in equilibrium, either in the Cassie-Baxter state, forming a droplet on the surface without wetting the structure, or in the Wenzel state, displacing air infiltration and filling the structure below the droplet. [158, 159] There is a third state in which the liquid exceeds the Wenzel equilibrium state and an infiltrating film spreads around the droplet and throughout the microstructure, resulting in complete infiltration of the nanopatterned array with the wetting material.

It was obtained a stable equilibrium film that completely infiltrates the metalens with the film height equal to the pillar height (2 m). This analysis assumes a regular array of flat-topped cylindrical pillars. In reality, the pillar spacing and size are highly non-uniform throughout the metalens. This non-uniform geometry can lead to complex infiltration behavior that is difficult to predict at the scale of the metalens.

Several droplets of the NLC/AuNPs mixture in the isotropic phase (heated to T > 30°C) were released around the outer edge of the metalens and left to infiltrate on a hot plate for 1 hour. During the infiltration, the NLC tends to move radially inward from the point of introduction at the outer edge of the lens after fully infiltrating the external pillared rings and remains spatially non-uniform even after the NLC front reaches the center of the lens. The equilibrium height profile of the infiltrated NLC depends strongly on the radially varying width of the circumferential rings without nanopillars (channels), due to the wicking forces and the downward force from the droplet at the outer edge of the lens.[160, 161]

The infiltration of the mixture inside the metalens can be followed through an optical microscope (Figure 3.5) analysis between crossed polarizers and the metalens is visibly brighter due to the polarization conversion performed by the birefringent NLC.

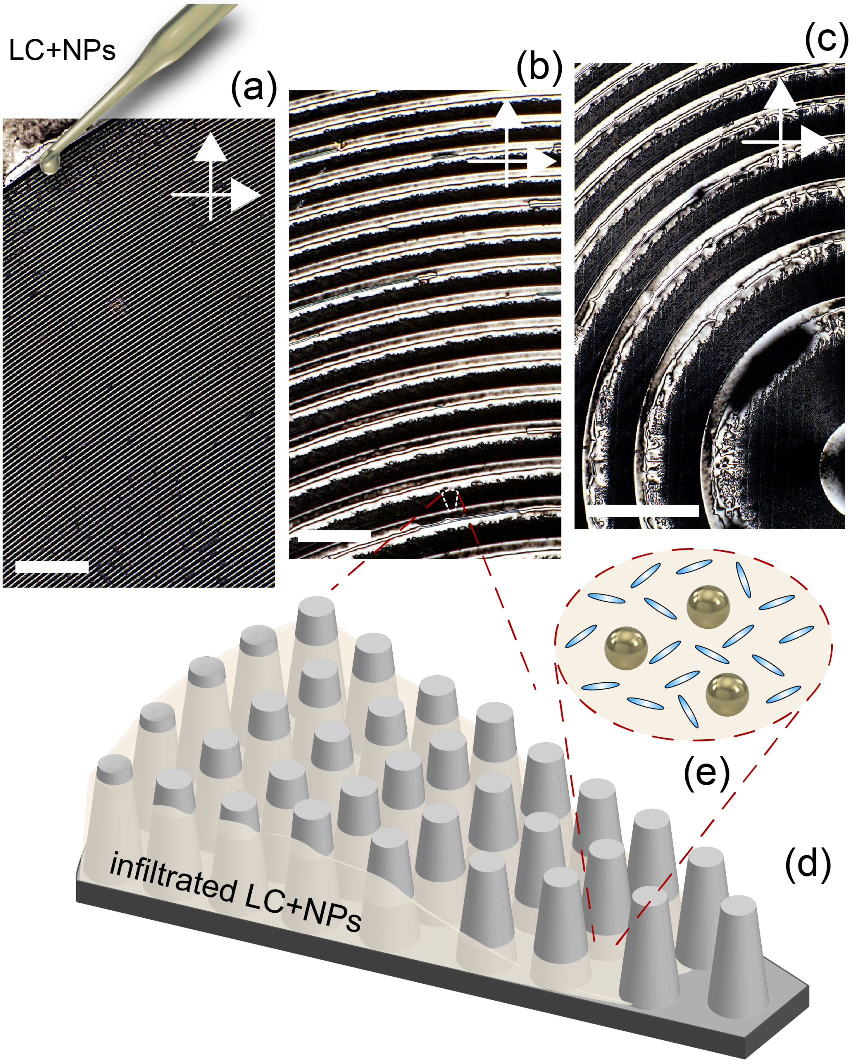

Figure 3.5: **(a) - (c)** POM images with cross polarizers of metalens filled with 6CB+AuNPs in different regions (scale bar: 200 μm). (**d**) Illustration of a pillars region of the metalens infiltrated with the 6CB+AuNPs mixture. **Reproduced with permission [156]**.

3.5 Tuning and imaging of metalens permeated LC

The optical setup to tune and control the filled metalens consists of a green continuous wave pump laser (λ = 532 nm, Verdi, Coherent), that resonates with the LSPR of AuNPs. The light is incident on the sample at a

45-degree angle and the resulting temperature variations are monitored with a thermal imaging camera, FLIR E40 (**Figure 3.6(a)**). The pump laser is enlarged with a beam expander (BE) to illuminate the entire metalens (diameter of 1 cm) so that the absorption for all planar NLC configurations, minimizes strain on the NLC alignment. [133, 162] A 570-nm high-pass filter is placed before the imaging CCD to remove the scattered pump beam from the focusing profile.

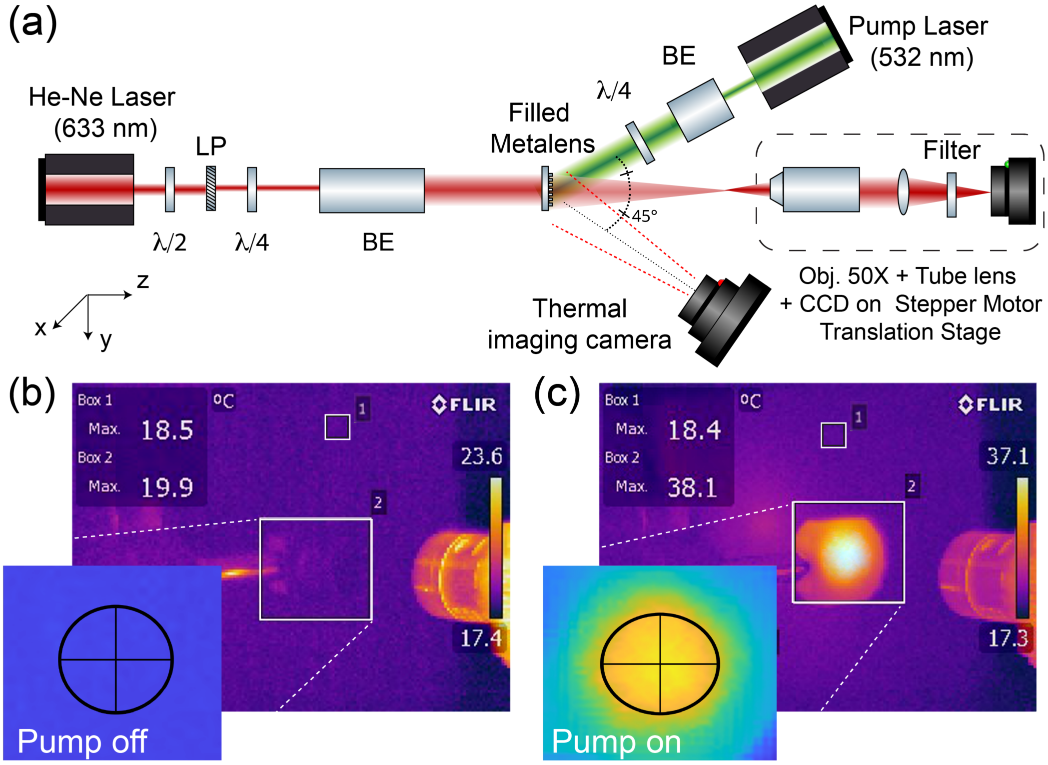

Figure 3.6: (**a**) Schematic diagram of the all-optical pump-probe and thermographic setup: Linear Polarizer (LP), $\lambda/2$ and $\lambda/4$ waveplates, Beam Expander (BE); thermographic images of the 6CB+ AuNPs filled metalens (**b**) when the pump laser beam is OFF and (**c**) when the pump laser beam is ON with intensity I= 2.3 W/cm^2. Inset: temperature maps of the metalens sample in each pump configuration. **Reproduced with permission [156]**.

Figure 3.6(b) shows a thermographic image of the 6CB+AuNPs filled metalens (with the mounting device) when the pump beam is stopped (state: pump off). The two white square areas labeled (1) and (2) in the figure, represent the two measurement areas centered on the room temperature (18.5 ± 1.0)°C and on the sample (19.9 ± 1.0)°C, respectively. The sample is then illuminated with the pump beam (state: pump on) and the intensity is varied and monitored until a maximum steady-state photo-induced temperature of 38.1 ± 1.0 °C is reached on the sample (box (2) in Figure 3.6(c)), that is higher than the nematic - isotropic transition temperature of $T_{NI} = 28.07$ °C.

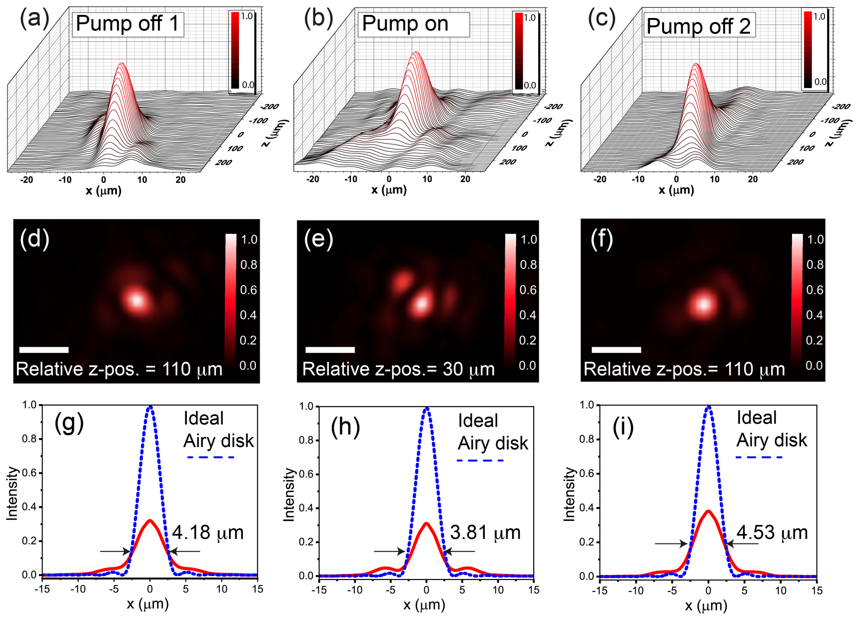

Figure 3.7: Normalized 3D plot of the measured intensity distributions of the metalens filled with 6CB+AuNPs when the pump state is (**a**) OFF, (**b**) ON (**c**) OFF 2 with (**d-f**) the corresponding intensity distributions at the focal plane for the three cases (scale bar: 10 μm), and (**g-i**) the corresponding PSFs, respectively. Experimental Strehl ratio values: (g) 0.324, (h) 0.315, and (i) 0.386. **Reproduced with permission [156]**.

Figure 3.7(a) shows the 3D reconstruction of the experimental intensity distribution of the metalens in the absence of pump beam (pump off 1), with the focal plane at the z-position of 110μm (Figure 3.7(d)). The z-position is given relative to the experimental zero point. The corresponding beam profile has a FWHM of 4.18 ± 0.01 μm (Figure 3.7(g)). The 3D beam reconstruction is performed by acquiring images in the x-z plane in the range from -250 μm to $+250$ μm along the optical axis, with a fixed step movement of 2 μm.

Comparing the infiltrated metalens with the empty one the infiltration is seen to decrease the Strehl ratio and so the quality of the focusing profile. This result is expected since the metalens has not been specifically designed to accommodate the infiltrated NLC.

A shift of 80 μm is observed in the focal distance (new z-position$= 30\mu$m) in the state of PUMP ON when turning on the pump beam, as well as a modification of the PSF (Figure 3.7(b)). Modifications in the sidelobe intensity can be observed in the focal plane 2-D intensity distribution (Figure 3.7(e)) while the FWHM of the central spot is decreased with respect to the pump off case. The FWHM of the focal spot is evaluated to be 3.81 ± 0.01 μm (Figure 3.7(h)). Then the pump beam is stopped from the sample in order to probe the reversibility of the tuning effect. A 3D reconstruction of the intensity distribution, as well as the corresponding PSF and the intensity sectional profile in the x-direction at the focal plane, are reported in Figures 3.7(c), 3.7(f) and 3.7(i), respectively. Following the heating cycle (pump off 2), the focal plane returns to the z-position of 110μm (Figure 3.7(c)), as obtained previously of the heating cycle in the state of pump off. The FWHM of the obtained PSF focal spot is 4.53 ± 0.01 μm (Figure 3.7(i)). The corresponding Strehl ratio values, for the three reported measurements, are SR$= 0.324 \pm 0.002$ for pump off 1, SR$= 0.315 \pm 0.002$ for pump on, and SR$= 0.386 \pm 0.002$ for pump off 2. The focal length tunability for the 6CB+AuNPs infiltrated metalens system is similarly demonstrated in Figure 3.8(a).

In order to check the reversibility of the tuning effect, a dynamic thermo-optical experiment was performed by monitoring the intensity in a fixed x-y plane (z-position = 30 μm) while modifying the sample temperature. The temperature was altered by controlling the exposure time to the pump beam. In the time interval 0 - 60 s a temperature of 40°C is reached, which is sufficient to induce the N-I transition Figure 3.8(b) - top panel). The intensity value is obtained by integrating over the intensity distribution in the x-y plane, and the measurement is then iterated for two on/off cycles. Only one cycle is shown in Figure 3.8(b) - bottom panel, for clarity. Increasing the temperature of the sample from T_1= 20 °C to T_7= 40 °C, the focal spot intensity is seen to increase roughly seven-fold from the initial intensity (Figure 3.8(b) - bottom panel). Once the pump beam is removed, the NLC cools back to room temperature, returning to the nematic phase (blue side region of the graph). At the same time, the light intensity values are observed to return to the initial state, demonstrating the repeatability of the observed effect. A control experiment (same experimental conditions) was performed on an NLC-filled metalens without AuNPs and no significant temperature or intensity variations were observed. This result demonstrates that the photo-heat conversion is directly associated with the plasmonic photo-thermal effect of the AuNPs.

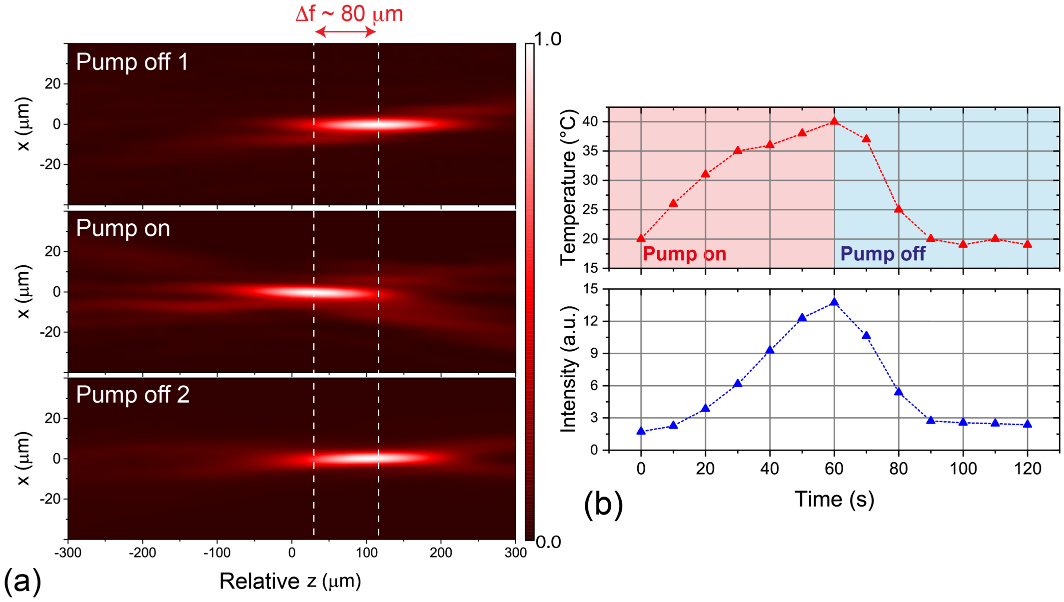

Figure 3.8: (a) Normalized measured intensity distributions along the propagation direction in the x-z plane for the 6CB+AuNPs filled metalens when the pump is off, pump on, and pump off 2. (b) Variations in the temperature and integrated focal spot intensity at the focal plane of the pump-active metalens (z-position = 30 μm), as the pump beam is turned on (Pump on) and then back off (Pump off) at 60 s. **Reproduced with permission [156]**.

The proposed tunable metalens system can be exploited for varifocal imaging with photothermally controlled focusing. To validate the imaging ability of the tunable metalens system, a negative 1951 USAF resolution target

(Thorlabs) was imaged with the metalens in place of an imaging objective, setup in the top panel of Figure 3.9. During the imaging measurement, the probe red laser (λ= 633 nm) continuously irradiated the target, while the green pump laser (λ = 532 nm - resonant with the plasmonic band of the spherical AuNPs) was switched on and off to trigger the photothermal effect and verify the focal plane shift. The images (corresponding to group 4 of the resolution target) formed by the metalens are shown in Figure 3.9. Initially, when the pump laser is off, the image is in maximal focus at z-position = 110 μm Figure 3.9(a)). When the thermo-optical control is switched on the image moves out of focus (Figure 3.9(b)). The image is returned to focus once the pump laser is removed (Figure 3.9(c)). Similarly, with the acquisition plane at the z-position of 30 μm, the obtained image is out of focus when the pump beam is off (Figure 3.9(d)), an in focus when the pump beam is on (Figure 3.9(e)). The image is again removed from focus when the pump beam is turned back off (pump off 2) (Figure 3.9(f)). The observed distance between the two well-focused image planes confirms a shift of about 80 μm in the focal length induced by the photothermal effects.

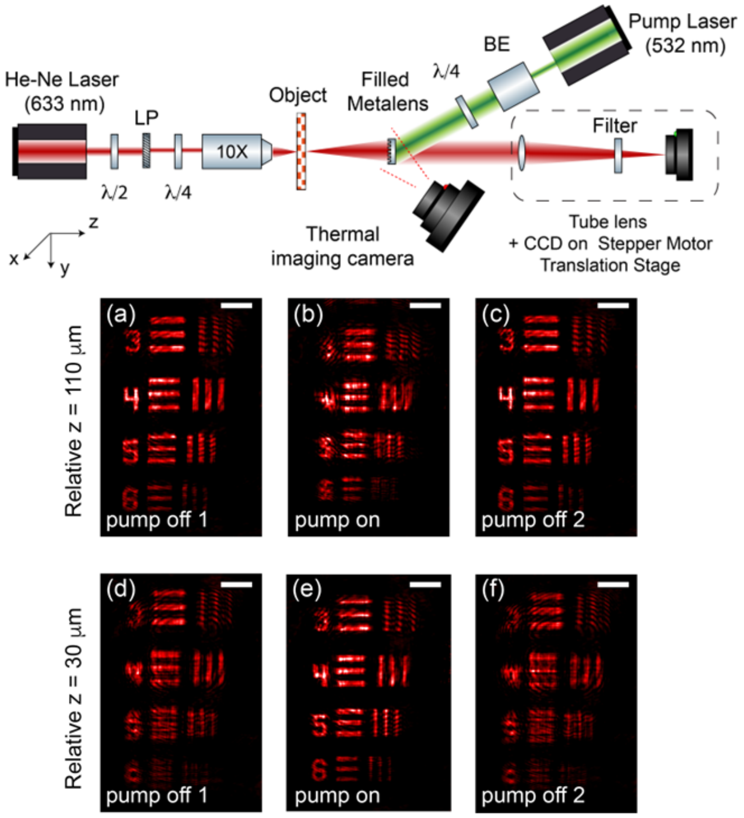

Figure 3.9: Schematic diagram of the imaging setup. A green laser (532 nm) is used to pump the metalens and the temperature was monitored by a thermal camera. **(a) - (f)** Tuning of the imaging distance of the metalens with negative target image (USAF 1951 target, group 4). **Readapted with permission** [**156**].

3.6 Conclusion

This chapter presents a novel approach to achieve reversible and dynamic control of the focal length in a metalens through a light-induced thermo-plasmonic effect. Experimental results demonstrate an impressive 80 μm shift in focal length, making it suitable for imaging applications. Notably, this device stands out from existing systems as it offers a fully optically tunable metalens. The tunability is achieved by directly infiltrating a mixture of NLC (liquid crystal) and AuNPs (gold nanoparticles) into the metasurface structure, eliminating the requirement for assembling a bulky liquid crystal cell.

In addition, this metalens system is fully compatible with conventional CMOS fabrication techniques and is easily controlled compared to tunable devices based on mechanical stretching or other control methods. Future applications include adaptive vision, bio-imaging, display applications where varifocal or multi-plane imaging is desired. In the current system, the phase profile is offset from the designed target by the infiltrated NLC. To improve the focal point shift distance, pillar geometries can be designed which maximize the difference in transmitted phase due to the NLC phase transition.

By altering the arrangement of pillars in the nanostructure, it is possible to modify the hemiwicking properties exhibited by the structure. This adjustment offers an opportunity to design specific infiltration profiles tailored to the desired application. To optimize this process effectively, the application of optimization methods, including machine learning approaches, would prove valuable. Machine learning algorithms can analyze and learn from large datasets, enabling the identification of optimal pillar arrangements that result in desired hemiwicking properties. By leveraging machine learning techniques, researchers can expedite the optimization process and enhance the overall performance of the nanostructure for various applications.

Chapter 4

Tunable polymeric metalenses

Metalenses have recently emerged as a groundbreaking technology, surpassing the capabilities of traditional refractive lenses in terms of compactness and subwavelength resolution. However, despite their exceptional optical properties, the fabrication process for these nanostructured lenses is known to be costly and time-intensive. This chapter presents a significant advancement in the field by reporting on the fabrication and characterization of scalable, cost-effective, flexible, and tunable metalenses designed specifically for visible frequencies. These advancements aim to address the challenges associated with the fabrication of metalenses, making them more accessible and practical for a wide range of applications. The material of such metalens consists of a polymer matrix, easily fabricated via direct pattern replication from a master copy. In addition, thanks to liquid crystal (LC) inclusions, the lens shows tunable features. This chapter explores the all-optical reconfigurability of a dielectric metalens through the thermal-induced changes in the local refractive index. The optical response of the metalenses undergoes a modification owing to the LC phase transition that can be induced thermally. We have obtained a continuous and reversible tunability of the metalens focal length with a variation up to 150 μm with an optical efficiency of 82% and a numerical aperture of 0.085 at 633nm.

4.1 Introduction

Efforts have been made to produce thinner and more compact lenses with the same properties as traditional refractive lenses. [163–165] Metasurfaces have enabled the development of multifunctional, thin, and lightweight optical components for optical imaging systems, such as augmented reality (AR), virtual reality (VR), mixed reality (MR) devices, and even imaging systems for drone cameras and orbiting satellites. [166–168] In particular, for the AR / VR / MR industry, the development of lightweight lenses in the centimeter range, larger than the pupil of the human eye, is of paramount importance. A lens with a large aperture allows better imaging in low light conditions and a larger field of view. [169]

These advances have led numerous research groups to fabricate ultrathin metalenses that feature properties such as tunability and aberration correction. [170–173]

The geometry, shape, and size of metalenses with specific subwavelength metallic or dielectric arrays, have been developed for multifunctional wavefront manipulation. For this reason, it is challenging to reconfigure such systems by external stimuli such as heat, [174] electrical voltage, [175] or mechanical action [176–178].

A metalens can be tuned by continuously changing its refractive index. Nematic liquid crystals (NLCs) are a class of materials known for their ability to alter their refractive index in response to an external stimulus. Many researchers have tuned LC refractive indices by applying an electric field in devices that coupled a NLC cell and a metalens. [179–183]

To design metalenses, the desired phase profile should be engineered by using meta-atoms. To focus an incident plane wave at a lens focal point, the target phase Φ at a point $P(x, y)$ on a metalens should satisfy the phase retardation: [184]

$$\Phi(r) = -\frac{2\pi}{\lambda}\sqrt{r^2 + f^2}, \tag{4.1}$$

where $r = \sqrt{x^2 + y^2}$ is the radial distance from the center to each point, f is the focal length, and λ is the wavelength.

In the present chapter, the ability of dynamic and reversible reconfiguration is provided by the NLC in a polymer matrix and the application of a thermal stimulus without creating an electro-optic cell. We demonstrate that it is possible to create inverse metasurfaces capable of focusing visible light, at low cost and their repeatability guarantees mass production.

4.2 Soft litography

Electron beam lithography, commonly used in the production of metasurfaces, is not well-suited for large-scale manufacturing due to its time-consuming and expensive nature. In contrast, polymer materials offer cost-effectiveness and disposability, making them more desirable for high-volume production. As a result, soft lithography techniques have continued to advance as an alternative approach to fabricating metasurfaces. Soft lithography methods provide greater scalability and cost-efficiency, contributing to the widespread adoption of these techniques in the field. [185–187] The advantages of this technique are numerous such as lower costs compared to classic lithography, suitable for applications in biochemistry and electronics, lower sensitivity than lithography which in any case depends on the master metasurface which can be reused many times and used to obtain even large-scale devices. The advantage of this approach is related to the multiple use of the master metasurface and its scalability. It is important also to mention that the aspect ratio of the nanopillars is a key parameter to avoid structural collapse. The aspect ratio of the elements of the metasurface must be limited to the values 3-4. [188]

Polydimethylsiloxane (PDMS) is an excellent material to be used in soft lithography stamps, as first demonstrated by Xia et al.[189] They showed that PDMS is able to replicate sub-micrometer structures. Due to the ease of use, PDMS has become the material of fist choice in soft lithography applications such as micro-contact printing, micro-transfer printing, replica molding, and transfer molding. The properties of this polymer are ideal for soft lithography: the low Young's modulus enables conformal contact on substrates and the rubber can be formed at room temperature. Moreover, PDMS is chemically inert, non-toxic, biocompatible, has a low surface energy and high permeability for gasses and solvents. Finally, PDMS is transparent in the wavelength range from 300 nm to 3 μm.

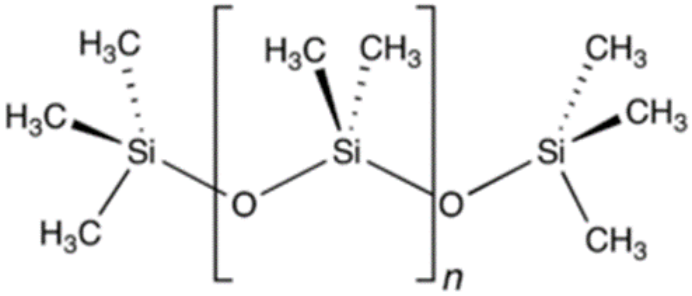

Figure 4.1: Chemical structure of Polydimethylsiloxane (PDMS).

Patterned PDMS stamps are formed by molding a reactive two-component PDMS system from a master pattern. This is usually a silicon wafer patterned by standard semiconductor lithography processes such as optical lithography, electron beam lithography in combination with etching or focused ion beam milling. PDMS stamps can also be directly molded from patterned resist materials.

4.3 Polymer Dispersed Liquid Crystal

Polymer Dispersed Liquid Crystals (PDLCs) are thin films of polymer that generally contains micro-sized droplets of nematic liquid crystal. [190] The LC director in the nematic droplet has no preferred orientation in the film in its undriven state. The result is the scattering of the incident light due to the mismatch between the refractive index of the polymer and the average refractive index of the LC. For this reason, it is important that the droplet diameter is of the same order of magnitude as the wavelength of the incident light. When an external stimulus is applied to the PDLC such as an electric field or heat, the NLC droplets can either reorient their directors parallel to the field, or lose their mesomorphism. [191] In the first case, if the ordinary refractive index of the LC (n_o) is matched to the refractive index of the polymer matrix, light incident normal to the film will be transmitted with no scattering as there is no refractive index mismatch. In the second case, if the average LC refractive index matches that of the polymer matrix, the heat will induce the nematic/isotropic phase transition with a consequent reduction of light scattering. For the large differences between the refractive indices of the two materials, PDLCs are opaque in their initial state and become transparent by applying an adequate external stimulus. An important application of these devices is their use as smart windows. [192, 193] When the stimulus is turned off, the PDLC films will gain the initial scattering state as the anchoring forces, acting on the NLC molecules at the polymer droplet walls, will move LC directors to their original random distribution of orientations.

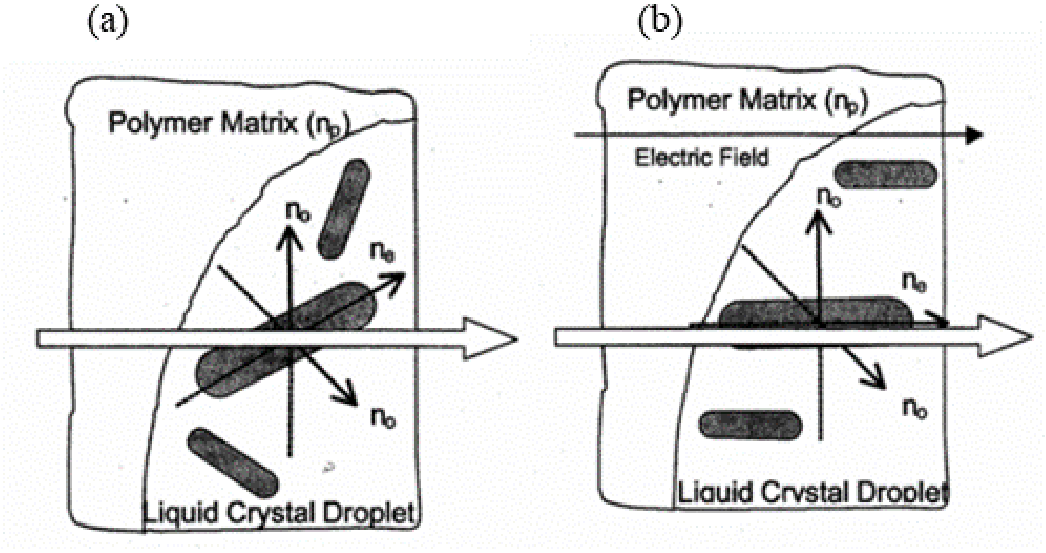

Figure 4.2: Schematic of PDLC material **(a)** in the undriven state **(b)** and in the driven state.

PDLC films can be prepared by different methods. The first one was demonstrated by Ferguson in 1981, who obtained a PDLC film (the so-called NCAP, Nematic Curvilinear Aligned Phase) by emulsification of a polymer and liquid crystal in water.[194] Other preparation methods were later described by Doane et al. The most important of these methods is certainly the polymerization of a homogeneous solution of liquid crystal and pre-polymer (Polymerisation Induced Phase Separation, PIPS). [195] As the polymer forms, the liquid crystal phase separates as discrete droplets. The polymerization process may be initiated by heat (as in an epoxy resin/curing agent mixture) or by UV light (as in an acrylate or thiol-ene system). In other similar methods of PDLC preparation, the phase separation process is controlled by temperature change (Thermal Induced Phase Separation, TIPS) or solvent evaporation (Solvent Induced Phase Separation, SIPS). It is possible to create metalens in PDLC that can focus the visible light spectrum and tune the focus.[196–200]

4.4 Fabrication and characterization

The metalens master is an all glass device as reported by Park et al. [169] Its surface was passivated by the deposition of a thin layer (10nm) of Chromium, using a Kenosistec KS300C sputtering system with a rate of 0.05 nm/sec. The inverse metasurface from the master was obtained by soft lithography, of a Polydimethylsiloxane polymer (PDMS), (Sylgar 184 Dow Corning), which is a transparent polymer widely used in microfluidics with excellent stretching, compliance, and biocompatibility properties.

The silicone and curing agent were mixed in the wt ratio 10:1 for a few minutes and then 2wt% of N-(4- Methoxybenzylidene) -4- butylaniline (MBBA) nematic liquid crystal was added. The MBBA concentration was limited to 2 wt% to avoid opaque lens effects being the PDMS refractive index ($n_{PDMS} = 1.41$) quite different from the MBBA average refractive index ($n_{MBBA} = 1.56$). After a vacuum degassing of about 10 minutes at a pressure of 10^{-2} mbar, the mixture was gently poured onto the metasurface, previously heated, and vacuum degassed again to prevent any air bubbles formation. The master metalens with the above mixture was then placed in the oven for 2 hours at 80°C.

Following the polymerization of PDMS, a gentle peel-off process was employed to obtain the replica metasurface. Figure 4.3 (a) shows the starting master metalens and the obtained replica metalens, Figure 4.3 (b). Both samples exhibit remarkably similar shapes and dimensions, providing strong confirmation of the reliability and fidelity of the manufacturing procedure. This is further illustrated in Figure 4.3, where the close resemblance between the two samples can be observed.

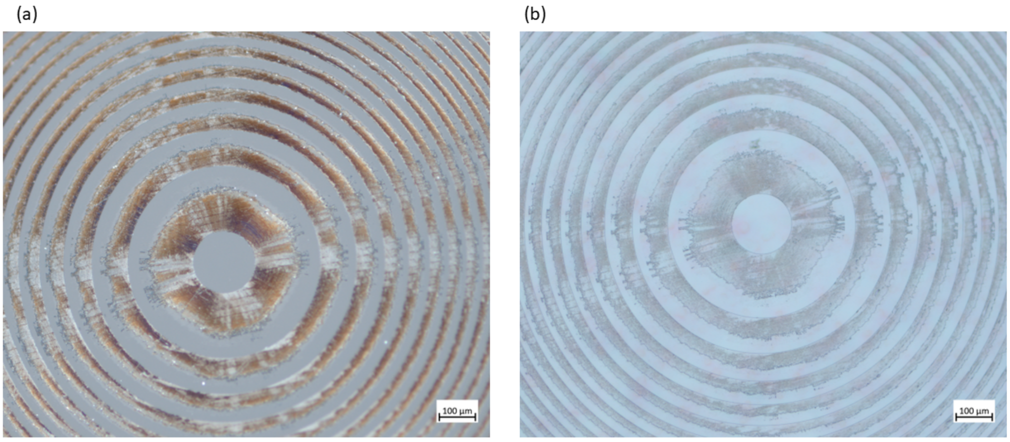

Figure 4.3: **(a)** Polarized optical microscopy image of metalens master between parallel polarizers after a deposition of 10 nm of Cr to passivate the surface and **(b)** metalens replica. Images were taken with a 10x objective, Axioscope 7 Microscopy (Zeiss) at room temperature. The scale bar is 100 μm.

The obtained metasurfaces are flat and flexible platforms, with a thickness of about 50 μm, and can focus the electromagnetic spectrum in the visible range. The flexibility of the material allows the metalenses to be able to be deformed as desired and therefore to be adapted to any type of geometry.

Figure 4.4 shows the fabricated metalens with a diameter of 1 cm and a focal length of 6 cm. During the initial test, the white light emitted by a smartphone was focused, and subsequent compression and elongation tests were conducted. Remarkably, the sample consistently returned to its original shape without any signs of breakage or damage.

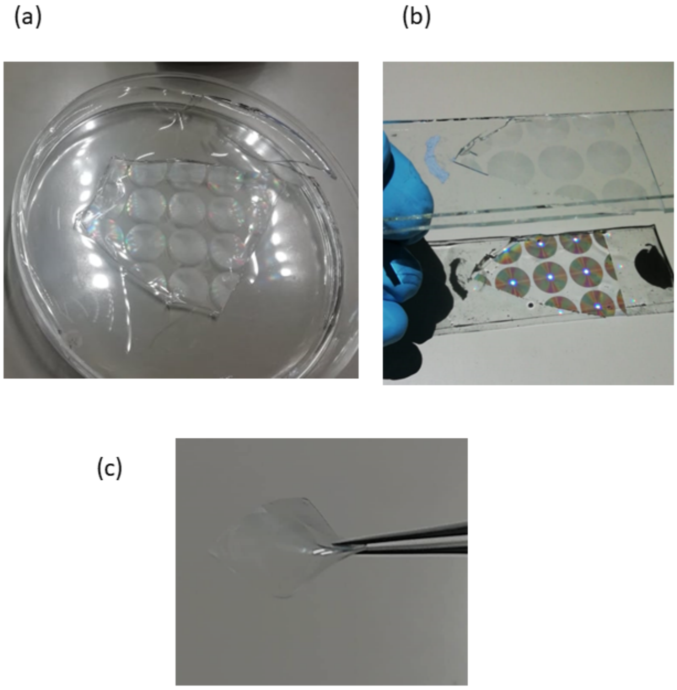

Figure 4.4: **(a)** Image of a series of manufactured replica metalens, the dimensions are identical to those of the master, 1cm diameter. **(b)** Demonstration of the property of manufactured lenses to focus the LED light of a smartphone and **(c)** demonstration of the flexibility of the metalens.

The samples fabricated using the soft lithography technique were analyzed by Atomic Force Microscopy (AFM) to check the quality of the metasurfaces.

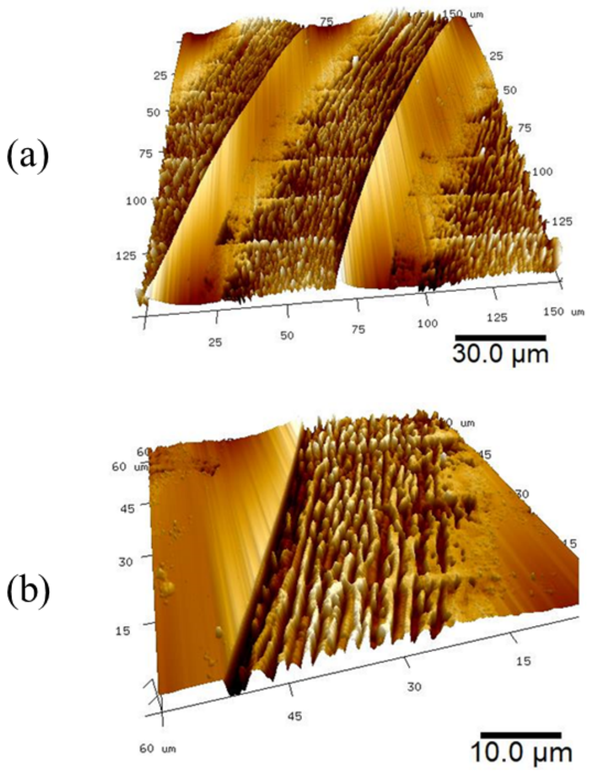

Figure 4.5: Images of metalens with Atomic Force Microscope (a) Three rings of metalens with a scale bar of 30 µm are shown. **(b)** A detail of a ring showing the periodicity of the pillars of the metalens. Scale bars 10 um.

In Figure 4.5 (a) a portion of the metalens is shown, specifically only three rings. It is noticeable that the pillars are not collapsed, but they have been well reproduced with a height of a few less than the master metasurface. In Figure 4.5 (b) a zoom was made on a portion of the metalens where the formation of the pillars and their periodicity of the same height are more evident.

The numerical aperture is evaluated using the following equation: [201]

$$NA = nsin\theta \tag{4.2}$$

In the condition of a low lens magnification, the equation is reduced to:

$$NA = nsin\left[arctan\left(\frac{D}{2f}\right)\right] \approx n\frac{D}{2f} \tag{4.3}$$

Where D is the diameter of the lens, n is the refractive index of the medium where the metalenses work namely n $\sim$ 1.0, and f is the focal length. From the last equation, a numerical aperture of the manufactured metalens of 0.085 was calculated.

Figure 4.6 shows the setups in the presence and absence of the metalens. The obtained power values were 470 mW and 570 mW respectively, keeping the laser power fixed.

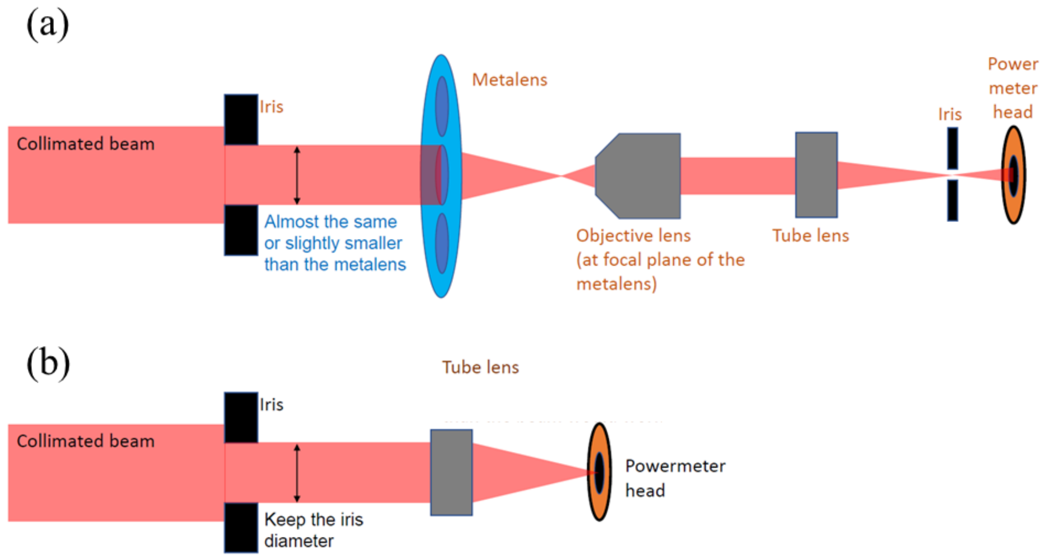

Figure 4.6: **T**wo experimental setups to calculate the efficiency of metalens: (a) in presence of the metalens to calculate the transmitted laser power, **(b)** without metalens to calculate all the transmitted laser power.

By comparing the two experimental values obtained, the efficiency of the metalens can be determined. This efficiency represents the amount of radiation that is transmitted through the metalens at a wavelength of 633 nm. Notably, the experimental value for the efficiency of the metalens is found to be 82%.

To confirm the quality of the replica metalens various characterizations were performed: focusing efficiency, Point Spread Functions (PSFs), and Strehl ratio (SR) measurements.

In Figure 4.7 PSFs and intensity profiles are obtained experimentally at different wavelengths (405 nm, 532 nm, 633 nm) at room temperature, to verify the properties of the metalens in the visible spectrum. The relative Full Width at Half Maximum (FWHM) values were 4.57, 7.49, 9.38 μm and SR values were 0.40, 0.30, 0.14 respectively.

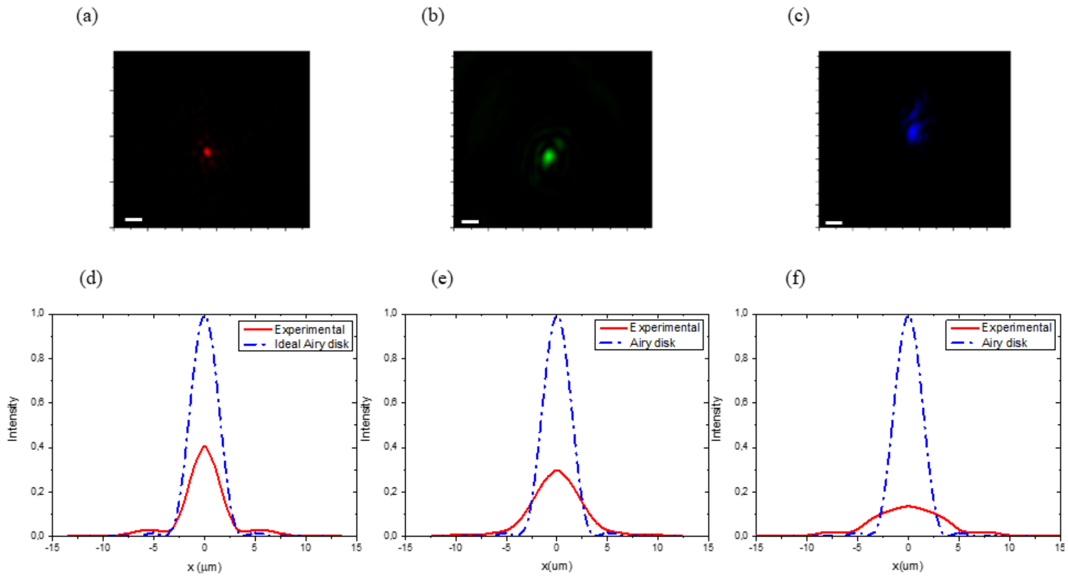

Figure 4.7: **(a) - (c)** Focal spot images of the metalens at room temperature with incident wavelengths at 405, 532, and 633 nm, respectively. The scale bar is 10 μm. **(d) - (f)** Comparison of the ideal intensity profile of the Airy disk (dashed line) and the experimental focusing profile of metalens replica (solid line) for each incident wavelength. The Strehl ratios (SRs) are 0.40, 0.30, and 0.13 and the measured focal lengths (f) for each wavelength are 40, 44, 52 mm, respectively.

It can be seen from the SR and FWHM values that the efficiency of the metalens is better at wavelengths closer to red, because PDMS is characterized by a large absorption in the UV and near blue region of electromagnetic spectrum, in Figure 4.8 is reported the experimental absorbance spectrum of the metalens.

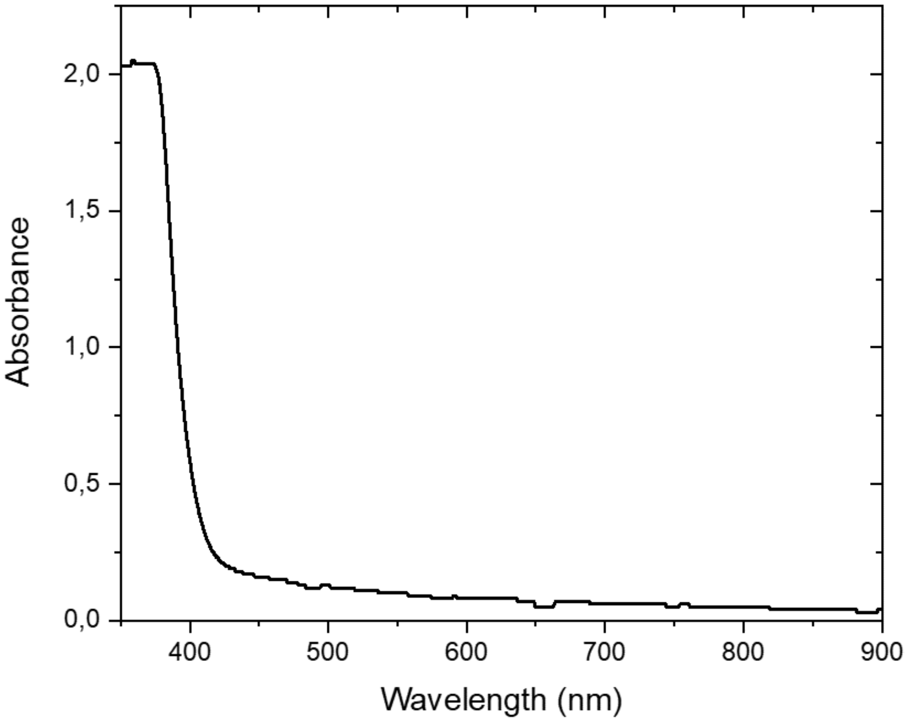

Figure 4.8: Absorbance spectrum of fabricated metalens in PDMS with 2wt % of MBBA.

4.5 Tuning and imaging of polymeric metalenses

The experimental setup to tune the replica metasurfaces (Figure 4.9) consists of a red laser (He-Ne, λ=633 nm) to illuminate the metalens; optical elements such as $\lambda/2$ and $\lambda/4$ waveplate and linear polarizer, a beam expander to widen the beam (beam diameter $\sim$ 1 cm). The transmitted light is collected by a 50X objective (N.A.= 0.5) and impinges through a tube lens on the CCD camera, (Pixelfly-Qe, a high-performance digital 12-bit CCD camera) that is mounted on a translation stage controlled by means of a step motor, to move and acquire intensity profiles. The metalens is placed on a heating stage to change and control its temperature.

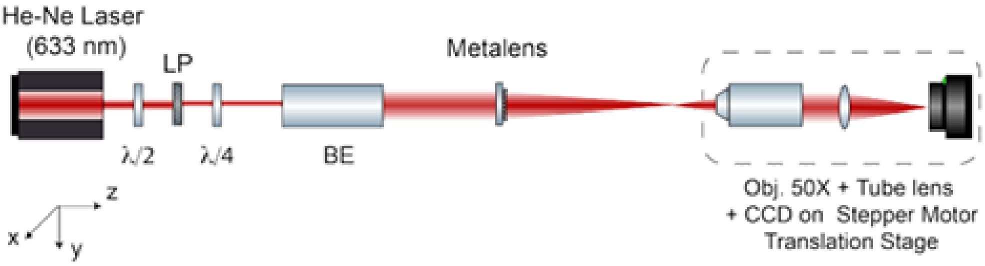

Figure 4.9: Schematic diagram of the optical setup: linear polarizer (LP), $\lambda/2$ and $\lambda/4$ waveplates, and beam expander (BE); metalens on a heating stage, a tube lens and a CCD with an objective 50x.

The nematic-isotropic transition temperature (T_{N-I}) of the MBBA liquid crystal occurs at 45°C. Consequently, the metalens was heated to T=55°C, to ensure the phase transition of the NLC. To check the repeatability and reversibility of the focus tuning, the reconstruction of the metalens Gaussian beam and the determination of the PSF and the SR values were performed at room temperature (T=21°C), after heating the sample to T=55°C, and after cooling the sample to T=21°C Figure 4.10.

First, the focus of the metalens was found at room temperature and was fixed as z = 0μm position for all experiments. A sweep of the focus position from $-400\mu m$ to +400 μm in 50 μm steps was done, moving the translator Then the sample was heated at 55°C, and the focus moved to the z = 150μm position after a few seconds. Subsequently, the sample was cooled, returning to room temperature after about 8 min, and the focus returned to the initial position (z = 0μm). The process was continuous and reversible, and checked by imaging for consecutive cycles.

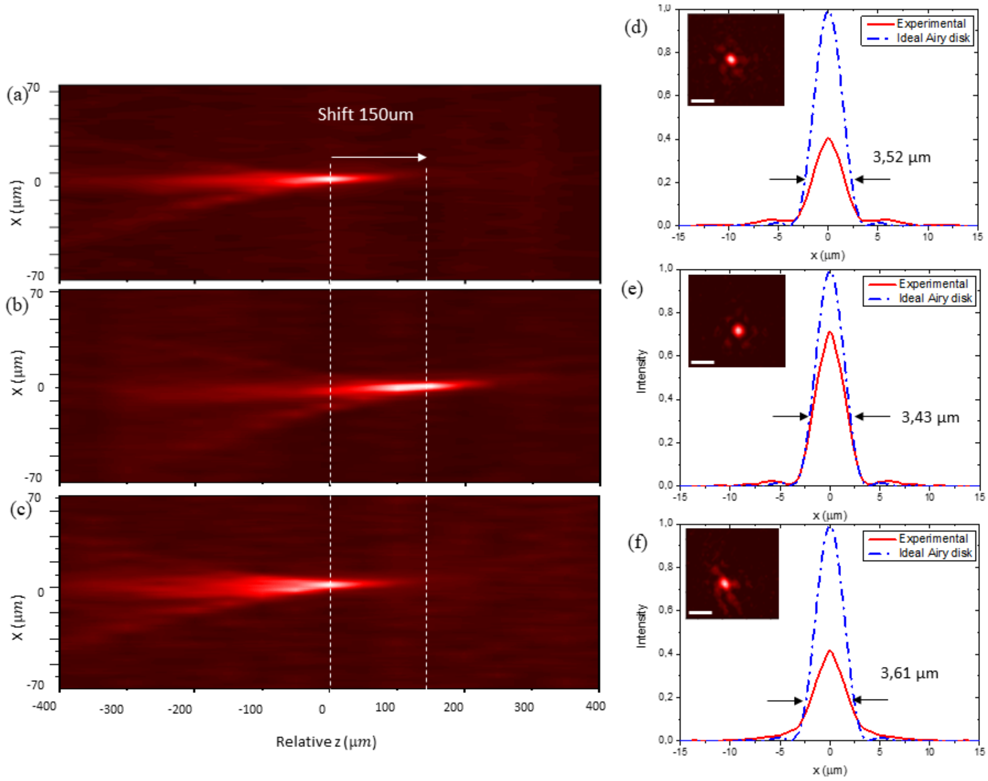

Figure 4.10: **(a)** Normalized measured intensity distributions along the x-z plane of the metalens at λ = 633 nm at room temperature T=21°C, **(b)** after increasing temperature at T=55°C and **(c)** after cooling the metalens and returning at room temperature T=21°C. Dashed line at z = 0 represents the focal plane for room temperature and the second dashed line represents the new focal plane at z=150 μm. **(d-f)** Corresponding PSFs, for the three temperatures respectively. The blue dashed lines represent the focal spot profile for ideal Airy disk along with the experimental focusing profile in red. Experimental Strehl ratio values: (d) 0.416, (e) 0.714, and (f) 0.403. In the inset the corresponding intensity distributions at the focal plane for the three cases (scale bar: 10 μm).

The SR values found for the three measurements were 0.416, 0.714, and 0.403 respectively. Being SR a parameter to assess the image quality, it is evident the obtained results that heating the metasurface can enhance the quality of images, in agreement with the PDLC scattering theory, which predicts a large reduction of the light scattering in the LC isotropic phase. Consequently, heat can tune the focus of the proposed metalens using the increase of temperature as the external stimulus.

To further assess the heat-induced enhancement of image quality, a USAF 1951 resolution test target, negative version, was placed in the middle of the metalens and a 10x objective within the previously described optical setup.

Figure 4.11(a) shows the images from the image at the room temperature T=21°C with the image focus set as the position z=0μm. Then, the metalens was heated a temperature well above the MBBA nematic-isotropic phase transition temperature (T=55°C) and moved out of focus in the position z=0 μm , Figure 4.11(b). Nevertheless, by changing the focus plane to the position z=150 μm, the focus of the image was got back, as shown in Figure 4.11(c). To validate the reversibility of the process, the metalens was cooled the initial temperature (T=21°C). Keeping the focus plane in the position z=150 μm the image was no longer in focus, Figure 4.11(d), but, moving it to the position z=0 μm, a well-focused image was again obtained as reported in Figure 4.11(e).

As a counter-test to verify the tunability of the metalens due to the thermal effect of the N-I transition of the NLC, imaging tests were performed with metalens without LC inclusion (MBBA 0 wt%).

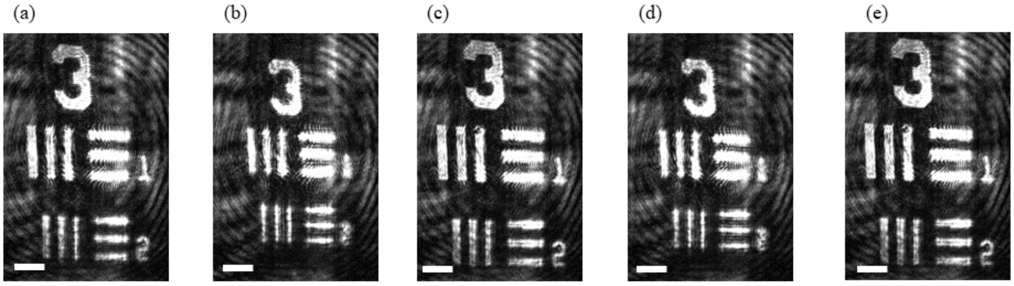

Figure 4.11: Imaging by metalens using a target (USAF 1951, group 3) when **(a)** the focus is at z=0 μm position at room temperature (T=21°C), **(b)** after heating the metalens well above the MBBA nematic-isotropic phase transition temperature without any change in the initial focus position (z=0μm), **(c)** after heating the metalens at T=55°C and shifting to the focus position of z=150 μm **(d)** after cooling the metalens T=21°C and keeping the previous focus position of z=150 μm, and **(e)** after cooling the metalens at T=21°C and moving the focus position back to z=0 μm. The scale bar is 500 μm.

Figure 4.12 shows clearly that the focus image of the target didn't move by changing the temperature in the position z=0 μm.

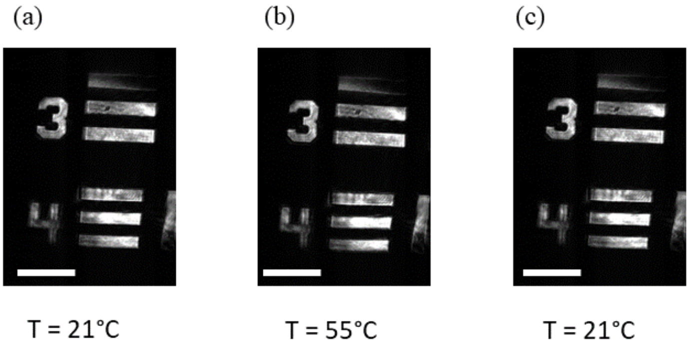

Figure 4.12: Imaging by a metalens without LC using a target (USAF 1951, group 2) when **(a)** the focus is at z=0 μm position at room temperature (T=21°C), **(b)** after heating at T=55°C the focused imaging remains in the initial position (z=0μm), **(c)** after cooling the metalens (T=21°C) there was not shift in the focused imaging, but still remains at z=0 μm. Scale bar is 500 μm.

To verify the effectiveness of the metalens, the experimental wavefront was calculated using the setup in Figure 4.13 (a). It includes a 635 nm laser diode as source, a Piezo Electric Deformable Mirror (DM), a beam splitter and Shack-Hartmann Sensor. The reconstructed wavefront is much thinner than the wavefront of the laser without metalens, a sign that the lens collimates the laser beam.

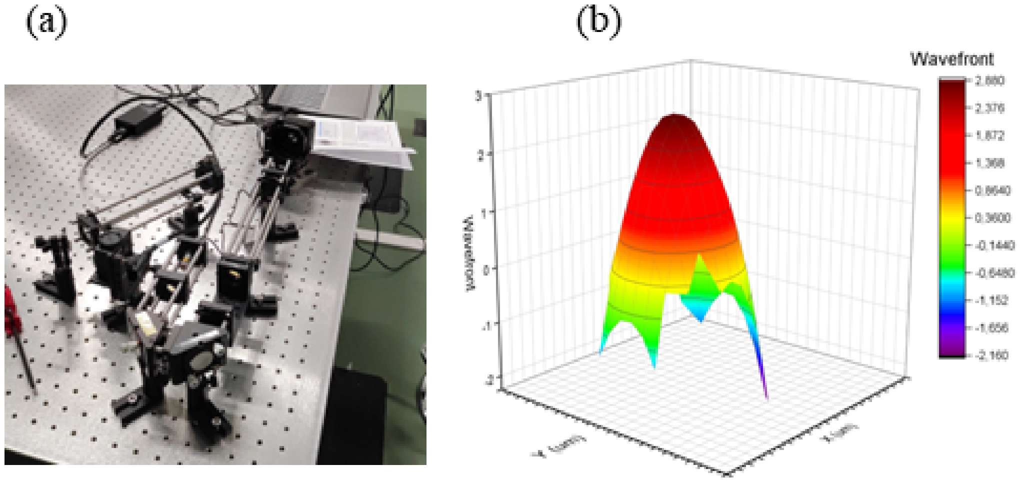

Figure 4.13: **(a)** Setup of Adaptive Optics Kit with CMOS Shack-Hartmann wavefront sensor (Thorlabs) **(b)** Experimental measurement of the wavefront of the fabricated metalens

4.6 Conclusion

In this chapter, I conducted research for my Ph.D. focused on the fabrication of tunable metalenses using a combination of polymer and nematic liquid crystal (NLC) materials. The fabrication process employed a fast and cost-effective method, resulting in flat, thin, flexible, and self-standing lenses. This soft lithography approach offers the advantage of directly fabricating the inverse of the master metalens, enabling large-scale production. To optimize the process, a large wafer containing multiple master metalenses can be utilized, allowing for the production of multiple lenses in a single manufacturing cycle. This scalable approach opens up possibilities for innovative and flexible device production. The metalenses were subjected to comprehensive optical and structural characterization. The inclusion of a thermally induced phase transition in the liquid crystal component enabled the reversible adjustment of the metalens focus. Impressively, a focal shift of 150 μm, which corresponds to 2.5% of the 6 cm nominal focal length, was achieved through this thermally induced phase transition. These findings highlight the tunable nature and practical applications of the fabricated metalenses, demonstrating their potential for diverse optical systems and devices.

Chapter 5

Conclusion and Perspectives

Metasurfaces represent a significant area of research and find applications across a wide range of fields due to their unique ability to manipulate electromagnetic waves at all optical frequencies. These artificial surface materials, typically composed of metallic patches or dielectric etchings in planar or multilayer configurations with sub-wavelength thickness, offer advantages such as lightweight construction, ease of fabrication, and control over wave propagation on the surface and in the surrounding free space.

This Ph.D. thesis focuses on the design, fabrication, and characterization of novel metasurfaces with the aim of greatly improving refractive index detection and optical tunable reconfiguration. The research was conducted under the supervision of Prof. G. Strangi at the University of Calabria, with substantial collaboration from the group at Case Western Reserve University and Prof. F. Capasso's group at Harvard University.

The first part of the thesis explores the fundamental aspects of metasurfaces for detecting various materials, particularly molecules, in sensing applications. Sensor technology has gained increasing importance in medical research and clinical diagnostics, enabling the direct detection of low molecular weight biomolecules associated with life-threatening diseases. While several technologies have been developed, becoming core label-free detection methods for cancer biomarkers and viruses, current biosensing techniques still require radical innovation to achieve high sensitivity, specificity, diffusion-limited transport, and accuracy in detecting both nucleic acids and proteins.

In the first chapter, a numerical investigation of a chiral plasmonic metasurface composed of an array of 3D right-handed gold helices is presented. By optimizing the parameters, it is possible to design a metasurface that exhibits distinct resonance modes within the infrared (IR) region of the electromagnetic spectrum. The calculated sensing sensitivity and figure of merit (FOM) values suggest that this tailored metasurface could be employed for surface sensing. Future studies may further enhance the sensitivity and FOM values by exploring alternative chiral geometries.

The second chapter provides a comprehensive study of Fano resonance and its application in optical coatings. A numerical study of a Fano-resonant optical coating (FROC) is presented, aimed at improving properties such as corrosion and oxidation resistance in air and water. Furthermore, several metasurfaces fabricated using physical vapor deposition (PVD) techniques are optically measured. These metasurfaces exhibit the potential for significantly enhancing the efficiency of silicon or perovskite photovoltaic cells and can also function as beam splitters.

The second part of the thesis focuses on the ability to control and manipulate electromagnetic radiation through metasurfaces using external stimuli. Optical metalenses have gained attention for their applications in solar energy harvesting, imaging, optoelectronic devices, and more. Conventional optical devices rely on geometric optics to focus light, such as convex lenses and concave mirrors. In the third chapter, the thermoplasmonic property of Au-Nps is utilized to induce a transition in liquid crystals in an infiltrated all-glass metalens. This groundbreaking result demonstrates the achievement of such a transition in an ultra-compact metasurface thickness through photonic stimuli. Future steps involve optimizing the metasurfaces, potentially leveraging artificial intelligence (AI) to better accommodate mixtures of liquid crystals.

The last chapter proposes a simple, low-cost, and rapid technique for fabricating replica metasurfaces that possess similar properties to the master metasurface. Structural and optical studies of the samples demonstrate their performance, including a focal shift of 150 μm, corresponding to 2.5% of the nominal 6 cm focal length. As a future prospect, the idea of fabricating a dedicated master metalens to obtain a tailored replica metasurface is presented. This approach would simplify the fabrication process, eliminating the need for time-consuming and expensive physical techniques.

In conclusion, this Ph.D. thesis has delved into the fascinating realm of metasurfaces, exploring their potential in manipulating electromagnetic waves across various optical frequencies. Through the design, fabrication, and characterization of novel metasurfaces, this research has contributed to the advancement of refractive index detection and optical tunable reconfiguration. The exploration of chiral plasmonic metasurfaces, Fano resonance, external stimuli control, and the fabrication of inverse metasurfaces has revealed promising avenues for enhancing biosensing, solar energy harvesting, imaging, and optoelectronic devices. While challenges and opportunities persist, the findings presented in this thesis underscore the importance of continued research and innovation in harnessing metasurfaces for transformative applications in the field of photonics.

Appendix A

Photo-thermal and stretching properties of polymer-based metasurfaces embedded with Au-NPs

Plasmonic PhotoThermal Therapy (PPTT) exploiting AuNPs, completely transformed material losses into a powerful nano-heating weapon. The possibility to exploit AuNPs as nano-sources of heat remotely triggered by light has, nowadays, impacted a wide range of research activities, including nanomedicine, cell biology, photothermal and hot-electron chemistry, solar light harvesting, soft matter, and nanofluidics.

In this section, we present a polymer-based meta-surface on which Au-Nps have been grown. This surface can be used both for laser irradiation at the same absorption wavelength as the molecules, generating heat, and as a control for shifting the absorption peak when the metasurface is stretched.

Table A.1 shows the values of laser power ($\lambda = 532nm$) used to excite the metasurface, as well as the power and intensity values on the sample.

$P_{laser}(mW)$	$P_{sample}(mW)$	I (W/cm^2)
10	6	$7.6 * 10^{-3}$
30	22.3	$2.8 * 10^{-2}$
50	39	$5.0 * 10^{-2}$
70	56.2	$7.2 * 10^{-2}$
90	73.3	$9.0 * 10^{-2}$
120	98.6	$1.3 * 10^{-1}$
150	124.5	$1.6 * 10^{-1}$
180	150.3	$1.9 * 10^{-1}$
210	175.6	$2.2 * 10^{-1}$
240	201.4	$2.6 * 10^{-1}$

Table A.1: Laser powers set, relative powers on the samples, and calculated laser intensity.

The results in Figure A.1 (a) were obtained with a spectrophotometer while the sample was continuously monitored with a thermal imaging camera (Figure A.1 (b)). It was possible to obtain a linear trend of the temperature difference as a function of the laser intensity on the sample, so that the system can be calibrated and used for disinfection of material or killing of bacteria.

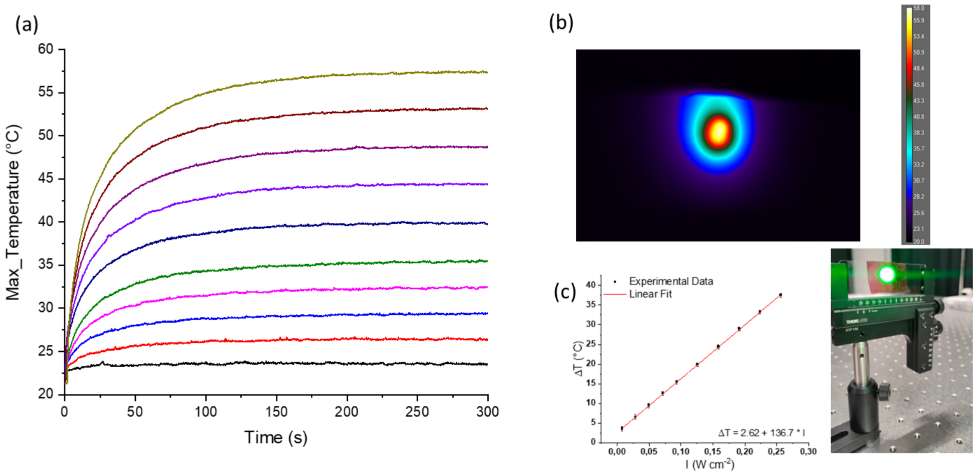

Figure A.1: **(a)** Time-temperature dependence under pump beam illumination with different laser intensity reported in table A.1. **(b)** Thermographic image captured with a thermal camera to monitor sample temperature. **(c)** Linear dependence of the temperature difference as a function of the laser intensity and, on the right, an image of the illuminated sample.

The proposed PDMS/AuNPs thin film can be used as a strain sensor if light absorption corresponding to the peak wavelength is calibrated to the level of applied strain. Three different PDMS metasurfaces containing Au-NPs with a radius size of 40 nm were simulated under the following conditions: compressed, at rest and stretched. After the creation of these three metasurfaces it was possible to obtain the absorbance spectra. In figure A.2 as in the case of compression, there is a blueshift and in the case of stretch there is a redshift of the plasmonic peak.

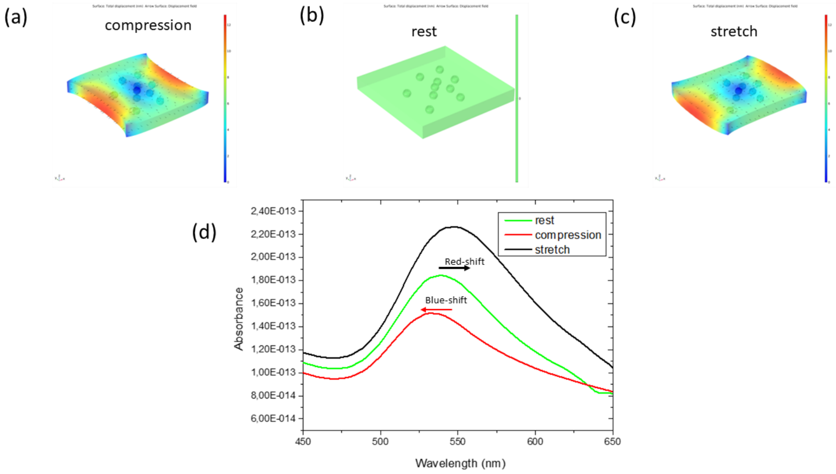

Figure A.2: **(a-c)** sketch of the simulated samples in the compression, rest and stretch conditions respectively. **(d)** Absorption spectra of the three previously described conditions. There is a blueshift in the compression and a redshift in the stretching of the sample.

The experimental results were conducted using a manual mechanism (in the inset of Figure A.3 (a)) to stretch the thin films and monitored with an Ocean Insight detector. Four measurements were performed to show the trend of the metasurfaces with relative percentages of stretch: one compression of -17%, one at rest of 0%, two stretches of 42% and 83% (Figure A.3 (a)-(c)). The obtained results are in agreement with the simulations previously presented.

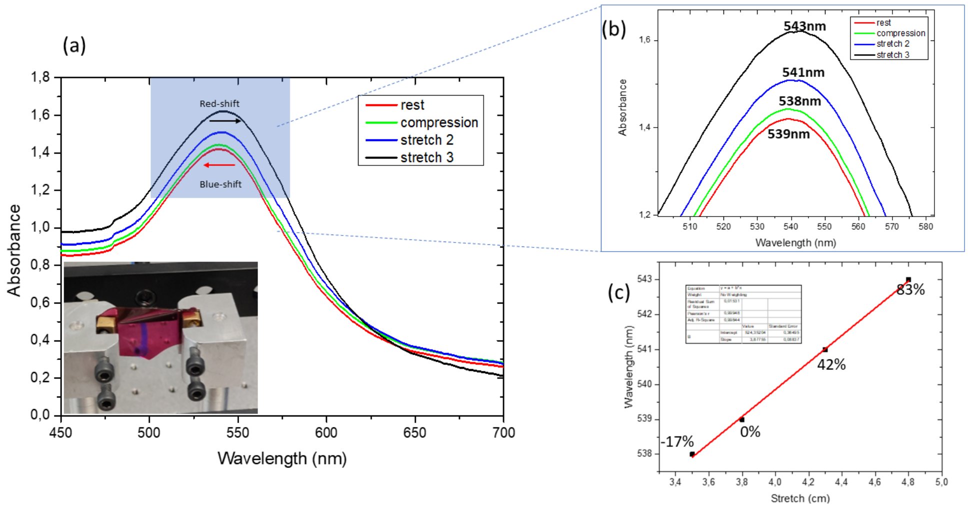

Figure A.3: **(a)** Experimental absorption spectra for the cases in which the sample (in the inset) is compressed, at rest and for two stretch conditions. **(b)** Zoom of the shift region of the spectral peaks confirming the previously simulated results. **(c)** Linear dependence of wavelength as a function of stretch percentage.

In conclusion these metasurfaces can find use as: (i) an effective thermal microbicidal effect; (ii) a photothermal lysis of cells; (iii) a development of biocide-free antibacterial surfaces and (iv) a unclonable flexible tags with hotspot fingerprint and others physical unclonable function (PUF).

Appendix B

Refractive index sensing using MIMI nanocavity

Hyperbolic metamaterials attract significant interest in the scientific community because they represent one of the most unusual classes of electromagnetic metamaterials. They represent a special system category that exhibits very particular behavior when impinged by an electromagnetic wave. They can be used to realize useful functions in emerging light-based meta-devices. Epsilon near zero (ϵNZ) metamaterials are characterized by the permittivity assuming near zero values at one or more wavelengths.

During my Ph.D., I was able to fabricate and analyze multilayered metasurfaces of Metal/Insulator/Metal/Insulator (MIMI). The aim is always to create sensors capable of detecting molecules with different refractive indices. I created some cells with MIMI samples at the base, around them some double-sided tape with a thickness of about 200 μm as shown in Figure B.1 (b) and (c). Through a graduated pipette it was possible to infiltrate 300 μl of different percentages of glycerol which are equivalent to the following refractive index values, reported in table B.1:

Percentage of glycerol	Refractive index
0%	1.3330
5%	1.3388
10%	1.3448
20%	1.3549

Table B.1: Percentage of glycerol and corresponding refractive indices.

As the percentage of glycerol increases and therefore the refractive index of the material, a shift of the second resonance mode in the transmittance spectrum can be seen in Figure B.1 (a), obtaining the following wavelength values:

Refractive index	Wavelength (nm)
1.3330	706.5
1.3388	705.5
1.3448	704.5
1.3549	700

Table B.2: Refractive index and corresponding wavelength values.

It is clear that there is a blue shift that causes a negative sensitivity value. From Figure B.1 (d), a linear fit of the wavelength values of the peaks as a function of the refractive indices was calculated. The value of the slope of the line represents the found sensitivity of the sensor, which is $S = -297nm/RIU$.

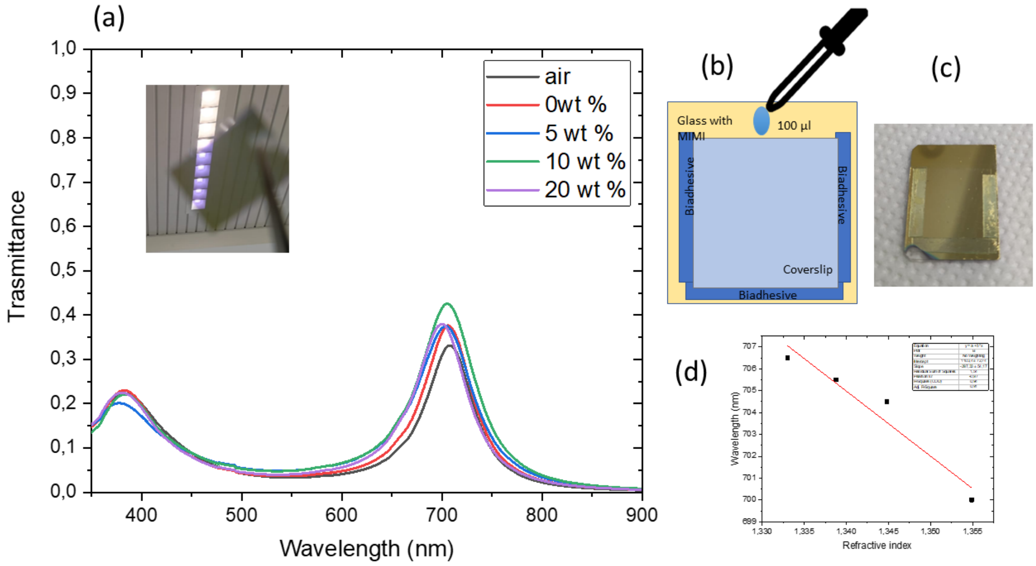

Figure B.1: **(a)** Trasmittance spectra of refractive index sensing with glycerol at difference % of glycerol. In the inset the transmittance view of the sample (Ag 30 nm – ITO 134 nm - Ag 30 nm – ITO 30 nm). **(b)** Sketch of the created cell for sensing application using bioadhesive and coverslip. **(c)** One of the cells created for sensing application. **(d)** Linear fit of different % of glycerol. Sensitivity of -297 nm/RIU.

List of Figures

List of Tables

Bibliography

[1] Xiaogang Lin, Nan Wan, Lingdong Weng, and Yong Zhou. Light scattering from normal and cervical cancer cells. *Applied optics*, 56(12): 3608–3614, 2017.

[2] Zhuo Wang, Gabriel Popescu, Krishnarao V Tangella, and Andre Balla. Tissue refractive index as marker of disease. *Journal of biomedical optics*, 16(11):116017, 2011.

[3] Andrew E Ekpenyong, Si Ming Man, Sarra Achouri, Clare E Bryant, Jochen Guck, and Kevin J Chalut. Bacterial infection of macrophages induces decrease in refractive index. *Journal of biophotonics*, 6(5):393–397, 2013.

[4] Yuan-Fong Chou Chau, Chan-Kuang Wang, Linfang Shen, Chee Ming Lim, Hai-Pang Chiang, Chung-Ting Chou Chao, Hung Ji Huang, Chun-Ting Lin, NTRN Kumara, and Nyuk Yoong Voo. Simultaneous realization of high sensing sensitivity and tunability in plasmonic nanostructures arrays. *Scientific reports*, 7(1):1–11, 2017.

[5] Barbora Špačková, Piotr Wrobel, Markéta Bocková, and Jiří Homola. Optical biosensors based on plasmonic nanostructures: a review. *Proceedings of the IEEE*, 104(12):2380–2408, 2016.

[6] Sayed Ali Khan, Noor Zamin Khan, Yinong Xie, Muhammad Tahir Abbas, Muhammad Rauf, Ikhtisham Mehmood, Marcin Runowski, Simeon Agathopoulos, and Jinfeng Zhu. Optical sensing by metamaterials and

metasurfaces: from physics to biomolecule detection. *Advanced Optical Materials*, 10(18):2200500, 2022.

[7] Ozlem Yavas, Srdjan S Acimovic, Jose Garcia-Guirado, Johann Berthelot, Paulina Dobosz, Vanesa Sanz, and Romain Quidant. Self-calibrating on-chip localized surface plasmon resonance sensing for quantitative and multiplexed detection of cancer markers in human serum. *ACS sensors*, 3(7):1376–1384, 2018.

[8] Erik Martinsson, Mohammad Mehdi Shahjamali, Karin Enander, Freddy Boey, Can Xue, Daniel Aili, and Bo Liedberg. Local refractive index sensing based on edge gold-coated silver nanoprisms. *The Journal of Physical Chemistry C*, 117(44):23148–23154, 2013.

[9] Ming Lun Tseng, Yasaman Jahani, Aleksandrs Leitis, and Hatice Altug. Dielectric metasurfaces enabling advanced optical biosensors. *ACS Photonics*, 8(1):47–60, 2020.

[10] Petr Bouchal, Petr Dvorak, Jiri Babocky, Zdenek Bouchal, Filip Ligmajer, Martin Hrton, Vlastimil Krapek, Alexander Faßbender, Stefan Linden, Radim Chmelík, et al. High-resolution quantitative phase imaging of plasmonic metasurfaces with sensitivity down to a single nanoantenna. *Nano letters*, 19(2):1242–1250, 2019.

[11] Jingxuan Cai, Cuiping Zhang, Chuwei Liang, Siyi Min, Xing Cheng, and Wen-Di Li. Solution-processed large-area gold nanocheckerboard metasurfaces on flexible plastics for plasmonic biomolecular sensing. *Advanced Optical Materials*, 7(19):1900516, 2019.

[12] Yang Shen, Jianhua Zhou, Tianran Liu, Yuting Tao, Ruibin Jiang, Mingxuan Liu, Guohui Xiao, Jinhao Zhu, Zhang-Kai Zhou, Xuehua Wang, et al. Plasmonic gold mushroom arrays with refractive index sensing figures of merit approaching the theoretical limit. *Nature communications*, 4(1):1–9, 2013.

[13] Ibrahim Misbah, Fusheng Zhao, and Wei-Chuan Shih. Symmetry breaking-induced plasmonic mode splitting in coupled gold–silver alloy nanodisk array for ultrasensitive rgb colorimetric biosensing. *ACS applied materials & interfaces*, 11(2):2273–2281, 2018.

[14] Jiao-Rong Fan, Jia Zhu, Wen-Gang Wu, and Yun Huang. Plasmonic metasurfaces based on nanopin-cavity resonator for quantitative colorimetric ricin sensing. *Small*, 13(1):1601710, 2017.

[15] Shobhit K Patel, Jaymit Surve, Vijay Katkar, Juveriya Parmar, Fahad Ahmed Al-Zahrani, Kawsar Ahmed, and Francis Minhthang Bui. Encoding and tuning of thz metasurface-based refractive index sensor with behavior prediction using xgboost regressor. *IEEE Access*, 10: 24797–24814, 2022.

[16] Yohan Lee, Sun-Je Kim, Hyeonsoo Park, and Byoungho Lee. Metamaterials and metasurfaces for sensor applications. *Sensors*, 17(8):1726, 2017.

[17] Na Liu, Thomas Weiss, Martin Mesch, Lutz Langguth, Ulrike Eigenthaler, Michael Hirscher, Carsten Sonnichsen, and Harald Giessen. Planar metamaterial analogue of electromagnetically induced transparency for plasmonic sensing. *Nano letters*, 10(4):1103–1107, 2010.

[18] Alexander B Khanikaev, Chihhui Wu, and Gennady Shvets. Fano-resonant metamaterials and their applications. *Nanophotonics*, 2(4): 247–264, 2013.

[19] Chihhui Wu, Alexander B Khanikaev, and Gennady Shvets. Broadband slow light metamaterial based on a double-continuum fano resonance. *Physical review letters*, 106(10):107403, 2011.

[20] Zhaoyi Li, Yibo Zhu, Yufeng Hao, Ming Gao, Ming Lu, Aaron Stein, Ah-Hyung Alissa Park, James C Hone, Qiao Lin, and Nanfang Yu. Hybrid metasurface-based mid-infrared biosensor for simultaneous quan-

tification and identification of monolayer protein. *Acs Photonics*, 6(2): 501–509, 2019.

[21] Giovanna Palermo, Massimo Rippa, Ylli Conti, Ambra Vestri, Riccardo Castagna, Giovanna Fusco, Elisabetta Suffredini, Jun Zhou, Joseph Zyss, Antonio De Luca, et al. Plasmonic metasurfaces based on pyramidal nanoholes for high-efficiency sers biosensing. *ACS applied materials & interfaces*, 13(36):43715–43725, 2021.

[22] Prasanta Mandal. Highly absorptive chiral l-shape mdm plasmonic metasurface as multifunction device: design and computational studies. *Plasmonics*, 16(4):1391–1403, 2021.

[23] Yu Qu, Lishun Huang, Li Wang, and Zhongyue Zhang. Giant circular dichroism induced by tunable resonance in twisted z-shaped nanostructure. *Optics Express*, 25(5):5480–5487, 2017.

[24] P Mandal. Au-al multi-metal bilayer dagger-like structure for broadband circular dichroism and tunability. *Optik*, 204:164222, 2020.

[25] Christopher Kelly, Ryan Tullius, Adrian J Lapthorn, Nikolaj Gadegaard, Graeme Cooke, Laurence D Barron, Affar S Karimullah, Vincent M Rotello, and Malcolm Kadodwala. Chiral plasmonic fields probe structural order of biointerfaces. *Journal of the American Chemical Society*, 140(27):8509–8517, 2018.

[26] Euan Hendry, T Carpy, J Johnston, M Popland, RV Mikhaylovskiy, AJ Lapthorn, SM Kelly, LD Barron, N Gadegaard, and MJNN Kadodwala. Ultrasensitive detection and characterization of biomolecules using superchiral fields. *Nature nanotechnology*, 5(11):783–787, 2010.

[27] Yao Liang, Han Lin, Kirill Koshelev, Fengchun Zhang, Yunyi Yang, Jiayang Wu, Yuri Kivshar, and Baohua Jia. Full-stokes polarization perfect absorption with diatomic metasurfaces. *Nano Letters*, 21(2):1090–1095, 2021.

[28] Chang-Yin Ji, Shanshan Chen, Yu Han, Xing Liu, Juan Liu, Jiafang Li, and Yugui Yao. Artificial propeller chirality and counterintuitive reversal of circular dichroism in twisted meta-molecules. *Nano Letters*, 21(16): 6828–6834, 2021.

[29] Giovanna Palermo, Giuseppe E Lio, Marco Esposito, Loredana Ricciardi, Mariachiara Manoccio, Vittorianna Tasco, Adriana Passaseo, Antonio De Luca, and Giuseppe Strangi. Biomolecular sensing at the interface between chiral metasurfaces and hyperbolic metamaterials. *ACS applied materials & interfaces*, 12(27):30181–30188, 2020.

[30] Alexander Y Zhu, Wei Ting Chen, Aun Zaidi, Yao-Wei Huang, Mohammadreza Khorasaninejad, Vyshakh Sanjeev, Cheng-Wei Qiu, and Federico Capasso. Giant intrinsic chiro-optical activity in planar dielectric nanostructures. *Light: Science & Applications*, 7(2):17158–17158, 2018.

[31] Justyna K Gansel, Michael Thiel, Michael S Rill, Manuel Decker, Klaus Bade, Volker Saile, Georg von Freymann, Stefan Linden, and Martin Wegener. Gold helix photonic metamaterial as broadband circular polarizer. *science*, 325(5947):1513–1515, 2009.

[32] Justyna K Gansel, Martin Wegener, Sven Burger, and Stefan Linden. Gold helix photonic metamaterials: a numerical parameter study. *Optics express*, 18(2):1059–1069, 2010.

[33] Yiqiao Tang and Adam E Cohen. Optical chirality and its interaction with matter. *Physical review letters*, 104(16):163901, 2010.

[34] SeokJae Yoo and Q-Han Park. Metamaterials and chiral sensing: a review of fundamentals and applications. *Nanophotonics*, 8(2):249–261, 2019.

[35] Yang Zhao, Amir N Askarpour, Liuyang Sun, Jinwei Shi, Xiaoqin Li, and Andrea Alù. Chirality detection of enantiomers using twisted optical metamaterials. *Nature communications*, 8(1):1–8, 2017.

[36] Mario Hentschel, Martin Schäferling, Xiaoyang Duan, Harald Giessen, and Na Liu. Chiral plasmonics. *Science advances*, 3(5):e1602735, 2017.

[37] Jose García-Guirado, Mikael Svedendahl, Joaquim Puigdollers, and Romain Quidant. Enantiomer-selective molecular sensing using racemic nanoplasmonic arrays. *Nano letters*, 18(10):6279–6285, 2018.

[38] John David Jackson. Classical electrodynamics, 1999.

[39] HG Jerrard. Modern description of polarized light: matrix methods. *Opt. Laser Technol.*, 14(6):309–319, 1982.

[40] R Clark Jones. A new calculus for the treatment of optical systems. vii. properties of the n-matrices. *Josa*, 38(8):671–685, 1948.

[41] RMA Azzam and NM Bashara. Simplified approach to the propagation of polarized light in anisotropic media—application to liquid crystals. *JOSA*, 62(11):1252–1257, 1972.

[42] Anthony Gerrard and James M Burch. *Introduction to matrix methods in optics*. Courier Corporation, 1994.

[43] Ismo Lindell, Ari Sihvola, Sergei Tretyakov, and Ari J Viitanen. *Electromagnetic waves in chiral and bi-isotropic media*. Artech House, 1994.

[44] Jin Au Kong. Theorems of bianisotropic media. *Proceedings of the IEEE*, 60(9):1036–1046, 1972.

[45] Mohammad Kamandi, Mohammad Albooyeh, Caner Guclu, Mehdi Veysi, Jinwei Zeng, Kumar Wickramasinghe, and Filippo Capolino. Enantiospecific detection of chiral nanosamples using photoinduced force. *Physical Review Applied*, 8(6):064010, 2017.

[46] Anatoly Serdyukov, Igor Semchenko, Sergei Tretyakov, and Ari Sihvola. Electromagnetics of bi-anisotropic materials: Theory and applications. 2001.

[47] Christophe Caloz, Andrea Alu, Sergei Tretyakov, Dimitrios Sounas, Karim Achouri, and Zoé-Lise Deck-Léger. Electromagnetic nonreciprocity. *Phys. Rev. Applied*, 10(4):047001, 2018.

[48] Tom G Mackay and Akhlesh Lakhtakia. *Electromagnetic anisotropy and bianisotropy: a field guide*. World Scientific, 2010.

[49] S Bassiri, N Engheta, and CH Papas. Dyadic green's function and dipole radiation in chiral media. *Alta Frequenza*, 55(2):83–88, 1986.

[50] Nader Engheta and Dwight L Jaggard. Electromagnetic chirality and its applications. *IEEE Trans. Antennas Propag.*, 30(5):6–12, 1988.

[51] Martin Schäferling. *Chiral Nanophotonics: Chiral Optical Properties of Plasmonic Systems*. Springer, 2018.

[52] William Moffitt. Optical rotatory dispersion of helical polymers. *J. Chem. Phys.*, 25(3):467–478, 1956.

[53] Yee-Hsiung Chen, Jen Tsi Yang, and Hugo M Martinez. Determination of the secondary structures of proteins by circular dichroism and optical rotatory dispersion. *Biochemistry*, 11(22):4120–4131, 1972.

[54] John D Roberts and Marjorie C Caserio. *Basic principles of organic chemistry*. WA Benjamin, Inc., 1977.

[55] Jan Petersen, Jürgen Volz, and Arno Rauschenbeutel. Chiral nanophotonic waveguide interface based on spin-orbit interaction of light. *Science*, 346(6205):67–71, 2014.

[56] William A Bonner. The origin and amplification of biomolecular chirality. *Origins of Life and Evolution of the Biosphere*, 21(2):59–111, 1991.

[57] LD Barron, EW Blanch, and L Hecht. Unfolded proteins studied by raman optical activity. *Advances in protein chemistry*, 62:51–90, 2002.

[58] JB Pendry. A chiral route to negative refraction. *Science*, 306(5700): 1353–1355, 2004.

[59] John B Pendry. Negative refraction. *Contemp. Phys.*, 45(3):191–202, 2004.

[60] John Brian Pendry. Negative refraction makes a perfect lens. *Phys. Rev. Lett.*, 85(18):3966, 2000.

[61] Nina Berova, Koji Nakanishi, and Robert W Woody. *Circular dichroism: principles and applications*. John Wiley & Sons, 2000.

[62] Robert W Woody. Circular dichroism. *Methods Enzymol.*, 246:34–71, 1995.

[63] Sang Soon Oh and Ortwin Hess. Chiral metamaterials: enhancement and control of optical activity and circular dichroism. *Nano Convergence*, 2 (1):1–14, 2015.

[64] Markku Oksanen and Arto Hujanen. How to determine chiral material parameters. In *1992 22nd European Microwave Conference*, volume 1, pages 195–199. IEEE, 1992.

[65] Konstantin Y Bliokh and Franco Nori. Characterizing optical chirality. *Phys. Rev. A*, 83(2):021803, 2011.

[66] Daniel M. Lipkin. Existence of a new conservation law in electromagnetic theory. *J. Math. Phys.*, 5(5):696–700, 1964. doi: 10.1063/1.1704165. URL `https://doi.org/10.1063/1.1704165`.

[67] TWB Kibble. Conservation laws for free fields. *J. Math. Phys.*, 6(7): 1022–1026, 1965.

[68] Robert P Cameron, Stephen M Barnett, and Alison M Yao. Optical helicity, optical spin and related quantities in electromagnetic theory. *New J. Phys.*, 14(5):053050, 2012.

[69] Jose L Trueba and Antonio F Ranada. The electromagnetic helicity. *Eur. J. Phys.*, 17(3):141, 1996.

[70] AF Ranada. On the magnetic helicity. *Eur. J. Phys.*, 13(2):70, 1992.

[71] M Schäferling. Chiral nanophotonics–chiral optical properties of phasmonic systems. *Springer Ser. Opt. Sci.*, 205, 2017.

[72] Yiqiao Tang and Adam E Cohen. Enhanced enantioselectivity in excitation of chiral molecules by superchiral light. *Science*, 332(6027):333–336, 2011.

[73] Joseph S. Choi and Minhaeng Cho. Limitations of a superchiral field. *Phys. Rev. A*, 86:063834, Dec 2012. doi: 10.1103/PhysRevA.86.063834. URL `https://link.aps.org/doi/10.1103/PhysRevA.86.063834`.

[74] Werner Kuhn. The physical significance of optical rotatory power. *Transactions of the Faraday Society*, 26:293–308, 1930.

[75] Chi-Sing Ho, Aitzol Garcia-Etxarri, Yang Zhao, and Jennifer Dionne. Enhancing enantioselective absorption using dielectric nanospheres. *ACS Photonics*, 4(2):197–203, 2017.

[76] Mina Hanifeh, Mohammad Albooyeh, and Filippo Capolino. Optimally chiral light: Upper bound of helicity density of structured light for chirality detection of matter at nanoscale. *ACS Photonics*, 7(10):2682–2691, 2020.

[77] Mina Hanifeh, Mohammad Albooyeh, and Filippo Capolino. Helicity maximization below the diffraction limit. *Phys. Rev. B*, 102(16):165419, 2020.

[78] COMSOL Multiphysics. Introduction to comsol multiphysics®. *COMSOL Multiphysics, Burlington, MA, accessed Feb*, 9(2018):32, 1998.

[79] Edmund JF Dickinson, Henrik Ekström, and Ed Fontes. Comsol multiphysics®: Finite element software for electrochemical analysis. a minireview. *Electrochemistry communications*, 40:71–74, 2014.

[80] Giuseppe Emanuele Lio, Giovanna Palermo, Roberto Caputo, and Antonio De Luca. A comprehensive optical analysis of nanoscale structures: from thin films to asymmetric nanocavities. *RSC advances*, 9(37):21429–21437, 2019.

[81] Giovanna Palermo, Kandammathe Valiyaveedu Sreekanth, Nicolò Maccaferri, Giuseppe Emanuele Lio, Giuseppe Nicoletta, Francesco De Angelis, Michael Hinczewski, and Giuseppe Strangi. Hyperbolic dispersion metasurfaces for molecular biosensing. *Nanophotonics*, 10(1):295–314, 2021.

[82] Andrew Lininger, Giovanna Palermo, Alexa Guglielmelli, Giuseppe Nicoletta, Madhav Goel, Michael Hinczewski, Giuseppe Strangi, et al. Chirality in light–matter interaction. *Adv. Mater*, 2107325, 2022.

[83] Giuseppe Emanuele Lio, Giovanna Palermo, Roberto Caputo, and Antonio De Luca. Opto-mechanical control of flexible plasmonic materials. *Journal of Applied Physics*, 125(8):082533, 2019.

[84] Fardad Koohyar, Farhoush Kiani, Sasan Sharifi, Meysam Sharifirad, and Seyed Hamed Rahmanpour. Study on the change of refractive index on mixing, excess molar volume and viscosity deviation for aqueous solution of methanol, ethanol, ethylene glycol, 1-propanol and 1, 2, 3-propantriol at t= 292.15 k and atmospheric pressure. *Research Journal of Applied Sciences, Engineering and Technology*, 4(17):3095–3101, 2012.

[85] Xinlong Xu, Bo Peng, Dehui Li, Jun Zhang, Lai Mun Wong, Qing Zhang, Shijie Wang, and Qihua Xiong. Flexible visible–infrared metamaterials and their applications in highly sensitive chemical and biological sensing. *Nano letters*, 11(8):3232–3238, 2011.

[86] Mengxin Ren, Chongpei Pan, Qunqing Li, Wei Cai, Xinzheng Zhang, Qiang Wu, Shoushan Fan, and Jingjun Xu. Isotropic spiral plasmonic metamaterial for sensing large refractive index change. *Optics Letters*, 38(16):3133–3136, 2013.

[87] Ugo Fano. Sullo spettro di assorbimento dei gas nobili presso il limite dello spettro d'arco. *Il Nuovo Cimento (1924-1942)*, 12(3):154–161, 1935.

[88] Mikhail F Limonov, Mikhail V Rybin, Alexander N Poddubny, and Yuri S Kivshar. Fano resonances in photonics. *Nature Photonics*, 11 (9):543–554, 2017.

[89] Michael Fleischhauer, Atac Imamoglu, and Jonathan P Marangos. Electromagnetically induced transparency: Optics in coherent media. *Reviews of modern physics*, 77(2):633, 2005.

[90] VB Novikov and TV Murzina. Borrmann effect in photonic crystals. *Optics letters*, 42(7):1389–1392, 2017.

[91] Wei Liu and Yuri S Kivshar. Generalized kerker effects in nanophotonics and meta-optics. *Optics express*, 26(10):13085–13105, 2018.

[92] Mohamed ElKabbash, Theodore Letsou, Sohail A Jalil, Nathaniel Hoffman, Jihua Zhang, James Rutledge, Andrew R Lininger, Chun-Hao Fann, Michael Hinczewski, Giuseppe Strangi, et al. Fano-resonant ultrathin film optical coatings. *Nature Nanotechnology*, 16(4):440–446, 2021.

[93] GE Jellison Jr. Optical functions of silicon determined by two-channel polarization modulation ellipsometry. *Optical Materials*, 1(1):41–47, 1992.

[94] GE Jellison, LA Boatner, et al. Optical functions of uniaxial zno determined by generalized ellipsometry. *Physical Review B*, 58(7):3586, 1998.

[95] DE Aspnes. Minimal-data approaches for determining outer-layer dielectric responses of films from kinetic reflectometric and ellipsometric measurements. *JOSA A*, 10(5):974–983, 1993.

[96] Alejandro Manjavacas and FJ García de Abajo. Tunable plasmons in atomically thin gold nanodisks. *Nature Communications*, 5(1):3548, 2014.

[97] GE Jellison Jr. Spectroscopic ellipsometry data analysis: measured versus calculated quantities. *Thin solid films*, 313:33–39, 1998.

[98] GE Jellison Jr, VI Merkulov, AA Puretzky, DB Geohegan, G Eres, DH Lowndes, and JB Caughman. Characterization of thin-film amorphous semiconductors using spectroscopic ellipsometry. *Thin Solid Films*, 377:68–73, 2000.

[99] PL Washington, HC Ong, JY Dai, and RPH Chang. Determination of the optical constants of zinc oxide thin films by spectroscopic ellipsometry. *Applied Physics Letters*, 72(25):3261–3263, 1998.

[100] GE Jellison Jr and FA Modine. Parameterization of the optical functions of amorphous materials in the interband region. *Applied Physics Letters*, 69(3):371–373, 1996.

[101] RW Collins and BY Yang. I nsitu ellipsometry of thin-film deposition: Implications for amorphous and microcrystalline si growth. *Journal of Vacuum Science & Technology B: Microelectronics Processing and Phenomena*, 7(5):1155–1164, 1989.

[102] JAd De Feijter, d J Benjamins, and FA Veer. Ellipsometry as a tool to study the adsorption behavior of synthetic and biopolymers at the air–water interface. *Biopolymers: Original Research on Biomolecules*, 17(7): 1759–1772, 1978.

[103] DE Aspnes, JB Theeten, and F Hottier. Investigation of effective-medium models of microscopic surface roughness by spectroscopic ellipsometry. *Physical Review B*, 20(8):3292, 1979.

[104] Marc D Porter, Thomas B Bright, David L Allara, and Christopher ED Chidsey. Spontaneously organized molecular assemblies. 4. structural characterization of n-alkyl thiol monolayers on gold by optical ellipsometry, infrared spectroscopy, and electrochemistry. *Journal of the American Chemical Society*, 109(12):3559–3568, 1987.

[105] Fausto D'apuzzo, Marco Esposito, Massimo Cuscunà, Alessandro Cannavale, Salvatore Gambino, Giuseppe E Lio, Antonio De Luca, Giuseppe Gigli, and Stefano Lupi. Mid-infrared plasmonic excitation in indium tin oxide microhole arrays. *ACS Photonics*, 5(6):2431–2436, 2018.

[106] Giuseppe Emanuele Lio, Antonio De Luca, Cesare Paolo Umeton, and Roberto Caputo. Opto-mechanically induced thermoplasmonic response of unclonable flexible tags with hotspot fingerprint. *Journal of Applied Physics*, 128(9):093107, 2020.

[107] Bo Zhen, Song-Liang Chua, Jeongwon Lee, Alejandro W Rodriguez, Xiangdong Liang, Steven G Johnson, John D Joannopoulos, Marin Soljačić, and Ofer Shapira. Enabling enhanced emission and low-threshold lasing of organic molecules using special fano resonances of macroscopic photonic crystals. *Proceedings of the National Academy of Sciences*, 110(34): 13711–13716, 2013.

[108] Yu Zhang, Yu-Rong Zhen, Oara Neumann, Jared K Day, Peter Nordlander, and Naomi J Halas. Coherent anti-stokes raman scattering with single-molecule sensitivity using a plasmonic fano resonance. *Nature communications*, 5(1):4424, 2014.

[109] Chihhui Wu, Alexander B Khanikaev, Ronen Adato, Nihal Arju, Ahmet Ali Yanik, Hatice Altug, and Gennady Shvets. Fano-resonant asymmetric metamaterials for ultrasensitive spectroscopy and identification of molecular monolayers. *Nature materials*, 11(1):69–75, 2012.

[110] SM Rossnagel. Thin film deposition with physical vapor deposition and related technologies. *Journal of Vacuum Science & Technology A: Vacuum, Surfaces, and Films*, 21(5):S74–S87, 2003.

[111] M Stueber, H Holleck, H Leiste, K Seemann, S Ulrich, and C Ziebert. Concepts for the design of advanced nanoscale pvd multilayer protective thin films. *Journal of Alloys and Compounds*, 483(1-2):321–333, 2009.

[112] John E Mahan. *Physical vapor deposition of thin films.* 2000.

[113] H Holleck, Schier, and V. Multilayer pvd coatings for wear protection. *Surface and Coatings Technology*, 76:328–336, 1995.

[114] Nanfang Yu and Federico Capasso. Optical metasurfaces and prospect of their applications including fiber optics. *Journal of Lightwave Technology*, 33(12):2344–2358, 2015.

[115] Alan Zhan, Shane Colburn, Rahul Trivedi, Taylor K Fryett, Christopher M Dodson, and Arka Majumdar. Low-contrast dielectric metasurface optics. *ACS Photonics*, 3(2):209–214, 2016.

[116] Amr M Shaltout, Alexander V Kildishev, and Vladimir M Shalaev. Evolution of photonic metasurfaces: from static to dynamic. *JOSA B*, 33 (3):501–510, 2016.

[117] Alexander V Kildishev, Alexandra Boltasseva, and Vladimir M Shalaev. Planar photonics with metasurfaces. *Science*, 339(6125):1232009, 2013.

[118] Giuseppe Emanuele Lio and Antonio Ferraro. Lidar and beam steering tailored by neuromorphic metasurfaces dipped in a tunable surrounding medium. In *Photonics*, volume 8, page 65. Multidisciplinary Digital Publishing Institute, 2021.

[119] Nanfang Yu and Federico Capasso. Flat optics with designer metasurfaces. *Nature materials*, 13(2):139–150, 2014.

[120] Heonyeong Jeong, Younghwan Yang, Hanlyun Cho, Trevon Badloe, Inki Kim, Ren-Min Ma, and Junsuk Rho. Emerging advanced metasurfaces: Alternatives to conventional bulk optical devices. *Microelectronic Engineering*, 220:111146, 2020.

[121] Patrice Genevet, Federico Capasso, Francesco Aieta, Mohammadreza Khorasaninejad, and Robert Devlin. Recent advances in planar optics: from plasmonic to dielectric metasurfaces. *Optica*, 4(1):139–152, 2017.

[122] Mohammadreza Khorasaninejad, Francesco Aieta, Pritpal Kanhaiya, Mikhail A Kats, Patrice Genevet, David Rousso, and Federico Capasso. Achromatic metasurface lens at telecommunication wavelengths. *Nano letters*, 15(8):5358–5362, 2015.

[123] Dianmin Lin, Pengyu Fan, Erez Hasman, and Mark L Brongersma. Dielectric gradient metasurface optical elements. *science*, 345(6194):298–302, 2014.

[124] Haejun Chung and Owen D Miller. Tunable metasurface inverse design for 80% switching efficiencies and 144 angular deflection. *ACS Photonics*, 7(8):2236–2243, 2020.

[125] Wei Ting Chen, Alexander Y Zhu, Vyshakh Sanjeev, Mohammadreza Khorasaninejad, Zhujun Shi, Eric Lee, and Federico Capasso. A broadband achromatic metalens for focusing and imaging in the visible. *Nature nanotechnology*, 13(3):220–226, 2018.

[126] Pin Chieh Wu, Weiming Zhu, Zhong Xiang Shen, Peter Han Joo Chong, Wee Ser, Din Ping Tsai, and Ai-Qun Liu. Broadband wide-angle multifunctional polarization converter via liquid-metal-based metasurface. *Advanced Optical Materials*, 5(7):1600938, 2017.

[127] Xingjie Ni, Alexander V Kildishev, and Vladimir M Shalaev. Metasurface holograms for visible light. *Nature communications*, 4(1):1–6, 2013.

[128] Qiong He, Shulin Sun, and Lei Zhou. Tunable/reconfigurable metasurfaces: physics and applications. *Research*, 2019, 2019.

[129] Inki Kim, Muhammad Afnan Ansari, Muhammad Qasim Mehmood, Won-Sik Kim, Jaehyuck Jang, Muhammad Zubair, Young-Ki Kim, and Junsuk Rho. Stimuli-responsive dynamic metaholographic displays with designer liquid crystal modulators. *Advanced Materials*, 32(50):2004664, 2020.

[130] Arash Nemati, Qian Wang, Minghui Hong, Jinghua Teng, et al. Tunable and reconfigurable metasurfaces and metadevices. *Opto-Electronic Advances*, 1(5):180009, 2018.

[131] Ping Yu, Jianxiong Li, Shuang Zhang, Zhongwei Jin, Gisela Sch*ü*tz, Cheng-Wei Qiu, Michael Hirscher, and Na Liu. Dynamic janus metasurfaces in the visible spectral region. *Nano letters*, 18(7):4584–4589, 2018.

[132] Jura Rensberg, Shuyan Zhang, You Zhou, Alexander S McLeod, Christian Schwarz, Michael Goldflam, Mengkun Liu, Jochen Kerbusch, Ronny Nawrodt, Shriram Ramanathan, et al. Active optical metasurfaces based on defect-engineered phase-transition materials. *Nano letters*, 16(2): 1050–1055, 2016.

[133] Pierre-Gilles De Gennes and Jacques Prost. *The physics of liquid crystals*. Number 83. Oxford university press, 1993.

[134] Andrei Komar, Zheng Fang, Justus Bohn, Jürgen Sautter, Manuel Decker, Andrey Miroshnichenko, Thomas Pertsch, Igal Brener, Yuri S Kivshar, Isabelle Staude, et al. Electrically tunable all-dielectric optical metasurfaces based on liquid crystals. *Applied Physics Letters*, 110(7): 071109, 2017.

[135] Jianxiong Li, Ping Yu, Shuang Zhang, and Na Liu. Electrically-controlled digital metasurface device for light projection displays. *Nature communications*, 11(1):1–7, 2020.

[136] Jorik van de Groep, Jung-Hwan Song, Umberto Celano, Qitong Li, Pieter G Kik, and Mark L Brongersma. Exciton resonance tuning of an atomically thin lens. *Nature Photonics*, 14(7):426–430, 2020.

[137] Alex Krasnok. Metalenses go atomically thick and tunable. *Nature Photonics*, 14(7):409–410, 2020.

[138] Guillaume Baffou and Romain Quidant. Thermo-plasmonics: using metallic nanostructures as nano-sources of heat. *Laser & Photonics Reviews*, 7(2):171–187, 2013.

[139] Guillaume Baffou, Frank Cichos, and Romain Quidant. Applications and challenges of thermoplasmonics. *Nature Materials*, 19(9):946–958, 2020.

[140] Giuseppe Emanuele Lio, Giovanna Palermo, Antonio De Luca, and Roberto Caputo. Tensile control of the thermal flow in plasmonic heaters realized on flexible substrates. *The Journal of chemical physics*, 151(24): 244707, 2019.

[141] Giovanna Palermo, Donatello Pagnotto, Loredana Ricciardi, Luigia Pezzi, Massimo La Deda, and Antonio De Luca. Thermoplasmonic effects in gain-assisted nanoparticle solutions. *The Journal of Physical Chemistry C*, 121(43):24185–24191, 2017.

[142] G Baffou, R Quidant, and Ch Girard. Heat generation in plasmonic nanostructures: Influence of morphology. *Applied Physics Letters*, 94 (15):153109, 2009.

[143] Kathryn M Mayer and Jason H Hafner. Localized surface plasmon resonance sensors. *Chemical reviews*, 111(6):3828–3857, 2011.

[144] Alexander O Govorov and Hugh H Richardson. Generating heat with metal nanoparticles. *Nano today*, 2(1):30–38, 2007.

[145] Giovanna Palermo, Alexa Guglielmelli, Luigia Pezzi, Ugo Cataldi, Luciano De Sio, Roberto Caputo, Antonio De Luca, Thomas Bürgi, Nelson Tabiryan, and Cesare Umeton. A command layer for anisotropic plasmonic photo-thermal effects in liquid crystal. *Liquid Crystals*, 45(13-15): 2214–2220, 2018.

[146] Luciano De Sio, Ugo Cataldi, Alexa Guglielmelli, Thomas Bürgi, Nelson Tabiryan, and Timothy J Bunning. Dynamic optical properties of gold

nanoparticles/cholesteric liquid crystal arrays. *MRS Communications*, 8 (2):550–555, 2018.

[147] Iam-Choon Khoo. *Liquid crystals*. John Wiley & Sons, 2022.

[148] Robert H Chen. *Liquid crystal displays: fundamental physics and technology*. John Wiley & Sons, 2011.

[149] Donald L Melchior and Joseph M Steim. Thermotropic transitions in biomembranes. *Annual review of biophysics and bioengineering*, 5(1): 205–238, 1976.

[150] Michel Mitov. Cholesteric liquid crystals in living matter. *Soft Matter*, 13(23):4176–4209, 2017.

[151] Ger Vertogen and Wim H De Jeu. *Thermotropic liquid crystals, fundamentals*, volume 45. Springer Science & Business Media, 2012.

[152] Constantinos M Paleos and Dimitris Tsiourvas. Thermotropic liquid crystals formed by intermolecular hydrogen bonding interactions. *Angewandte Chemie International Edition in English*, 34(16):1696–1711, 1995.

[153] Chenyu Guo, Jun Wang, Fengliang Cao, Robert J Lee, and Guangxi Zhai. Lyotropic liquid crystal systems in drug delivery. *Drug discovery today*, 15(23-24):1032–1040, 2010.

[154] Ingo Dierking and Antônio Martins Figueiredo Neto. Novel trends in lyotropic liquid crystals. *Crystals*, 10(7):604, 2020.

[155] Jun Li, Sebastian Gauzia, and Shin-Tson Wu. High temperature-gradient refractive index liquid crystals. *Optics express*, 12(9):2002–2010, 2004.

[156] Giovanna Palermo, Andrew Lininger, Alexa Guglielmelli, Loredana Ricciardi, Giuseppe Nicoletta, Antonio De Luca, Joon-Suh Park, Soon Wei Daniel Lim, Maryna L Meretska, Federico Capasso, et al. All-optical

tunability of metalenses permeated with liquid crystals. *ACS nano*, 16 (10):16539–16548, 2022.

[157] Andrew Lininger, Alexander Y Zhu, Joon-Suh Park, Giovanna Palermo, Sharmistha Chatterjee, Jonathan Boyd, Federico Capasso, and Giuseppe Strangi. Optical properties of metasurfaces infiltrated with liquid crystals. *Proceedings of the National Academy of Sciences*, 117(34):20390–20396, 2020.

[158] ABD Cassie and Skyler Baxter. Wettability of porous surfaces. *Transactions of the Faraday society*, 40:546–551, 1944.

[159] Robert N Wenzel. Resistance of solid surfaces to wetting by water. *Industrial & Engineering Chemistry*, 28(8):988–994, 1936.

[160] Jungchul Kim, Myoung-Woon Moon, and Ho-Young Kim. Dynamics of hemiwicking. *Journal of Fluid Mechanics*, 800:57–71, 2016.

[161] CW Extrand, Sung In Moon, P Hall, and D Schmidt. Superwetting of structured surfaces. *Langmuir*, 23(17):8882–8890, 2007.

[162] SD Durbin, SM Arakelian, and YR Shen. Optical-field-induced birefringence and freedericksz transition in a nematic liquid crystal. *Physical Review Letters*, 47(19):1411, 1981.

[163] Soham Saha, Deesha Shah, Vladimir M Shalaev, and Alexandra Boltasseva. Tunable metasurfaces: controlling light in space and time. *Optics and Photonics News*, 32(7):34–41, 2021.

[164] Shuming Wang, Pin Chieh Wu, Vin-Cent Su, Yi-Chieh Lai, Mu-Ku Chen, Hsin Yu Kuo, Bo Han Chen, Yu Han Chen, Tzu-Ting Huang, Jung-Hsi Wang, et al. A broadband achromatic metalens in the visible. *Nature nanotechnology*, 13(3):227–232, 2018.

[165] Fatih Balli, M Sultan, Sarah K Lami, and Jeffrey T Hastings. A hybrid achromatic metalens. *Nature communications*, 11(1):3892, 2020.

[166] Alexander Lachmann, Denis Torre, Alexandra B Keenan, Kathleen M Jagodnik, Hoyjin J Lee, Lily Wang, Moshe C Silverstein, and Avi Ma'ayan. Massive mining of publicly available rna-seq data from human and mouse. *Nature communications*, 9(1):1366, 2018.

[167] Gun-Yeal Lee, Jong-Young Hong, SoonHyoung Hwang, Seokil Moon, Hyeokjung Kang, Sohee Jeon, Hwi Kim, Jun-Ho Jeong, and Byoungho Lee. Metasurface eyepiece for augmented reality. *Nature communications*, 9(1):4562, 2018.

[168] Shane Colburn, Alan Zhan, and Arka Majumdar. Varifocal zoom imaging with large area focal length adjustable metalenses. *Optica*, 5(7): 825–831, 2018.

[169] Joon-Suh Park, Shuyan Zhang, Alan She, Wei Ting Chen, Peng Lin, Kerolos MA Yousef, Ji-Xin Cheng, and Federico Capasso. All-glass, large metalens at visible wavelength using deep-ultraviolet projection lithography. *Nano letters*, 19(12):8673–8682, 2019.

[170] Wei Bai, Ping Yang, Jie Huang, Dingbo Chen, Jingjing Zhang, Zhaojian Zhang, Junbo Yang, and Bing Xu. Near-infrared tunable metalens based on phase change material ge2sb2te5. *Scientific reports*, 9(1):5368, 2019.

[171] Trevon Badloe, Inki Kim, Yeseul Kim, Joohoon Kim, and Junsuk Rho. Electrically tunable bifocal metalens with diffraction-limited focusing and imaging at visible wavelengths. *Advanced Science*, 8(21):2102646, 2021.

[172] Wenwei Liu, Dina Ma, Zhancheng Li, Hua Cheng, Duk-Yong Choi, Jianguo Tian, and Shuqi Chen. Aberration-corrected three-dimensional positioning with a single-shot metalens array. *Optica*, 7(12):1706–1713, 2020.

[173] Jaekyung Kim, Junhwa Seong, Younghwan Yang, Seong-Won Moon, Trevon Badloe, and Junsuk Rho. Tunable metasurfaces towards ver-

satile metalenses and metaholograms: a review. *Advanced Photonics*, 4 (2):024001–024001, 2022.

[174] Adeel Afridi, Josep Canet-Ferrer, Laurent Philippe, Johann Osmond, Pascal Berto, and Romain Quidant. Electrically driven varifocal silicon metalens. *Acs Photonics*, 5(11):4497–4503, 2018.

[175] Taimoor Naeem, Hafiz Saad Khaliq, Muhammad Zubair, Tauseef Tauqeer, and Muhammad Qasim Mehmood. Engineering tunability through electro-optic effects to manifest a multifunctional metadevice. *RSC advances*, 11(22):13220–13228, 2021.

[176] Peng Lin, Yu-Sheng Lin, Jie Lin, and Bo-Ru Yang. Stretchable metalens with tunable focal length and achromatic characteristics. *Results in Physics*, 31:105005, 2021.

[177] Ho-Seok Ee and Ritesh Agarwal. Tunable metasurface and flat optical zoom lens on a stretchable substrate. *Nano letters*, 16(4):2818–2823, 2016.

[178] Alan She, Shuyan Zhang, Samuel Shian, David R Clarke, and Federico Capasso. Adaptive metalenses with simultaneous electrical control of focal length, astigmatism, and shift. *Science advances*, 4(2):eaap9957, 2018.

[179] Zhixiong Shen, Shenghang Zhou, Xinan Li, Shijun Ge, Peng Chen, Wei Hu, and Yanqing Lu. Liquid crystal integrated metalens with tunable chromatic aberration. *Advanced Photonics*, 2(3):036002–036002, 2020.

[180] Chinhua Wang and Qian Xu. Fabrication and imaging of liquid crystal-based metalens. In *First Optics Frontier Conference*, volume 11850, pages 105–113. SPIE, 2021.

[181] Melissa Bosch, Maxim R Shcherbakov, Kanghee Won, Hong-Seok Lee, Young Kim, and Gennady Shvets. Electrically actuated varifocal lens

based on liquid-crystal-embedded dielectric metasurfaces. *Nano Letters*, 21(9):3849–3856, 2021.

[182] Chun-Yuan Fan, Tsung-Jung Chuang, Kuo-Hao Wu, and Guo-Dung J Su. Electrically modulated varifocal metalens combined with twisted nematic liquid crystals. *Optics Express*, 28(7):10609–10617, 2020.

[183] Shenghang Zhou, Zhixiong Shen, Xinan Li, Shijun Ge, Yanqing Lu, and Wei Hu. Liquid crystal integrated metalens with dynamic focusing property. *Optics Letters*, 45(15):4324–4327, 2020.

[184] Zhenghao Wang, Yongling Wu, Dongfeng Qi, Wenhui Yu, and Hongyu Zheng. Progress in the design, nanofabrication, and performance of metalenses. *Journal of Optics*, 24(3):033001, 2022.

[185] Amit Kessel, Christian Frydendahl, Sita Rama Krishna Chaitanya Indukuri, Noa Mazurski, Pankaj Arora, and Uriel Levy. Soft lithography for manufacturing scalable perovskite metasurfaces with enhanced emission and absorption. *Advanced Optical Materials*, 8(23):2001627, 2020.

[186] Xinyi Cao, Yibo Xiao, Qiao Dong, Shaobo Zhang, Junzhuan Wang, Lianhui Wang, and Li Gao. Tuning metasurface dimensions by soft nanoimprint lithography and reactive ion etching. *Advanced Photonics Research*, 3(11):2200127, 2022.

[187] Jingkai Huang, Yuetang Wang, Liming Yuan, Cheng Huang, Jianming Liao, Chen Ji, and Xiangang Luo. Large-area and flexible plasmonic metasurface for laser–infrared compatible camouflage. *Laser & Photonics Reviews*, 17(3):2200616, 2023.

[188] Ying Zhang, Chi-Wei Lo, J Ashley Taylor, and Shu Yang. Replica molding of high-aspect-ratio polymeric nanopillar arrays with high fidelity. *Langmuir*, 22(20):8595–8601, 2006.

[189] Younan Xia and George M Whitesides. Soft lithography. *Annual review of materials science*, 28(1):153–184, 1998.

[190] Mikhail N Krakhalev, Oxana O Prishchepa, Vitaly S Sutormin, and Victor Ya Zyryanov. Polymer dispersed nematic liquid crystal films with conical boundary conditions for electrically controllable polarizers. *Optical Materials*, 89:1–4, 2019.

[191] Oksana Olegovna Prishchepa, Aleksandr Vasil'evich Shabanov, V Ya Zyryanov, AM Parshin, and Vasilii Gennadievich Nazarov. Friedericksz threshold field in bipolar nematic droplets with strong surface anchoring. *JETP letters*, 84:607–612, 2007.

[192] Daniela Cupelli, Fiore Pasquale Nicoletta, Sabrina Manfredi, Marco Vivacqua, Patrizia Formoso, Giovanni De Filpo, and Giuseppe Chidichimo. Self-adjusting smart windows based on polymer-dispersed liquid crystals. *Solar Energy Materials and Solar Cells*, 93(11):2008–2012, 2009.

[193] Hadi Hosseinzadeh Khaligh, Kelvin Liew, Yining Han, Nasser Mohieddin Abukhdeir, and Irene A Goldthorpe. Silver nanowire transparent electrodes for liquid crystal-based smart windows. *Solar Energy Materials and Solar Cells*, 132:337–341, 2015.

[194] Heinz-S Kitzerow. Polymer-dispersed liquid crystals from the nematic curvilinear aligned phase to ferroelectric films. *Liquid Crystals*, 16(1): 1–31, 1994.

[195] Philip K Chan and Alejandro D Rey. Polymerization-induced phase separation. 1. droplet size selection mechanism. *Macromolecules*, 29(27): 8934–8941, 1996.

[196] Yi-Hsin Lin and Yu-Shih Tsou. A polarization independent liquid crystal phase modulation adopting surface pinning effect of polymer dispersed liquid crystals. *Journal of Applied Physics*, 110(11):114516, 2011.

[197] Srinivas Pagidi, Ramesh Manda, Surjya Sarathi Bhattacharyya, Sung Guk Lee, Seong Min Song, Young Jin Lim, Joong Hee Lee, and Seung Hee Lee. Fast switchable micro-lenticular lens arrays using highly

transparent nano-polymer dispersed liquid crystals. *Advanced Materials Interfaces*, 6(18):1900841, 2019.

[198] Hui Li, Yancheng He, Yi Yu, Yuntao Wu, Shuiping Zhang, and Yanduo Zhang. A light field display realization with a nematic liquid crystal microlens array and a polymer dispersed liquid crystal film. In *Photonics*, volume 9, page 244. MDPI, 2022.

[199] Hongwen Ren, Yi-Hsin Lin, Yun-Hsing Fan, and Shin-Tson Wu. Polarization-independent phase modulation using a polymer-dispersed liquid crystal. *Applied Physics Letters*, 86(14):141110, 2005.

[200] Hongwen Ren, Yun-Hsing Fan, Yi-Hsin Lin, and Shin-Tson Wu. Tunable-focus microlens arrays using nanosized polymer-dispersed liquid crystal droplets. *Optics communications*, 247(1-3):101–106, 2005.

[201] Giuseppe Emanuele Lio, Antonio Ferraro, Tiziana Ritacco, Dante Maria Aceti, Antonio De Luca, Michele Giocondo, and Roberto Caputo. Leveraging on enz metamaterials to achieve 2d and 3d hyper-resolution in two-photon direct laser writing. *Advanced Materials*, 33(18):2008644, 2021.